Willem E. van Caspel

Atmospheric Tides in the Mesosphere and Lower Thermosphere

Meteor Wind Observations and Mechanistic Tidal Model Simulations

Thesis for the degree of Philosophiae Doctor

Trondheim, February 2022

Norwegian University of Science and Technology
Faculty of Natural Sciences
Department of Physics

NTNU
Innovation and Creativity

NTNU Norwegian University of Science and Technology

Doctoral thesis
for the degree of Philosophiae Doctor

Faculty of Natural Sciences
Department of Physics

ISBN (printed version)
ISBN (electronic version)
ISSN 1503-8181

Doctoral theses at NTNU,

Printed by NTNU-trykk

Abstract

Atmospheric tides are global-scale waves whose periods are an integer fraction of a solar or lunar day. While the tides are primarily excited in the lower atmosphere, their amplitudes can become very large at high altitudes. As a result, the tides can strongly impact the chemistry and dynamics of the upper atmosphere and ionosphere. In this thesis, the drivers of the seasonal and short-term variations of the atmospheric tides are investigated by means of meteor radar wind measurements and mechanistic tidal model simulations.

Meteor wind measurements made by a global-scale array of SuperDARN radars are utilized to measure the sun-synchronous, or migrating, components of the tides in the mid- to high-latitude mesosphere and lower thermosphere (MLT). The SuperDARN radars span over 180° of longitude on a latitude band centered on 60°N, and make hourly wind measurements based on the backscatter signal of meteor ablation trails. Leveraging the geographical extent and time of operation of the SuperDARN radars, unambiguous observations of the migrating tides are presented for a time period spanning 16 years.

The semidiurnal tide (SDT) is a major source of variability in the mid- and high-latitudes. To investigate the driving mechanisms of the seasonal variations of the SDT, simulations made using a mechanistic tidal model are validated against SuperDARN observations of the migrating SDT for the year 2015. Numerical experiments identify the impact of tidal dissipation, the background atmosphere, and surface reflections on establishing the simulated SW2 tide. The background atmosphere and eddy diffusion are found to strongly impact the seasonal behavior of the SDT, while the interference between the upward propagating tide and its surface reflection plays an important role during the summer months.

To investigate the drivers of short-term tidal variability, the SDT response to the 2013 major sudden stratospheric warming (SSW) event is simulated. The simulation results are validated against meteor wind observations made by the CMOR (43.3°N, 80.8°W), Collm (51.3°N, 13.0°E), and Kiruna (67.5°N, 20.1°E) radars, and against the migrating SDT measured by the SuperDARN radars. Numerical experiments identify the relative importance of the background atmosphere, non-linear interactions between the migrating SDT and quasi-stationary planetary waves, and variations in the tidal forcing. In addition, special attention is paid to the individual role of the solar and lunar SDT components. Results find that the solar SDT accounts for the majority of the net SDT variability, while being strongly impacted by the background atmosphere and by non-linear wave-wave interactions.

The SuperDARN model sampling technique, represented by a Gaussian vertical averaging kernel following the SuperDARN meteor echo distribution, is used to compare the mean zonal winds measured by SuperDARN radars against those simulated by the WACCMX-DART model for the 2009 SSW event. The temporal and spatial evolution of the measured winds compare favourably to the simulated winds, giving confidence in the representation of the polar vortex in the WACCMX-DART model. Further model analysis, in conjunction with temperature and nitric oxide (NO_X) volume mixing ratio observations, finds that the downward transport of NO_X during the SSW event was a factor of five greater in the trough than in the ridge of the polar vortex.

List of Papers

Paper I

van Caspel, W. E., Espy, P. J., Hibbins, R. E., & McCormack, J. P. (2020). Migrating tide climatologies measured by a high-latitude array of SuperDARN HF radars. *Annales Geophysicae* (Vol. 38, No. 6, pp. 1257-1265). https://doi.org/10.5194angeo-38-1257-2020

WEC, PJE and REH developed the concept, while WEC performed the data analysis and wrote the paper. JPM provided NAVGEM-HA data and contributed to Sect. 2.3. PJE, REH and JPM gave feedback on the development of the work.

Paper II

van Caspel, W. E., Espy, P. J., Ortland, D. A., & Hibbins, R. E. (2022). The mid- to high-latitude migrating semidiurnal tide: Results from a mechanistic tide model and SuperDARN observations. *Journal of Geophysical Research: Atmospheres*, 127, e2021JD036007. https://doi.org/10.1029/2021JD036007

WEC developed the concept, performed the data and model analysis, and wrote the paper. PJE, REH, and DAO gave feedback on the development of the manuscript.

Paper III

van Caspel, W. E., Espy, P. J., Hibbins, R. E., Stober, G., Chartier, A., Brown, P., Jacobi, C., Kero, J., & Belova, E. A case study of the solar and lunar semidiurnal tide response to the 2013 major sudden stratospheric warming event. *Prepared for Submission to Journal of Geophysical Research: Atmospheres*.

WEC developed the concept, performed the data and model analysis, and wrote the paper. PJE and REH gave feedback on the development of the manuscript. GS processed and prepared the Collm, Kiruna, and CMOR meteor radar data, which was supplied by PB, CJ, JK, and EB. AC provided the SuperDARN meteor wind data.

Paper IV

Harvey, V. L., Datta-Barua, S., Pedatella, N. M., Wang, N., Randall, C. E., Siskind, D. E., & van Caspel, W. E. (2021). Transport of nitric oxide via Lagrangian coherent structures into the top of the polar vortex. *Journal of Geophysical Research: Atmospheres*, 126, e2020JD034523. https://doi.org/10.1029/2020JD034523

WEC contributed the SuperDARN wind and WACCMX-DART analysis, and the text in section 2 describing the SuperDARN analysis.

Acknowledgement

List of Symbols and Abbreviations

t	:	time [s]
u	:	zonal velocity [ms^{-1}]
v	:	meridional velocity [ms^{-1}]
$\hat{i}$, $\hat{j}$, $\hat{k}$	:	local eastward, northward and upward unit vectors
$\vec{u} = \hat{i}u + \hat{j}v$	:	horizontal velocity vector
λ	:	geographic longitude [rad]
ϕ	:	geographic latitude [rad]
Ω	:	angular velocity planet Earth [s^{-1}]
$f = 2\Omega \sin 2\phi$	:	Coriolis parameter [s^{-1}]
Φ	:	geopotential height [$\mathrm{m}^2\mathrm{s}^{-2}$]
∇_H	:	horizontal gradient operator
R	:	gas constant for dry air per unit mass [J $\mathrm{kg}^{-1}\mathrm{K}^{-1}$]
C_p	:	specific heat at constant pressure per unit mass [J $\mathrm{kg}^{-1}\mathrm{K}^{-1}$]
κ	:	R/C_p

MLT	:	Mesosphere-Lower-Thermosphere
DT	:	Diurnal Tide
SDT	:	Semidiurnal Tide
TDT	:	Terdiurnal Tide
SuperDARN	:	Super Dual Auroral Radar Network
GCM	:	General Circulation Model
PRISM	:	Primitive Equations in Sigma-coordinates Model
SD-WACCMX	:	Specified Dynamics Whole-Atmosphere Community Climate
	:	Model with thermosphere and ionosphere eXtension
DART	:	Data Assimilation Research Testbed
SSW	:	Sudden Stratospheric Warming
NO_X	:	Reactive odd nitrogen (NO_X = NO + NO_2)
FWHM	:	Full Width at Half Maximum
LOS	:	Line Of Sight

Contents

Abstract **i**

List of Papers **iii**

Acknowledgement **v**

List of Symbols and Abbreviations **vii**

1 Introduction **1**

2 Meteor Wind Observations **7**

2.1 Meteor Trail Backscatter 7

2.2 Longitudinal Array of SuperDARN Radars 8

2.3 Measuring the Migrating Tides 8

2.3.1 Migrating Tide Climatologies 11

3 Mechanistic Tidal Model **13**

3.1 Primitive Equations 15

3.1.1 Tidal Forcing 17

3.1.2 Specified Dynamics 19

3.2 The Migrating Semidiurnal Tide 20
3.3 Semidiurnal Sudden Stratospheric Warming Response 23

4 Downward Transport of Nitric Oxide **31**

5 Conclusion and Future Work **35**

Bibliography **39**

6 Publications **49**

Chapter 1

Introduction

Earth's atmosphere represents a highly dynamic system where the physics from a broad range of disciplines come together to form a complex interplay of chemistry, dynamics, electrodynamics, and radiation. While most of us are familiar with the lower region of the atmosphere, the troposphere, a wealth of physical phenomena take place in the higher altitudes. The atmosphere is traditionally divided into its different regions based on the vertical temperature gradient, as illustrated in Fig. 1.1. The temperature decreases by altitude in the troposphere, increases in the stratosphere, decreases again in the mesosphere, and increases in the thermosphere until reaching the exosphere ($\sim$600 km altitude). The ionosphere, the ionized part of the atmosphere that contains free ions and electrons, lies within the mesosphere and thermosphere, and extends down to around 65 km during the day and to around 85 km during the night.

While the majority of atmospheric motions occur along the horizontal, the lower atmosphere is nevertheless strongly coupled to the upper atmosphere through atmospheric waves. Atmospheric waves generated in the troposphere can propagate upwards into the stratosphere and above, provided atmospheric conditions are favourable. When the wave amplitudes become sufficiently large, they can break, depositing their energy and momentum impulse locally. The waves thereby effectively serve as a transfer mechanism for energy and momentum from the lower to the upper atmosphere. This vertical coupling mechanism represents a major

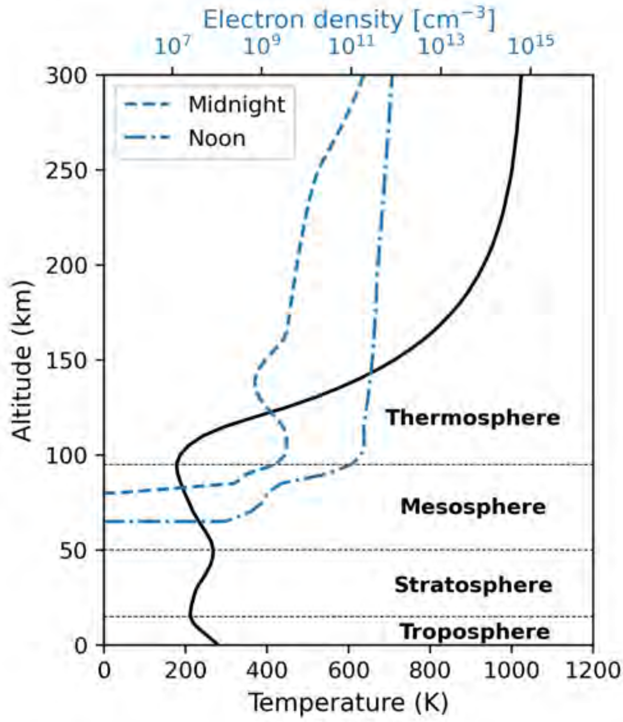

Figure 1.1: Global mean vertical temperature (black) based on the empirical NRLMSISE-00 model (Picone et al. 2002), and the equatorial electron densities (blue) at midnight (dashed) and noon (dashdot) local time from the International Reference Ionosphere (Bilitza 2001).

paradigm in modern atmospheric science (Yiğit et al. 2016), and has given rise to our understanding of the dynamics of the stratospheric polar vortex (Matsuno 1971), the gravity-wave driven mesospheric circulation (Holton 1982), and the quasi-biennial oscillation (Plumb and Bell 1982). Atmospheric waves are typically classified based on the nature of their restoring force. For example, common wave-types are gravity waves (or 'buoyancy waves'), planetary Rossby waves, and inertio-gravity waves (Andrews et al. 1987). The restoring force for gravity waves is the vertical buoyancy force, while the restoring force for planetary Rossby waves is the horizontal Coriolis force that results from the rotation of the Earth. Inertio-gravity waves are gravity waves whose horizontal and temporal scales are sufficiently large that they are also affected by Earth's rotation. One type of inertio-gravity waves are the atmospheric tides, which form the focus of this thesis.

Atmospheric tides are global-scale waves that are primarily excited by the periodic heating of the atmosphere by the sun, and to a lesser extent by the gravitational attraction of the moon. The thermally excited tides, referred to as the solar tides, have periods that are an integer fraction of a solar day. The principal components are the 24 hr diurnal tide (DT), 12 hr semidiurnal tide (SDT), and 8 hr terdiurnal tide (TDT). The gravitationally excited lunar tides have periods that are an integer fraction of a lunar day, with the most dominant component being the 12.42 hr lunar semidiurnal M_2 tide. The study of atmospheric tides has a history going back as far as the late 18th century, when Laplace formulated the tidal equations (Chapman and Lindzen 1970). For a dissipationless atmosphere having a zero mean flow, the solution to Laplace's tidal equations yields the horizontal structure of the atmospheric tides. The solution is described by its latitudinal Hough mode (spherical harmonic) structure for a given zonal wavenumber and forcing frequency. While the tides are generally defined by their frequency, or period of oscillation, their zonal wavenumber classifies them either as being migrating or non-migrating. For example, the solar migrating diurnal, semidiurnal, and terdiurnal tides follow the apparent motion of the sun over the course of a day, having zonal wavenumbers S = 1, 2, and 3, respectively. Non-migrating tides also have periods of an integer fraction of a solar day, but are not sun-synchronous. Through constructive and destructive interference between the migrating and non-migrating tides, the non-migrating tides represent longitudinal variations in the net tidal wave field.

The thermal and gravitational excitation of the tides takes place mostly in the lower atmosphere, where the density of the atmosphere is greatest. For the solar tides, the principal excitation mechanisms are the absorption of radiation by tropospheric water vapour and stratospheric ozone, and latent heat release by tropospheric clouds (Hagan 1996). As the tides propagate upwards, their amplitude grows exponentially with altitude to conserve energy as the density of the air decreases. Upon reaching the mesosphere and lower thermosphere (MLT), the tides can readily reach amplitudes upwards of 60-80 ms^{-1} in the horizontal winds. In addition to the horizontal wind components, the tides are also observed in the atmospheric temperature, density, and pressure. Moreover, the tidal oscillations present in the neutral atmosphere also interact with the ionosphere. For example, the charge separation driven by the collision between tidal winds and ions lies at the basis of a global system of ionospheric currents (Yamazaki and Maute 2017). Atmospheric tides therefore represent an important vertical coupling mechanism between the lower atmosphere and the MLT and ionosphere system. Their role as a vertical coupling mechanism is compounded by the fact that the tides are influenced by their excitation, propagation, and dissipation conditions throughout the atmospheric column (Forbes 2009, Pedatella and Forbes 2010).

Given the widespread presence of the tides in the MLT and ionosphere system, understanding the sources of their long- and short-term variability is critically important. However, measurements capable of delineating the global structure of the tides are difficult to obtain. Such measurements nevertheless have an important role in quantifying the natural background tidal variability, as well as serving as a validation tool for model simulations. In this thesis, a method is presented that unambiguously separates the migrating tides using the meteor wind measurements made by a longitudinal array of SuperDARN meteor radars in the MLT. This method is validated in Paper I, which demonstrates that the SuperDARN radars support migrating tide measurements with a high temporal resolution. Paper I also presents a mid- to high-latitude migrating tide climatology based on 16 years of measurements. In Paper II, the SuperDARN observations of the migrating SDT are leveraged to understand the drivers of its seasonal variability by means of mechanistic tidal model simulations and numerical experiments. Paper III extends the migrating SDT model to simulate the short-term variability of the total SDT response to the 2013 major sudden stratospheric warming (SSW) event, during which the tides were observed to display a high degree of variability on short timescales. Here the simulated SDT is validated against a range of mid- and high-latitude meteor wind observations, including the migrating SDT measurements from the SuperDARN radars. In Paper III, special attention is paid to the individual role of the solar and lunar SDT components. The model sampling technique presented in Paper II is furthermore applied in Paper IV for the comparison of model simulations against SuperDARN mean wind observations, to investigate the downward transport of mesospheric NO_X during the 2009 major SSW event. The following chapters summarize and discuss the main points and conclusions of each of the papers submitted as part of this thesis, and emphasis is placed on the significance of the results within the body of existing literature and for future study. A more detailed description of the model used in Papers II and III is also given, emphasizing those aspects of the model which have been further developed as part of this work.

Chapter 2

Meteor Wind Observations

2.1 Meteor Trail Backscatter

A commonly used method to measure winds in the MLT region is through the use of radars that measure the backscatter signal of meteor ablation trails (Reid 2015). Sub-visual meteors are a ubiquitous feature of the 80-120 km altitude region, where they leave trails of ionized gas upon their entry into Earth's atmosphere. High-Frequency (HF, 3-30 MHz) and Very-High-Frequency (VHF, 30-300 MHz) radiation waves emitted from ground-based radar stations can be scattered by these ionised gasses, and the return signal, or so-called 'meteor echo', can be used to determine the Line Of Sight (LOS) velocity of the neutral winds carrying the ablation trail. By combining the LOS velocities from a number of differently oriented radar beams, the horizontal wind vector carrying the meteor ablation trail can be calculated. Traditional meteor radars measure the neutral winds by binning the LOS velocities by altitude and time, often in hourly increments. The resulting near-continuous time series of hourly wind measurements provide an excellent tool to determine the vertical and temporal variability of the atmospheric tides. A major limitation of traditional meteor radar measurements is, however, that they are limited to a single location. Given the global structure of the atmospheric tides, interpreting tidal variability measured at a single location can be complicated since only the superposition of multiple tidal modes can be observed. To circumvent this problem, a methodology is presented to separate the zonal structure of the migrating tides from meteor wind observations made by a global-scale longitudinal array of SuperDARN meteor radars.

2.2 Longitudinal Array of SuperDARN Radars

As described in detail in Paper I, the SuperDARN radar network is comprised of over 40 similarly operating HF (10-15 MHz) radars, built to measure ion drift velocities over the polar cap regions. However, the SuperDARN radars also record meteor echoes in their first five range gates (Chisham 2018, Hall et al. 1997), which can be used as a measure of the meteor trail LOS velocities for each of their angularly separated radar beams. Hourly winds are retrieved by least-squares fitting a function representing a mean zonal and meridional wind to the hourly binned LOS velocities for all radar beams. The vertical meteor echo distribution as measured by the SuperDARN radars is approximately a Gaussian in altitude, centered on 100 km with a Full Width at Half Maximum (FWHM) of 30 km (Chisham and Freeman 2013). Since not all of the radars are equipped with height interferometry, the standard SuperDARN wind product, as used in this thesis, therefore represents a broad vertical average. The spatial coverage provided by the radars nevertheless provides a unique opportunity to observe longitudinal variations in the atmospheric winds (Hibbins et al. 2019, Kleinknecht et al. 2014). An additional strength of the SuperDARN radars is their long and consistent mode of operation, with meteor wind measurements going back as far as the year 1995 (Hall et al. 1997).

The geographical locations and abbreviated names of the 10 SuperDARN radar stations used in this thesis are illustrated in Fig. 2.1a. The high-latitude array spans over 180° of longitude on a 14° latitude band centered on 60°N, while the radars have been resolving time-synchronous hourly wind measurements consistently between the year 2000 and 2016, as shown in Fig. 2.1b.

2.3 Measuring the Migrating Tides

The migrating tides are those tides that follow the apparent motion of the sun over the course of the day, with the diurnal, semidiurnal, and terdiurnal tides having a zonal wavenumber S = 1, 2, and 3 structure, respectively. Given the apparent

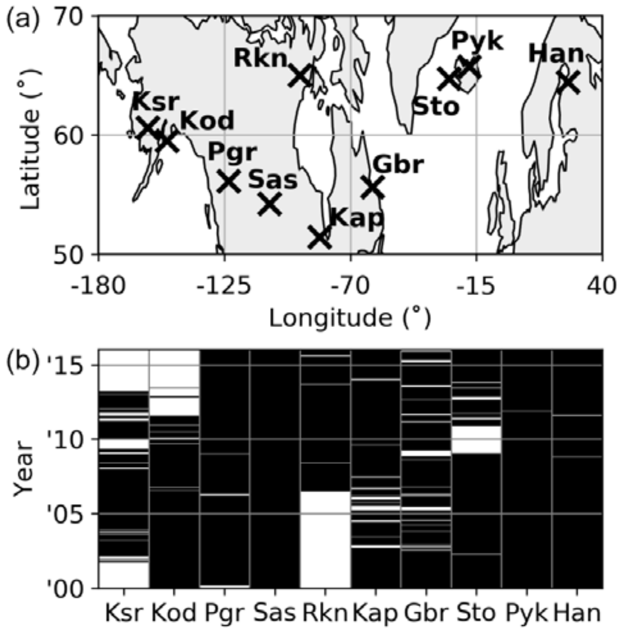

Figure 2.1: (a) Abbreviated names and geographic locations of the SuperDARN radars used in this work, and **(b)** time of operation (black marking) between the years 2000 and 2016 (van Caspel et al. 2020).

westward motion of the sun, the migrating tides are conventionally referred to as the DW1 (Diurnal, Westward S = 1), SW2, and TW3 tides. While the migrating tides have a long history of observational and theoretical study (e.g., Ortland 2017, Hagan et al. 1995, Chapman and Lindzen 1970), observations that are capable of isolating the migrating tides are sparse, and in almost all cases limited to satellite observations. A downside of satellite observations is that they are typically limited by temporal resolutions upwards of 30-60 days, resulting from the asynoptic sampling required to separate the orbital time-longitude aliasing (Salby 1982). A major strength of this longitudinal array of SuperDARN radars is that their time-synchronized hourly measurements can be used to resolve the migrating tides on the time scale of a few days, albeit along a single latitude.

The migrating tides are isolated from the array of SuperDARN wind measurements by least-squares fitting a wave surface representing the DW1, SW2, and TW3 tides, including a mean wind, over a sliding window that is stepped forward in hourly increments. The function describing the migrating tidal wave surface is given by

$$G(\lambda, t) = \sum_{k=1}^{3} A_k \sin(k\,[\Omega t - \lambda] + \phi_k) + G_0, \tag{2.1}$$

where $k = 1, 2, 3$ represent the DW1, SW2, and TW3 tides, respectively, and G_0 is the mean wind. Each fit to the SuperDARN winds yields the average migrating tidal amplitudes and phases over the fitted time interval.

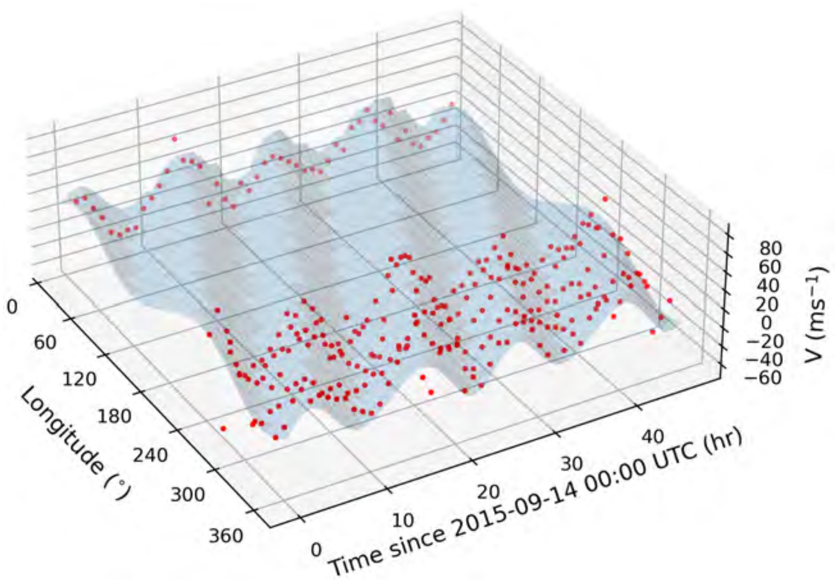

Figure 2.2: Illustration of the fit of Eq. 2.1 to hourly meridional SuperDARN wind measurements (red dots) between the 14th and 16th of September 2015.

Fig. 2.2 illustrates a fit of Eq. 2.1 to SuperDARN meridional wind data between the 14th and 16th of September 2015, where both the SuperDARN winds and the tidal fit can be seen to exhibit a pronounced sun-synchronous semidiurnal variation. The lack of data coverage between roughly 20° and 180° longitude is demonstrated to have little impact on the ability to resolve the migrating tides in Paper I, by means of sampling experiments using horizontal wind data from a high-altitude meteorological analysis system. In these experiments, the migrating tides extracted from the array of SuperDARN radars is also demonstrated to most closely correspond to those at 60°N. Furthermore, while the uncertainty estimates on the hourly winds are not shown in Fig. 2.2, these are typically around 5-15 ms^{-1} for the meridional wind and 10-30 ms^{-1} for the zonal wind components. The higher uncertainty estimates for the zonal winds results from the predominantly poleward orientation of the SuperDARN radar beams.

The method described here to extract the migrating tides from the array of SuperDARN meteor wind measurements is used in Paper I to present a migrating tide climatology based on 16 years of observations. In Paper II the seasonal variations of the observed SW2 tide extracted with this method are used to validate the mechanistic tidal model used to simulate the SW2. In Paper III the simulated short-term variability of the SW2 tide in response to the 2013 major SSW event is also validated against SuperDARN observations.

2.3.1 Migrating Tide Climatologies

Leveraging the unique capabilities of the SuperDARN radar array, Paper I presents an unambiguous climatology of migrating tides based on sixteen years of measurements between the year 2000 and 2016. For this analysis, a 10-day sliding window fit of Eq. 2.1 is used to ensure that the uncertainties on the fitted tidal parameters are negligibly small. Because of the large number of hourly data points included in each fit, which is required to be at least 960, the uncertainties on the fitted parameters become less than 0.5 ms^{-1} and 30 minutes for the tidal amplitudes and phases, respectively.

The resulting migrating tide climatologies are shown in Fig. 2.3. Here the climatological amplitudes are calculated as a 16-year average, while the shading in Fig. 2.3a-c represents the standard deviation around the climatological mean. For the tidal phases, expressed here in terms of their local time of maximum (LTOM), the climatological mean is calculated using the circular mean (Fisher 1995). Notable features of the observed climatologies are that the DW1 is considerably different between its zonal and meridional component, and that the SW2 shows peak amplitudes around day of year 260 and amplitude minima coincident with phase transitions around day of year 75 and 300. The TW3 tide shows a pronounced local amplitude maximum around day of year 265, while its amplitudes generally maximize during winter. The results presented in Paper I find that the year-to-year

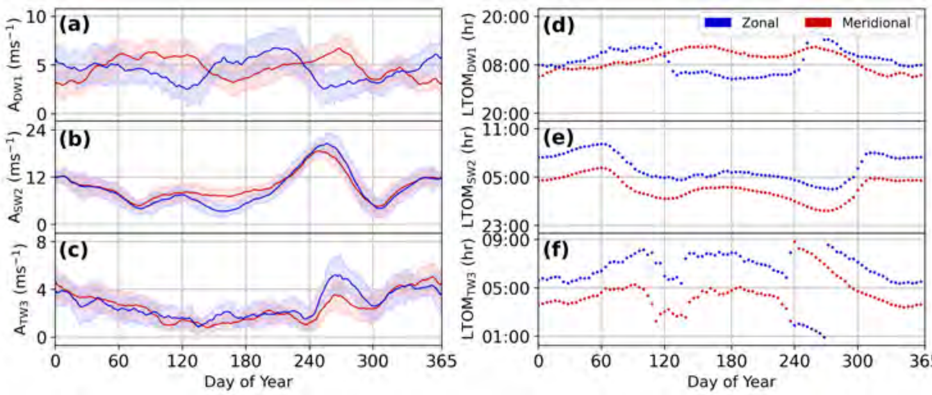

Figure 2.3: Climatologies of the amplitude and phase of the DW1 **(a,d)**, SW2 **(b,e)**, and TW3 **(c,f)** tides based on SuperDARN meridional (red) and zonal (blue) meteor wind measurements between the years 2000 and 2016. Shading marks the standard deviation around the climatological mean. Adapted from van Caspel et al. (2020).

variations of the SW2 and TW3 tides show a strongly repeatable seasonal cycle, while the DW1 shows relatively more inter-annual variability. Since amplitudes of the SW2 tide are typically greater than those of the DW1 and TW3 tides, the SW2 represents the major source of tidal variability at the latitude and altitude of the SuperDARN radar array. This served as an initial motivation to further investigate the SW2 tide by means of mechanistic tide model simulations in order to understand the drivers of its variability, as described in the following chapter.

Chapter 3

Mechanistic Tidal Model

The use of numerical models to simulate Earth's atmosphere forms an essential part of modern day atmospheric and climate science. Numerical models apply the basic equations governing the motion, thermodynamics, and continuity of the atmosphere to describe the behavior of atmospheric motions. By numerically integrating these equations, future states of the atmosphere can be calculated. Similarly, numerical models can be used to simulate atmospheric wave and tidal generation, propagation, and dissipation. For example, one can use numerical models to deduce how the atmosphere responds to a certain thermal or mechanical wave forcing.

Numerical models of atmospheric tides have a history going back to the middle half of the 20th century, as discussed in the review article of Forbes and Garrett (1979). For present day use, tidal models can be divided roughly into three categories. These are two-dimensional steady state models such as the Global Scale Wave Model (GSWM, Hagan et al. 1999), comprehensive whole-atmosphere General Circulation Models (GCMs) (e.g., Pedatella et al. 2020, Stober et al. 2020a, Jin et al. 2012), and mechanistic primitive equation models (e.g., Ortland 2017, McLandress 2002). Steady-state models can offer a detailed insight into the physical mechanisms governing the generation, propagation and dissipation of atmospheric tides. However, given that their numerical solution is obtained by relaxing the equations towards an equilibrium state, it can be a challenge to describe the drivers of short-term tidal variability. In contrast, whole-atmosphere GCMs are well suited for the simulation of short-term tidal variability, generally operating on sub-daily timescales. For these models, however, the complex interactions between chemistry and dynamics make it challenging to identify the specific drivers of the simulated tidal variability. The power of mechanistic primitive equation models is that they can be used to perform time-dependent and whole-atmosphere simulations, while still maintaining full control over the physical mechanisms that determine the tidal simulation results (hence the term 'mechanistic'). They thereby effectively combine many of the benefits of both steady-state and whole-atmosphere general circulation models.

In this thesis, the further development and application of the mechanistic primitive equation in sigma-coordinates model (PRISM) of Ortland (2017) plays a pivotal role. This 'bare-bones' primitive equation model, meaning that it includes only those physical processes relevant to the simulation of atmospheric tides (and other global-scale waves), has been used over the course of two decades to investigate planetary waves and tidal variability. A major strength of the model is that its physical processes can be controlled individually, such that their individual impact on the simulation results can be investigated. For example, Ortland and Alexander (2006) use a linearized version of the model to isolate the impact of gravity-waves on the amplitude and phase of the diurnal tide, while Lieberman et al. (2015) use the model to compute the nonlinear forcing response arising from migrating diurnal tide and planetary wave interactions. As part of this thesis, and as discussed in the following sections, the specification of the background atmosphere through which the tides propagate has been further developed to allow for a three-dimensional rather than zonal-mean specification. For the tidal forcing, the model's thermal forcing has been extended throughout the whole atmosphere, by incorporating heating effects from the ionosphere and from non-local-thermodynamic-equilibrium processes. In addition, a comprehensive gravitational (lunar) tide forcing has been developed, which incorporates the effects of the lunar gravitational potentials, Earth tides, and ocean and load tides.

3.1 Primitive Equations

In principle, the Navier-Stokes equations form the comprehensive set of equations that describe fluid motions in the atmosphere (Temam and Ziane 2005). These equations are, however, highly complex and computationally expensive to numerically solve. For large-scale atmospheric motions, the Navier-Stokes equations can instead be simplified to the so-called primitive equations. While the latter are considerably less complex, they still contain the physics necessary to describe large-scale atmospheric motions, such as the atmospheric tides. The primitive equations are based on the assumption that, 1) the atmosphere comprises a shallow envelope of gas, 2) atmospheric motions are predominantly along the horizontal, 3) the horizontal motions are relatively slow compared to the rotation speed of the Earth. With the first assumption, the distance to the center of the earth is constant for any point in the atmosphere. The second assumption can be used to write the vertical momentum balance in terms of hydrostatic balance, which assumes that the vertical pressure gradient force is always in balance with the gravitational force. With the third assumption, the Coriolis acceleration caused by horizontal motions on a rotating sphere, can be expressed in terms of the Coriolis parameter $f = 2\Omega \sin\phi$. Here the notation is fairly standard, with a complete list of definitions given in the List of Symbols and Abbreviations section of this thesis.

The primitive equations can be written in their Lagrangian form in pressure coordinates as (Holton 2003),

$$\frac{d\vec{u}}{dt} = -f\hat{k} \times \vec{u} - \nabla_H \Phi + \mathrm{F}_u \tag{3.1a}$$

$$\frac{d\Theta}{dt} = \mathrm{F}_T \tag{3.1b}$$

$$0 = \nabla_H \cdot \vec{u} + \frac{\partial \omega}{\partial p} \tag{3.1c}$$

$$\frac{\partial \Phi}{\partial \zeta} = -C_p \Theta, \tag{3.1d}$$

where F_T and F_u represent thermal and mechanical forcing and dissipation terms, respectively, and $\zeta = (p/p_s)^\kappa$ is an auxiliary vertical coordinate. The total derivative is defined as

$$\begin{aligned}\frac{d}{dt} &= \frac{\partial}{\partial t} + \frac{dx}{dt}\frac{\partial}{\partial x} + \frac{dy}{dt}\frac{\partial}{\partial y} + \frac{dp}{dt}\frac{\partial}{\partial p} \\ &= \frac{\partial}{\partial t} + u\frac{\partial}{\partial x} + v\frac{\partial}{\partial y} + \omega\frac{\partial}{\partial p},\end{aligned} \tag{3.2}$$

where $\omega = dp/dt$ represents the vertical velocity in pressure coordinates. The momentum equation given by Eq. 3.1a describes the time-development of the horizontal winds under the effects of the Coriolis force, the horizontal geopotential gradient force, and mechanical forcing or dissipation. The thermodynamic energy equation represented by Eq. 3.1b describes the time-development of the potential temperature when a diabatic forcing or dissipation is applied. Here potential temperature is defined as $\Theta = T(p_s/p)^\kappa$, and represents a conserved quantity for adiabatic motions. The continuity equation given by Eq. 3.1c describes the conservation of mass, while Eq. 3.1d describes hydrostatic balance.

The PRISM model numerically solves the time-development of the primitive equations. To aid the numerical implementation, the model solves the vorticity and divergence form of Eq. 3.1a, reflecting only the notation of the equation. In addition, horizontal variations of any quantity q are represented by a series of spherical harmonics, which is why PRISM is referred to as a spectral model. The model furthermore employs a sigma-coordinate rather than pressure-coordinate system, to simplify the implementation of surface topography. In sigma-coordinates, the vertical levels are defined as σP_s, where $\sigma = 0$ at the model top and $\sigma = 1$ at the surface, and where P_s is the surface pressure in Pascal (Holton 2003). A detailed description of the numerical implementation of the primitive equations for the PRISM model is given by Saravanan (1992). Eq. 3.1a-d nevertheless describe the same physical system as that of the PRISM model, and these equations are therefore referred to in the following sections describing the implementation of the thermal and gravitational tidal forcing.

3.1.1 Tidal Forcing

Diabatic processes are represented in Eq. 3.1b by the F_T term in units of Kelvin per second (K s^{-1}). Diabatic forcing leads to atmospheric heating and cooling, which in turn generates pressure variations. These pressure variations in turn excite horizontal and vertical winds. When this process of wind generation is coupled to the daily insolation cycle, the resulting temperature, pressure and wind perturbations become highly periodic in nature, leading to the excitation of the thermal atmospheric tides.

To excite the thermal tides in PRISM, heating by the daily insolation cycle is specified through the F_T term by incorporating a continuous data set of (hourly or 3-hourly) heating rates from external models. These external temperature tendency fields are interpolated onto the model's temperature tendency equation (Eq. 3.1b), such that the time-integration step generates atmospheric heating and cooling in accordance with the specified heating rates. Using this approach, PRISM does not require the parameterizations of diabatic processes itself, while a mechanistic control over the incorporated heating rates is still maintained. For example, Fig. 3.1 illustrates the heating rates at 50 km altitude from the Specified Dynamics Whole-Atmosphere Community Climate model with Ionospheric Extension v2.1 (SD-WACCMX, Liu et al. 2018), on the 1st of January 2014 at 00:00 UTC, as employed in Paper II (van Caspel et al. 2022b). At this altitude, diabatic heating by shortwave radiation absorption by ozone dominates, although negative temperature tendency rates caused by longwave radiative cooling can also be seen. If desired, the contributions of the short- and longwave radiative forcing can be incorporated separately in the PRISM model, such that their individual contribution to the tidal forcing can be investigated. For example, the whole-atmosphere heating rates from the SD-WACCMX model can be used to assess the individual tidal forcing resulting from short- and longwave radiation, latent heating, gravity wave dissipation, and heating and cooling by NO_x.

Atmospheric tides can also be excited by direct and indirect gravitational effects. These are incorporated in PRISM by specifying the mechanical forcing resulting from the horizontal gradient of the tidally induced geopotential variations through the F_u term in Eq. 3.1a. The implementation considers only the lunar semidi-

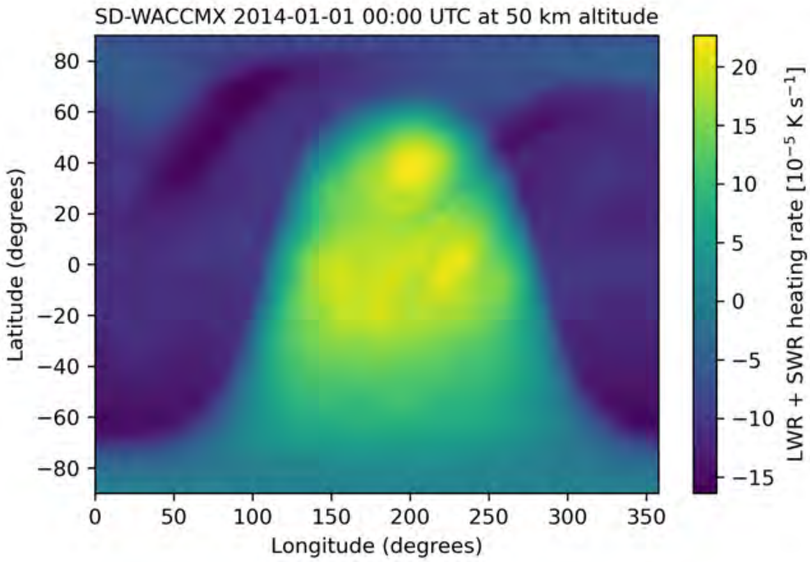

Figure 3.1: SD-WACCMX diabatic heating rates on 2014-01-01 at 00:00 hr and 50 km altitude (∼1 hPa).

urnal tidal components, as the other gravitational tidal components are considerably smaller (Chapman and Lindzen 1970). The direct lunar tide forcing arises from the gravitational pull of the moon on the atmosphere, whose gravitational potential along Earth's surface is described by the classical double tidal bulge (Arons 1979). As the Earth rotates underneath this tidal potential over the course of a solar day, the lunar 12.42 hr M_2 SDT is generated. In addition, the ellipticity of the lunar orbit leads to the generation of the lunar 12.66 hr N_2 SDT, which represents a $\sim$20% variation in the lunar gravitational potential.

As part of this thesis, the PRISM model was developed to include the contributions arising from M_2 and N_2 lunar gravitational potentials, and the 'indirect' contributions arising from the tidally induced vertical motions of the solid Earth and oceans. Together, these represent the largest sources of atmospheric lunar tide excitation (Vial and Forbes 1994). To incorporate the effects of the ocean and load tides, the PRISM model incorporates hourly surface elevation fields from the Finite Element Solution 2014 (FES2014, Lyard et al. 2021) ocean tide atlas. Here the load tide describes the vertical crustal displacement caused by the loading due to the ocean tides, and is typically about an order of magnitude smaller than the ocean tide itself. For illustration, Fig. 3.2 shows the FES2014 lunar semidiurnal ocean tide amplitude for June 2014 conditions, demonstrating that the ocean tide is highly spatially variable. This reflects that the resulting lunar atmospheric tide forcing is also strongly dependent on longitude and latitude. A detailed overview of the lunar tide implementation in PRISM is given by van Caspel et al. (2022a).

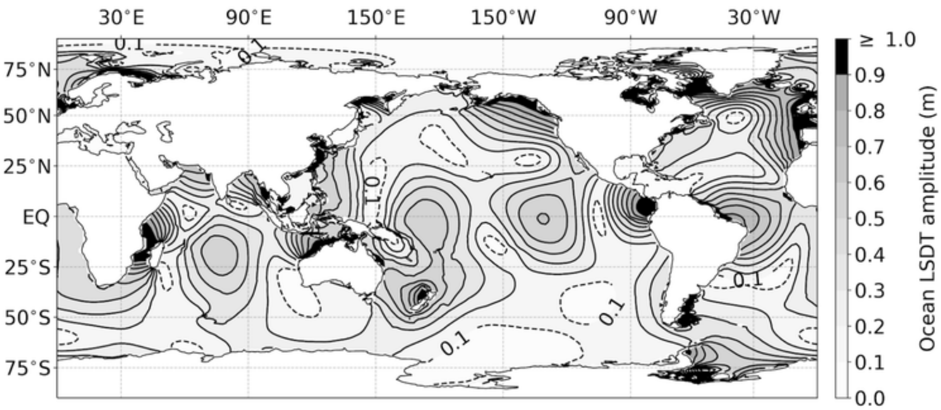

Figure 3.2: Ocean lunar semidiurnal tide amplitude for June 2014 calculated from the FES2014 ocean atlas model.

3.1.2 Specified Dynamics

Atmospheric tides are strongly affected by the background atmosphere through which they propagate. A powerful aspect of the PRISM model is therefore that its background atmosphere can be freely specified, which is achieved by nudging its background atmosphere to that of an external 'assimilation' data set. For example, using an assimilation data set that is either directly based on observations, or on a model that is itself based on observations. As part of this thesis, the assimilation scheme of PRISM has been further developed to be capable of specifying a full three-dimensional atmosphere. With this capability, the impact of quasi-stationary planetary waves on the longitudinal variations of the simulated tides can be isolated, as described in Paper III. The nudging of the model's background winds and temperatures is achieved by considering the additional forcing terms $F_u^\star$ and $F_T^\star$,

$$\mathrm{F}_u^\star = G_u \left(\vec{u}_{input} - \vec{u}_{model}\right) \tag{3.3a}$$

$$\mathrm{F}_T^\star = G_T \left(T_{input} - T_{model}\right), \tag{3.3b}$$

where G_u and G_T represent the momentum and temperature nudging rates in units of days^{-1} (d^{-1}). By incorporating these terms in Eq. 3.1a and 3.1b, respectively, the model's momentum and temperature fields are relaxed towards that of the assimilation data. This is achieved by damping the model state and by forcing the input state, which can, however, have the undesirable effect of also damping the simulated tides. An appropriate nudging rate therefore has to be carefully considered. For the simulation of semidiurnal tides, a nudging rate of $G_u = G_T = 1/3$ d^{-1} was found to be high enough to capture the time development of the daily mean winds of the input atmosphere, while being low enough to have a negligibly small impact on the simulated tides (van Caspel et al. 2022a).

3.2 The Migrating Semidiurnal Tide

In Paper II, the PRISM model was further developed specifically for the simulation of the seasonal variability of the solar thermal SW2 tide, or migrating semidiurnal tide, as observed by the SuperDARN meteor radars. This work was principally motivated to provide an interpretation and attribution of the seasonal SW2 tide variations observed by SuperDARN, which is representative of other mid- and high-latitude SDT observations. By identifying those aspects of the model which most strongly impact the simulated SW2, light can also be shed on why the representation of the SDT can vary considerably from model to model (e.g., McCormack et al. 2021, Pancheva et al. 2020, Stober et al. 2021). The latter is especially important considering that such models are often used to infer the physical processes which lead to the observed variability in the SW2 tide (Pedatella et al. 2020, Conte et al. 2018).

In Paper II, the PRISM model is nudged towards a realistic background atmospheric specification based on the Navy Global Environmental Model – High Altitude (NAVGEM-HA, McCormack et al. 2017) to ensure realistic propagation con-

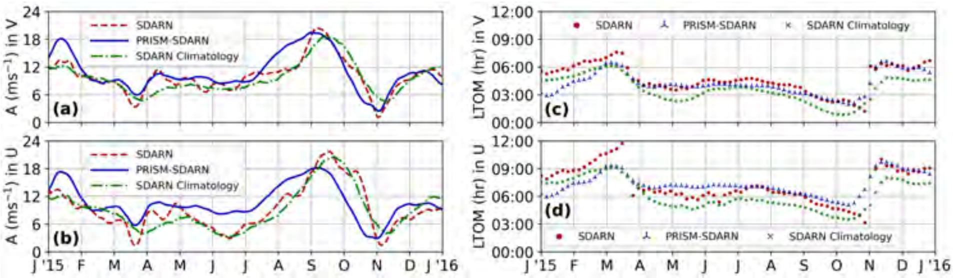

Figure 3.3: Simulated PRISM-SDARN (blue) and observed SuperDARN (SDARN, red) solar SW2 amplitude and phase in the meridional **(a,c** and zonal **(b,d** wind for the year 2015. The climatological observed amplitude and phase based on observations between the years 2000 and 2016 are marked in green.

ditions. A key aspect of the validated NAVGEM-HA analysis system is that it is based on a broad range of satellite observations in the stratosphere and mesosphere, in addition to standard meteorological observations in the troposphere. The tidal dissipation terms in PRISM were also expanded to include the effects of ion drag in the thermosphere, Newtonian cooling in the troposphere and stratosphere, seasonally varying eddy and molecular diffusion of momentum and heat in the MLT, and surface friction. Furthermore, a sampling method was developed to interpolate the model output to the geographical locations of the SuperDARN stations, and applies a vertical averaging kernel representing the SuperDARN meteor echo distribution (a Gaussian centered on 100 km altitude with a FWHM of 30 km). The output of this is termed PRISM-SDARN. Moreover, this sampling technique was also used in Paper IV for the comparison of the mean zonal winds observed by SuperDARN against those simulated by the WACCMX Data Assimilation Research Testbed (WACCMX-DART) model for the 2009 major SSW (Harvey et al. 2021), as discussed in section 4 of this thesis.

Fig. 3.3 compares the simulated SW2 tide (PRISM-SDARN) against observation for the year 2015. The climatological SW2 amplitude and phase from Fig. 2.3 are also included for reference. Here the SW2 tide has been calculated using a 16-day sliding window to limit the effects of quasi-stationary planetary wave interactions and the lunar semidiurnal tide on the observed tidal variations. Fig. 3.3 demonstrates that PRISM-SDARN closely reproduces the observed SW2 amplitude and phase variations for the year 2015, which are also broadly representative of the climatological tidal variations.

Following this validation of the model, Paper II performs a series of numerical experiments to gain insight into the mechanisms of the simulated SW2 tide. For example, these experiments employ a zero-wind atmosphere to investigate the impact of the background atmosphere, and use different dissipation configurations to investigate the impact of eddy diffusion and surface friction. In addition, experiments are performed that focus on the individual SW2 tide response in the MLT resulting from the forcing in the troposphere, stratosphere, and mesosphere-thermosphere regions. The main results of these experiments can be concluded as follows,

1. The seasonal variations in the background zonal winds and temperatures give rise to the seasonal variations in the phase of the SW2. The background atmosphere also gives rise to the amplitude maxima in September and in the winter months, and the amplitude minima in March and October.

2. Contrary to previous thinking, the majority of the sensitivity to the background atmosphere can be attributed to the sensitivity of the SW2 tide forced in the troposphere. The background atmosphere enhances the tropospheric forcing response by up to a factor of 4 in the MLT over a zero-wind simulation, while the SW2 tide forced in the stratosphere is impacted to a much lesser extent.

3. Seasonal variations in the eddy diffusion, driven by dissipating gravity waves, considerably damps the simulated SW2 tide between May and August.

4. An unexpected result was that surface friction enhances the simulated SW2 tide in the MLT region between April and September, with the enhancement being especially pronounced between August and September. This enhancement is identified as being caused by the dampening of the surface reflection of the tide.

There are two results from Paper II that especially stand out. Firstly, that the SW2 tide forced in the troposphere is strongly enhanced by the background atmosphere, making its amplitudes comparable to that of the SW2 tide forced in the stratosphere. While this result is in agreement with the numerical study of Hagan (1996), who finds that the water vapour (troposphere) and ozone (stratosphere) heating responses are comparable in magnitude, the broad consensus is nonetheless that the SW2 is predominantly excited by ozone heating. The results of Paper II thereby represent a first observationally verified confirmation of the results of Hagan (1996). However, a theoretical framework of why the tropospheric forcing response is impacted so much stronger than the stratospheric forcing response is still lacking.

The second result concerns the sensitivity of the simulated SW2 tide to the specification of a narrow surface friction profile. Diagnostic simulations find that the sensitivity to surface friction arises from the dampening of the surface reflection of the tide, which in turn leads to changes in the complex interference pattern between the upward propagating tides and their reflections. The dampening of the surface reflection is surprising, not in the least because tidal dissipation is inversely proportional to the vertical wavelength of the tide (Forbes and Garrett 1979), and the vertical wavelength of the semidiurnal tide is typically very large (50-100 km). The surface friction effect identified in Paper II is also anticipated to serve as a possible excitation mechanism for non-migrating semidiurnal tides, as a more realistic specification of surface friction contains strong ocean and land contrasts (Stevens et al. 2002, Yang et al. 2013).

3.3 Semidiurnal Sudden Stratospheric Warming Response

As part of this thesis, the PRISM model has also been developed to perform a detailed simulation of the SDT response to the 2013 major SSW (van Caspel et al. 2022a). SSWs are large-scale dynamical events in which the wintertime stratospheric polar vortex is disrupted by upwards propagating planetary waves, leading to enhanced meridional flows and compressional heating by tens of degrees of Kelvin in the stratosphere. The warming occurs over the course of a few days, and is accompanied by a reversal of the otherwise climatologically eastward winds of the stratospheric polar vortex. As such, SSWs represent a major perturbation in the wind and temperature structure of the middle atmosphere. Even though the majority of the dynamical changes associated with SSWs take place in the stratosphere, their impact can extend across the entire atmospheric column (Limpasuvan et al.

2016), and even across hemispheres (Lieberman et al. 2021). In addition to the aforementioned effects, models and observations have shown that SSWs induce large changes in the SDT (Baldwin et al. 2021).

The simulation of the SDT response to the 2013 SSW event was motivated in part by a desire to further investigate the contentious role of the lunar SDT component. After the lunar SDT was found to enhance strongly in response to SSWs in early model simulations (Stening et al. 1997), the lunar SDT response developed into a much studied topic. A theoretical framework was set by the so-called Pekeris peak, which describes a resonant response of semidiurnal waves in the presence of a static stability parameter that varies with height (Forbes and Zhang 2012, Platzman 1988). This resonant condition is approached during SSWs, and even more so for the lunar SDT than for the solar SDT, even though their periods are closely spaced. This theoretical framework is supported by a swath of observational analysis showing that the lunar SDT enhances throughout the global MLT and ionosphere system during SSWs, at times even becoming comparable in magnitude to the solar SDT component (e.g., Chau et al. 2015, Zhang and Forbes 2014). However, extracting the short-term variability of the lunar SDT from observation and whole-atmosphere general circulation models is challenging. For example, separating the solar and lunar SDT frequencies requires a time-window of at least 15.3 days (Maute et al. 2016). This places considerable constraints on the temporal resolution of the lunar and solar SDT analysis over the course of SSWs, especially considering that the SSW-induced variability in the SDT can occur on the time scale of a few days (Stober et al. 2020b). Time-frequency analysis effectively assumes the tides to be stationary over the analyzed time window, which is clearly not the case for 15-day time windows of the SDT during SSWs. The latter can in turn easily lead to cross-contamination effects, where variability in the solar SDT 'leaks' into a spurious lunar SDT signal. As a result, variability in the solar SDT can easily be interpreted as being caused by the presence of an enhanced lunar SDT.

To circumvent any lunar and solar SDT cross-contamination effects, in Paper III the PRISM model is used to perform individual simulations of the solar and lunar SDT response to the 2013 major SSW event. The approach of this work is to first validate a detailed simulation of the net SDT response to give confidence in the model efficacy. Once validated, the model is used to simulate the individual solar and lunar SDT response over the course of the same event. To accomplish the latter, a detailed lunar tide forcing was designed and implemented as described in detail in Paper III. In addition, a three-dimensional assimilation scheme was developed to assimilate the temporal development of the polar vortex, as represented in the validated NAVGEM-HA data set (Stober et al. 2020b). With these model capabilities, the PRISM simulations can be used to address open questions regarding the contributions of non-linear wave-wave interactions between the migrating SDT and quasi-stationary planetary waves (Liu et al. 2010), and changes in the tidal forcing brought about by a SSW-induced redistribution of equatorial stratospheric ozone (Goncharenko et al. 2012).

The simulated SDT response is validated against meteor wind measurements from the CMOR (43.3°N, 80.8°W), Collm (51.3°N, 13.0°E), and Kiruna (67.5°N, 20.1°E) radars, in addition to SW2 tide measurements made by the array of SuperDARN radars. For illustrative purposes, focus is placed here on the results for the SDT amplitudes measured at the CMOR radar site. Fig. 3.4a shows the amplitude of the SDT in the zonal wind measured by the CMOR meteor radar, where a 4-day sliding window fit containing a 24-, 12-, and 8-hour wave, including a mean wind, is used on the hourly radar winds. The vertical dashed lines in this figure represent, from left to right, 1) the SSW onset where the zonal mean zonal winds reverse at 70°N and 48 km altitude, 2) the time of peak polar vortex weakening following the definition of Zhang and Forbes (2014), 3) recovery of the zonal mean zonal winds at 70°N and 48 km altitude towards their climatological westerlies. Fig. 3.4a shows that the observed SDT at the CMOR site enhances strongly around 45 days after the 1st of December, reaching amplitudes of up to 70 ms^{-1}. Before this enhancement, roughly between days 35 and 44, amplitudes are at a minimum, with typical values of around 20 ms^{-1}. Fig. 3.4b shows that the PRISM simulation accurately reproduces the observed SDT, where the same analysis is used for the hourly model winds as for the observations. This result gives confidence that the mechanisms controlling the observed SDT response are described realistically in the PRISM model. Leveraging this result, Fig. 3.4c shows a simulation where only the solar thermal forcing is included (OnlySolar). This panel illustrates that the solar SDT component closely follows that of the full PRISM simulation, indicating that the role of the lunar SDT in shaping the net SDT response at the CMOR site is less important. The latter is confirmed by the simulation where only the lunar tide forcing is included (OnlyLunar), shown in Fig. 3.4d, where the lunar SDT reaches amplitudes of at most 12 ms^{-1}. As such, the amplitude of the lunar SDT component at the CMOR site is about 15-20% of that of the solar SDT.

Following the result that the solar SDT dominates, Paper III performs a series of numerical experiments investigating the mechanisms that drive the solar SDT response. These experiments identify the impact of the background atmosphere, quasi-stationary planetary waves, and the SSW-induced redistribution of equatorial stratospheric ozone. The results of these experiments show that nearly all of the solar SDT response is driven by the changing propagation conditions through the background atmosphere, and by non-linear wave-wave interactions between the migrating SDT and quasi-stationary planetary waves.

A possible explanation for the discrepancy between the result for the CMOR radar and the major lunar SDT enhancements described in literature, is the inherent difficulty of separating the lunar and solar SDT components over the course of a SSW event. To illustrate this difficulty, the conventional method of using a 16-day sliding window fit containing both the lunar (12.42 hr) and solar (12.00) hr SDT components is demonstrated in Fig. 3.4e and f. In these panels, the solar and lunar SDT components are calculated using output from the OnlySolar simulation (i.e., no lunar SDT forcing is present). The resulting 'contaminated' lunar tide nevertheless reaches amplitudes of around 25 ms^{-1}, becoming comparable in magnitude to the solar SDT. This behavior of the resulting solar and lunar SDT components is, however, still in qualitative agreement with that of the observed SDT, reaching maximum values roughly between peak polar vortex weakening and the recovery phase onset. These results could therefore easily be interpreted as a major lunar SDT enhancement occurring in response to the SSW, even though no lunar SDTs were included in this experiment. Similar cross-contamination effects may play a role in the (large) lunar SDT enhancements that have often been reported in the literature.

While the lunar SDT is only about 15-20% of that of the solar SDT up to 97 km

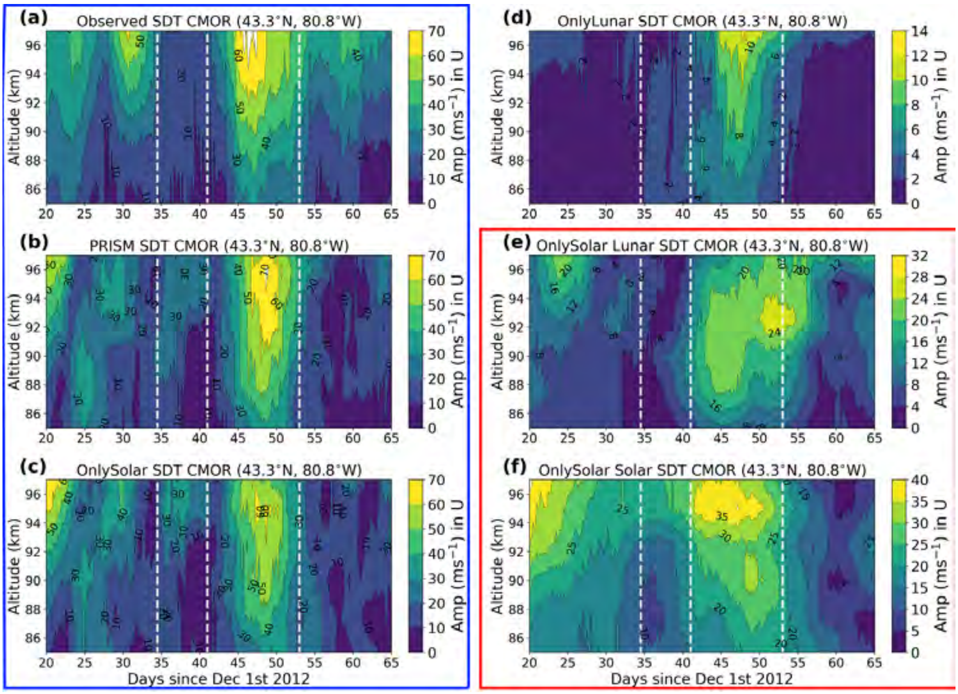

Figure 3.4: Comparison of the SDT amplitude in the zonal wind measured by the CMOR meteor radar **(a)** against the PRISM **(b)** and OnlySolar **(c)** simulations. Panel **(d)** shows the lunar SDT calculated from the OnlyLunar simulation. Panels **(e)** and **(f)** show the lunar and solar SDT calculated from the OnlySolar simulation using a 16-day sliding window.

altitude at the CMOR radar site, the lunar SDT is found to enhance more strongly for altitudes between 105-130 km (van Caspel et al. 2022a). There, the lunar SDT amplitudes can reach closer to 35-40% of that of the solar SDT. Since the SuperDARN meteor echo distribution extends up to 125 km altitude, the simulated SW2 tide as observed by SuperDARN is also impacted more strongly than the CMOR data. This is illustrated in Fig. 3.5, which compares the observed SW2 tide in the zonal wind against PRISM-SDARN, and against the corresponding OnlyLunar-SDARN and OnlySolar-SDARN simulations. Here the suffix SDARN is used to indicate that the model output has been sampled using the SuperDARN observational filter, as described in section 3.2. Furthermore, the migrating tides are calculated here using a 4-day sliding window, with the method described in section 2.3. The shading and error bars in Fig. 3.5 indicate the 2σ uncertainties on the fitted parameters.

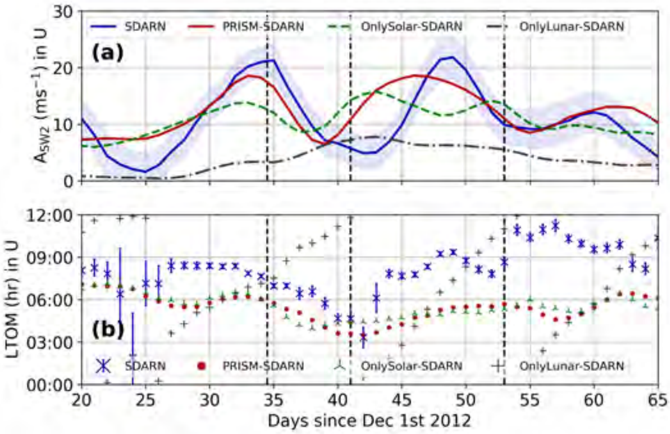

Figure 3.5: Comparison of the amplitude **(a)** and phase **(b)** of the zonal SW2 tide observed by SuperDARN (blue), simulated by PRISM-SDARN (red), and simulated by the OnlySolar-SDARN (green) and OnlyLunar-SDARN (grey) numerical experiments. The shading and error bars represent the 2σ fitting uncertainties on the SuperDARN measurements. The vertical dashed lines mark the SSW onset, peak PVW, and recovery to westerly zonal winds.

In Fig. 3.5b the temporal variations of the simulated phase are found to show good agreement with observation, even though the phase is around 3 hr earlier on average. The lunar SW2 has little to no impact on the net simulated phase. However, Fig. 3.5a illustrates that with the inclusion of the lunar tide, the overall levels and main oscillatory features of the amplitude data are well captured, even though there remains some discrepancy in the magnitude and period of this oscillatory component. Nevertheless, the PRISM-SDARN simulation suggests that the observed quasi 16-day modulation of the migrating semidiurnal tide is caused in part by the beating of the lunar and solar SW2 tides Maute et al. (2016). Following this result, and following the numerical experiments investigating the drivers of the solar SDT response, the main results of Paper III can be summarized as,

1. The validated net SDT response in the mid- and high-latitudes to the 2013 major SSW can be almost entirely attributed to that of the solar SDT component for altitudes below 105 km.

2. In this altitude region the amplitude of the lunar SDT can be greatly overestimated when the solar and lunar SDT components are separated using a

16-day or longer (sliding) time window over the course of the SSW event.

3. Contrasting earlier studies on the impact of equatorial stratospheric ozone, the (solar) SDT response is almost entirely driven by changing propagation conditions through the background atmosphere and by non-linear wave-wave interactions between quasi-stationary planetary waves and the solar SW2 tide.

4. The amplitude of the enhanced lunar tide can be as much as 35-40% of that of the solar SDT for altitudes above around 105 km. As a result, the presence of the lunar SDT considerably improves the model performance when compared to the SW2 tide observed by SuperDARN during the 2013 SSW.

One of the implications of the results presented in Paper III is that the SDT response to the 2013 SSW is strongly dependent on latitude, longitude and altitude. The SDT response at any given location can therefore be anticipated to vary considerably between different SSW events, which in turn can complicate the climatological analysis of the SDT response. The results also raise the question as to what extent the lunar SDT enhancement has been overestimated in earlier literature given the inherent difficulty of separating the lunar and solar SDT components.

Chapter 4

Downward Transport of Nitric Oxide

In Paper II, a sampling technique was developed that interpolates model data to the locations of available SuperDARN meteor wind measurements, and vertically averages the model winds with an averaging kernel representing the SuperDARN meteor echo distribution. The latter is represented by a Gaussian centered on 100 km altitude with a FWHM of 30 km, as discussed in section 3.2. In Paper IV, this sampling technique was applied to hourly simulation output from the WACCMX Data Assimilation Research Testbed (WACCMX-DART) model for the 2009 major SSW (Harvey et al. 2021). The WACCMX-DART model is constrained to assimilated observational data up to an altitude of around 100 km (Pedatella et al. 2014; 2013). For this, radiosonde and satellite drift wind measurements are used in the lower atmosphere, and Sounding of the Atmosphere using Broadband Emission Radiometry (SABER) and Microwave Limb Sounder (MLS) temperature measurements are used between approximately 20-100 km altitude. SuperDARN data is not assimilated, however, making it an independent validation tool of the modeled winds.

In Paper IV, the SuperDARN sampling technique was applied to obtain hourly mean zonal model winds representative of those observed by the SuperDARN radars. The mean winds were obtained using the same method used to resolve the tidal amplitudes and phases, by employing a 4-day sliding window fit containing a 24-, 12-, and 8- hour wave, including a mean wind. The primary goal of this analysis was to validate the longitudinal zonal wind structure in the WACCMX-DART model in order to give confidence in the representation of the high-altitude polar vortex in the model. As shown in Fig. 4.1, the modeled and observed winds are in qualitative agreement, displaying a similar temporal evolution over the course of the SSW event. The modeled winds are, however, around a factor of two stronger than the observed winds, although the winds at the Pykkvibaer radar site in Iceland closely agree.

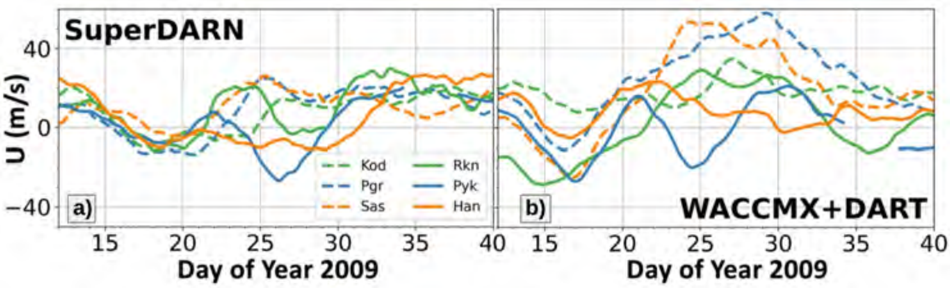

Figure 4.1: Time-series of 4-day average zonal winds near 100 km based on (a) SuperDARN and (b) WACCMX + DART. The six radars are, from west to east, in Kodiac Alaska USA (Kod; 57.6°N, 152.2°W), Prince George British Columbia Canada (Pgr; 54°N, 122.6°W), Saskatoon Saskatchewan Canada (Sas; 52.2°N, 106.5°W), Rankin Inlet Nunavut Canada (Rkn; 62.8°N, 92.1°W), Pykkvibaer Iceland (Pyk; 63.8°N, 20.6°W), and Hankasalmi Finland (Han; 62.3°N, 26.6°E). Adapted from Harvey et al. (2021).

The qualitative agreement between the model and observation gives confidence in the evolution of the zonal winds and synoptic-scale meteorology in the MLT as simulated by the WACCMX-DART model. This result was leveraged to analyse the spatial distribution of nitric oxide (NO) transport by the model's horizontal mean winds, which was furthermore compared to NO volume mixing ratios observed by the Atmospheric Chemistry Experiment Fourier Transform Spectrometer (ACE-FTS, Bernath et al. 2005) and Solar Occultation For Ice Experiment (SOFIE, Gordley et al. 2009). The results of this analysis found that the horizontal transport of NO in the MLT is dictated by highly longitudinally-dependent and coherent horizontal wind structures. Furthermore, the downward transport of NO from the thermosphere into the upper mesosphere ($\sim$75-95 km altitude) was found to be a factor of five greater in the trough of the polar vortex than in the ridge. These results represent the first demonstration of the longitudinal variability in horizontal and vertical transport of NO during an SSW event, which contrasts the conventional view of zonally averaged transport.

Chapter 5

Conclusion and Future Work

The goal of this thesis was to develop a novel observational method for migrating components of the mid- to high-latitude atmospheric tides, and to investigate the drivers of the semidiurnal tidal variability in the MLT. To this end, meteor wind observations from a longitudinal array of 10 SuperDARN radars were used to develop a methodology to unambiguously separate the migrating tides in the mid- to high-latitude MLT. This method is described and validated in detail in Paper I (van Caspel et al. 2020), where it is also used to present a climatology of the migrating tides based on 16 years of observations. For future work, the validated 16-year time series of migrating tide observations can be used to address a range of open questions regarding the drivers of long- and short-term variability of the migrating tides. For example, statistical analysis could be performed between the observed tidal variability and variations in geophysical forcing mechanisms, such as the 27-day periodicity in solar radiation. The latter has been hypothesized to have an impact on the atmospheric tides, although this has not yet been definitively confirmed (Guharay et al. 2020). The long time series of SuperDARN observations also allows for a detailed investigation into the impact of, for example, large-scale atmospheric oscillations such as the quasi-biennial oscillation on the migrating tides (Hibbins et al. 2007). The method and validation steps outlined in Paper I will also contribute to similar analyses of SuperDARN meteor winds from the continuously expanding global network of radars.

The SW2 tide observations presented in Paper I display a pronounced seasonal cycle, with peak amplitudes in September and during the winter months, and amplitude minima coincident with sharp phase transitions in March and October. Paper II (van Caspel et al. 2022b) investigates the driving mechanisms of the seasonal variability of the SW2 tide by means of mechanistic tide model simulations. For this, the tide model from (Ortland 2017) was further developed specifically for the simulation of the SW2 tide as observed by the SuperDARN radars. The resulting simulation shows excellent agreement with observations for the year 2015, which is also representative of the climatological seasonal variations. Through a series of numerical experiments, the seasonal variations of the SW2 tide were determined to be caused largely by the changing propagation conditions through the background atmosphere. This sensitivity is furthermore attributed largely to that of the SW2 tide forced in the troposphere. The simulated seasonal variations are also found to be sensitive to the seasonal variations in mesospheric eddy diffusion, which peaks in strength around summer solstice, and to the specification of a narrow surface friction layer. The impact of the surface friction layer is determined to be caused by its dampening effect on the surface reflection of the tide. Future work can go out to the implementation of a more realistic, spatially varying surface friction specification, which is anticipated to serve as a possible new excitation mechanism of non-migrating tides. The question also remains why the background atmosphere greatly enhances the response of the tropospheric SW2 forcing, but not that of the stratospheric forcing. A future line of research can, for example, investigate this in more detail using the theoretical framework provided by Riggin et al. (2003), together with a Hough mode decomposition of the tide forcing. The latter may indicate how the background atmosphere affects semidiurnal tide modes with different vertical wavelengths differently, while also shedding light on the extent to which 'mode-coupling' by the background atmosphere occurs (Ortland 2005, Lindzen et al. 1977). Better understanding the amplification mechanism of the tropospheric forcing response can have considerable implications for our understanding of how the variability in the troposphere couples to that in the MLT. An additional line of future research can attempt to establish a global picture of the drivers of the seasonal variations in the SW2. This can be achieved by, for example, a comparison of PRISM simulations to the daily estimates of the global temperature SW2 tide from Ortland (2017). Furthermore, while the seasonal variations of the observed SW2 amplitude and phase are investigated in detail in Paper II, the DW1 and TW3 have not yet been examined in a similar manner. Doing so in a future study can shed light on why the DW1 observed by SuperDARN is markedly different between the zonal and meridional winds, and what the causes are for the TW3 amplitude maximum around day of year 265, as described in Paper I.

In Paper III (van Caspel et al. 2022a), the model presented in Paper II is further developed for the simulation of the short-term variability of the SDT in response to the 2013 major SSW. The net simulated SDT response shows good agreement with the SW2 tide observed by the array of SuperDARN radars, and with meteor wind measurements made by the CMOR (43.3°N, 80.8°W), Collm (51.3°N, 13.0°E), and Kiruna (67.5°N, 20.1°E) radars. The net SDT response below around 105 km altitude is found to be almost entirely determined by the solar SDT component, which itself is found to be strongly impacted by the changes in the background atmosphere and by non-linear wave-wave interactions between the SW2 tide and quasi-stationary planetary waves. Above 105 km altitude, enhanced lunar SDT amplitudes are around 35-40% of that of the solar SDT. The presence of the enhanced lunar SDT considerably improves the agreement between the model and SuperDARN observations, whose meteor echo distribution extends up to 125 km altitude. Paper III also demonstrates that the solar SDT can easily cross-contaminate the lunar SDT when attempts are made to separate both components over the course of the SSW event. Future efforts can aim to quantify the cross-contamination effect in other observational tools, such as satellite measurements, to investigate if similar effects occur there. In addition, future efforts can seek to couple the validated PRISM simulation to ionospheric models such as the thermosphere-ionosphere-electrodynamics general circulation model (TIE-GCM, Qian et al. 2014). Such a coupled model would be an invaluable asset in addressing open questions regarding the drivers of the mid- and high-latitude ionospheric response to SSW events (e.g., Goncharenko et al. 2021, Liu et al. 2021b;a, Wu et al. 2019).

In Paper IV (Harvey et al. 2021), the model sampling technique developed in Paper

II is used for the comparison of the mean zonal winds simulated by the WACCMX-DART model and observed by the SuperDARN radars. Good qualitative agreement is established between the simulated and observed mean zonal winds over the course of the 2009 major SSW event, giving confidence in the representation of the high-altitude polar vortex in the WACCMX-DART model. This result, in conjunction with a range of other observational tools, solidifies the conclusion that the downward transport of mesospheric NO_x is about five times stronger in the ridge than in the trough of the polar vortex. Future research will investigate the downward transport mechanism on a climatological scale, to further investigate its dependency on the planetary wave structure of the polar vortex.

Bibliography

D. G. Andrews, J. R. Holton, and C. B. Leovy. *Middle atmosphere dynamics*. Number 40. Academic press, 1987.

A. B. Arons. Basic physics of the semidiurnal lunar tide. *American Journal of Physics*, 47(11):934–937, 1979. doi: https://doi.org/10.1119/1.11614.

M. P. Baldwin, B. Ayarzagüena, T. Birner, N. Butchart, A. H. Butler, A. J. Charlton-Perez, D. I. V. Domeisen, C. I. Garfinkel, H. Garny, E. P. Gerber, M. I. Hegglin, U. Langematz, and N. M. Pedatella. Sudden stratospheric warmings. *Reviews of Geophysics*, 59(1):e2020RG000708, 2021. doi: 10.1029/2020RG000708.

P. F. Bernath, C. T. McElroy, M. C. Abrams, C. D. Boone, M. Butler, C. Camy-Peyret, M. Carleer, C. Clerbaux, P.-F. Coheur, R. Colin, P. DeCola, M. De-Mazière, J. R. Drummond, D. Dufour, W. F. J. Evans, H. Fast, D. Fussen, K. Gilbert, D. E. Jennings, E. J. Llewellyn, R. P. Lowe, E. Mahieu, J. C. McConnell, M. McHugh, S. D. McLeod, R. Michaud, C. Midwinter, R. Nassar, F. Nichitiu, C. Nowlan, C. P. Rinsland, Y. J. Rochon, N. Rowlands, K. Semeniuk, P. Simon, R. Skelton, J. J. Sloan, M.-A. Soucy, K. Strong, P. Tremblay, D. Turnbull, K. A. Walker, I. Walkty, D. A. Wardle, V. Wehrle, R. Zander, and J. Zou. Atmospheric chemistry experiment (ace): Mission overview. *Geophysical Research Letters*, 32(15), 2005. doi: https://doi.org/10.1029/2005GL022386.

D. Bilitza. International reference ionosphere 2000. *Radio Science*, 36(2):261–275, 2001. doi: 10.1029/2000RS002432.

S. Chapman and R. S. Lindzen. *Atmospheric Tides*. Springer Netherlands, 1970. doi: https://doi.org/10.1007/978-94-010-3399-2.

J. L. Chau, P. Hoffmann, N. M. Pedatella, V. Matthias, and G. Stober. Upper mesospheric lunar tides over middle and high latitudes during sudden stratospheric warming events. *Journal of Geophysical Research: Space Physics*, 120 (4):3084–3096, 2015. doi: 10.1002/2015JA020998.

G. Chisham. Calibrating SuperDARN interferometers using meteor backscatter. *Radio Science*, 53(6):761–774, 2018. doi: https://doi.org/10.1029/2017rs006492.

G. Chisham and M. P. Freeman. A reassessment of SuperDARN meteor echoes from the upper mesosphere and lower thermosphere. *Journal of Atmospheric and Solar-Terrestrial Physics*, 102:207–221, 2013. doi: https://doi.org/10.1016/j.jastp.2013.05.018.

J. F. Conte, J. L. Chau, F. I. Laskar, G. Stober, H. Schmidt, and P. Brown. Semidiurnal solar tide differences between fall and spring transition times in the northern hemisphere. *Annales Geophysicae*, 36(4):999–1008, 2018. doi: https://doi.org/10.5194/angeo-36-999-2018.

N. I. Fisher. *Statistical analysis of circular data*. cambridge university press, 1995.

J. M. Forbes. Vertical coupling by the semidiurnal tide in earth's atmosphere. *In T. Tsuda, R. Fujii, K. Shibata, & M. A. Geller (Eds.), Climate and Weather of the Sun-Earth System(CAWSES): Selected Papers from the 2007 Kyoto Symposium(pp. 337–348). Tokyo: TERRAPUB*, 2009.

J. M. Forbes and H. B. Garrett. Theoretical studies of atmospheric tides. *Reviews of Geophysics*, 17(8):1951–1981, 1979. doi: https://doi.org/10.1029/RG017i008p01951.

J. M. Forbes and X. Zhang. Lunar tide amplification during the january 2009 stratosphere warming event: Observations and theory. *Journal of Geophysical Research: Space Physics*, 117(A12), 2012. doi: https://doi.org/10.1029/2012JA017963.

L. P. Goncharenko, A. J. Coster, R. A. Plumb, and D. I. V. Domeisen. The potential role of stratospheric ozone in the stratosphere-ionosphere coupling during stratospheric warmings. *Geophysical Research Letters*, 39(8), 2012. doi: https://doi.org/10.1029/2012GL051261.

L. P. Goncharenko, V. L. Harvey, H. Liu, and N. M. Pedatella. *Sudden Stratospheric Warming Impacts on the Ionosphere–Thermosphere System*, chapter 16, pages 369–400. American Geophysical Union (AGU), 2021. ISBN 9781119815617. doi: https://doi.org/10.1002/9781119815617.ch16.

L. L. Gordley, M. E. Hervig, C. Fish, J. M. Russell, S. Bailey, J. Cook, S. Hansen, A. Shumway, G. Paxton, L. Deaver, T. Marshall, J. Burton, B. Magill, C. Brown, E. Thompson, and J. Kemp. The solar occultation for ice experiment. *Journal of Atmospheric and Solar-Terrestrial Physics*, 71(3):300–315, 2009. ISSN 1364-6826. doi: https://doi.org/10.1016/j.jastp.2008.07.012. Global Perspectives on the Aeronomy of the Summer Mesopause Region.

A. Guharay, P. P. Batista, R. A. Buriti, and N. J. Schuch. Signature of the 27-day oscillation in the mlt tides and its relation with solar radiation at low latitudes. *Earth, Planets and Space*, 72(1):1–10, 2020. doi: https://doi.org/10.1186/s40623-020-01149-7.

M. E. Hagan. Comparative effects of migrating solar sources on tidal signatures in the middle and upper atmosphere. *Journal of Geophysical Research: Atmospheres*, 101(D16):21213–21222, 1996. doi: https://doi.org/10.1029/96jd01374.

M. E. Hagan, J. M. Forbes, and F. Vial. On modeling migrating solar tides. *Geophysical Research Letters*, 22(8):893–896, 1995. doi: https://doi.org/10.1029/95GL00783.

M. E. Hagan, M. D. Burrage, J. M. Forbes, J. Hackney, W. J. Randel, and X. Zhang. GSWM-98: Results for migrating solar tides. *Journal of Geophysical Research: Space Physics*, 104(A4):6813–6827, 1999. doi: https://doi.org/10.1029/1998ja900125.

G. E. Hall, J. W. MacDougall, D. R. Moorcroft, J.-P. St.-Maurice, A. H. Manson, and C. E. Meek. Super dual auroral radar network observations of meteor echoes. *Journal of Geophysical Research: Space Physics*, 102(A7):14603–14614, jan 1997. doi: 10.1029/97ja00517.

V. L. Harvey, S. Datta-Barua, N. M. Pedatella, N. Wang, C. E. Randall, D. E. Siskind, and W. E. van Caspel. Transport of nitric oxide via lagrangian coherent structures into the top of the polar vortex. *Journal of Geophysical Research: Atmospheres*, 126(11):e2020JD034523, 2021. doi: https://doi.org/10.1029/2020JD034523.

R. E. Hibbins, P. J. Espy, and M. J. Jarvis. Quasi-biennial modulation of the semidiurnal tide in the upper mesosphere above halley, antarctica. *Geophysical Research Letters*, 34(21), 2007. doi: https://doi.org/10.1029/2007GL031282.

R. E. Hibbins, P. J. Espy, Y. J. Orsolini, V. Limpasuvan, and R. J. Barnes. Superdarn observations of semidiurnal tidal variability in the mlt and the response to sudden stratospheric warming events. *Journal of Geophysical Research: Atmospheres*, 124(9):4862–4872, 2019. doi: https://doi.org/10.1029/2018JD030157.

J. R. Holton. The role of gravity wave induced drag and diffusion in the momentum budget of the mesosphere. *Journal of Atmospheric Sciences*, 39(4):791 – 799, 1982. doi: 10.1175/1520-0469(1982)039<0791:TROGWI>2.0.CO;2.

J. R. Holton. *An Introduction to Dynamic Meteorology: Fourth Edition*. Academic Press, 2003.

H. Jin, Y. Miyoshi, D. Pancheva, P. Mukhtarov, H. Fujiwara, and H. Shinagawa. Response of migrating tides to the stratospheric sudden warming in 2009 and their effects on the ionosphere studied by a whole atmosphere-ionosphere model gaia with cosmic and timed/saber observations. *Journal of Geophysical Research: Space Physics*, 117(A10), 2012. doi: https://doi.org/10.1029/2012JA017650.

N. H. Kleinknecht, P. J. Espy, and R. E. Hibbins. The climatology of zonal wave numbers 1 and 2 planetary wave structure in the mlt using a chain of northern hemisphere superdarn radars. *Journal of Geophysical Research: Atmospheres*, 119(3):1292–1307, 2014. doi: https://doi.org/10.1002/2013JD019850.

R. S. Lieberman, D. M. Riggin, D. A. Ortland, J. Oberheide, and D. E. Siskind. Global observations and modeling of nonmigrating diurnal tides generated by tide-planetary wave interactions. *Journal of Geophysical Research: Atmospheres*, 120(22):11,419–11,437, 2015. doi: https://doi.org/10.1002/2015JD023739.

R. S. Lieberman, J. France, D. A. Ortland, and S. D. Eckermann. The role of inertial instability in cross-hemispheric coupling. *Journal of the Atmospheric Sciences*, 78(4):1113 – 1127, 2021. doi: 10.1175/JAS-D-20-0119.1.

V. Limpasuvan, Y. J. Orsolini, A. Chandran, R. R. Garcia, and A. K. Smith. On the composite response of the mlt to major sudden stratospheric warming events with elevated stratopause. *Journal of Geophysical Research: Atmospheres*, 121(9):4518–4537, 2016. doi: https://doi.org/10.1002/2015JD024401.

R. S. Lindzen, S. shung Hong, and J. Forbes. Semidiurnal hough mode extensions in the thermosphere and their application. Technical report, feb 1977.

G. Liu, R. S. Lieberman, V. L. Harvey, N. M. Pedatella, J. Oberheide, R. E. Hibbins, P. J. Espy, and D. Janches. Tidal variations in the mesosphere and lower thermosphere before, during, and after the 2009 sudden stratospheric warming. *Journal of Geophysical Research: Space Physics*, 126(3):e2020JA028827, 2021a. doi: https://doi.org/10.1029/2020JA028827.

H.-L. Liu, W. Wang, A. D. Richmond, and R. G. Roble. Ionospheric variability due to planetary waves and tides for solar minimum conditions. *Journal of Geophysical Research: Space Physics*, 115(A6), 2010. doi: https://doi.org/10.1029/2009JA015188.

H.-L. Liu, C. G. Bardeen, B. T. Foster, P. Lauritzen, J. Liu, G. Lu, D. R. Marsh, A. Maute, J. M. McInerney, N. M. Pedatella, L. Qian, A. D. Richmond, R. G. Roble, S. C. Solomon, F. M. Vitt, and W. Wang. Development and validation of the whole atmosphere community climate model with thermosphere and ionosphere extension (WACCM-x 2.0). *Journal of Advances in Modeling Earth Systems*, 10(2):381–402, 2018. doi: https://doi.org/10.1002/2017ms001232.

J. Liu, D. Zhang, L. P. Goncharenko, S.-R. Zhang, M. He, Y. Hao, and Z. Xiao. The latitudinal variation and hemispheric asymmetry of the ionospheric lunitidal signatures in the american sector during major sudden stratospheric warming events. *Journal of Geophysical Research: Space Physics*, 126(5):e2020JA028859, 2021b. doi: https://doi.org/10.1029/2020JA028859.

F. H. Lyard, D. J. Allain, M. Cancet, L. Carrère, and N. Picot. Fes2014 global ocean tide atlas: design and performance. *Ocean Science*, 17(3):615–649, 2021. doi: 10.5194/os-17-615-2021.

T. Matsuno. A dynamical model of the stratospheric sudden warming. *Journal of Atmospheric Sciences*, 28(8):1479 – 1494, 1971. doi: 10.1175/1520-0469(1971)028<1479:ADMOTS>2.0.CO;2.

A. Maute, B. G. Fejer, J. M. Forbes, X. Zhang, and V. Yudin. Equatorial vertical drift modulation by the lunar and solar semidiurnal tides during the 2013 sudden stratospheric warming. *Journal of Geophysical Research: Space Physics*, 121(2):1658–1668, 2016. doi: https://doi.org/10.1002/2015JA022056.

J. P. McCormack, K. Hoppel, D. Kuhl, R. de Wit, G. Stober, P. Espy, N. Baker, P. Brown, D. Fritts, C. Jacobi, D. Janches, N. Mitchell, B. Ruston, S. Swadley, K. Viner, T. Whitcomb, and R. Hibbins. Comparison of mesospheric winds from a high-altitude meteorological analysis system and meteor radar observations during the boreal winters of 2009–2010 and 2012–2013. *Journal of Atmospheric and Solar-Terrestrial Physics*, 154:132–166, 2017. doi: https://doi.org/10.1016/j.jastp.2016.12.007.

J. P. McCormack, V. L. Harvey, N. Pedatella, D. Koshin, K. Sato, L. Coy, S. Watanabe, C. E. Randall, F. Sassi, and L. A. Holt. Intercomparison of middle atmospheric meteorological analyses for the northern hemisphere winter 2009-2010. *Atmospheric Chemistry and Physics Discussions*, 2021:1–48, 2021. doi: https://doi.org/10.5194/acp-2021-224.

C. McLandress. The seasonal variation of the propagating diurnal tide in the mesosphere and lower thermosphere. part ii: The role of tidal heating and zonal mean winds. *Journal of the Atmospheric Sciences*, 59(5):907 – 922, 2002. doi: https://doi.org/10.1175/1520-0469(2002)059<0907:TSVOTP>2.0.CO;2.

D. A. Ortland. A study of the global structure of the migrating diurnal tide using generalized hough modes. *Journal of the Atmospheric Sciences*, 62(8), 2005. doi: 10.1175/JAS3501.1.

D. A. Ortland. Daily estimates of the migrating tide and zonal mean temperature in the mesosphere and lower thermosphere derived from saber data. *Journal of Geophysical Research: Atmospheres*, 122(7):3754–3785, 2017. doi: https://doi.org/10.1002/2016JD025573.

D. A. Ortland and M. J. Alexander. Gravity wave influence on the global structure of the diurnal tide in the mesosphere and lower thermosphere. *Journal of Geophysical Research: Space Physics*, 111(A10), 2006. doi: 10.1029/2005JA011467.

D. Pancheva, P. Mukhtarov, C. Hall, C. Meek, M. Tsutsumi, N. Pedatella, and S. Climatology of the main (24-h and 12-h) tides observed by meteor radars at svalbard and tromsø: Comparison with the models cmam-das and waccm-x. *Journal of Atmospheric and Solar-Terrestrial Physics*, 207:105339, 2020. ISSN 1364-6826. doi: https://doi.org/10.1016/j.jastp.2020.105339.

N. M. Pedatella and J. M. Forbes. Evidence for stratosphere sudden warming-ionosphere coupling due to vertically propagating tides. *Geophysical Research Letters*, 37(11), 2010. doi: https://doi.org/10.1029/2010GL043560.

N. M. Pedatella, K. Raeder, J. L. Anderson, and H.-L. Liu. Application of data assimilation in the whole atmosphere community climate model to the study of day-to-day variability in the middle and upper atmosphere. *Geophysical Research Letters*, 40(16):4469–4474, 2013. doi: https://doi.org/10.1002/grl.50884.

N. M. Pedatella, K. Raeder, J. L. Anderson, and H.-L. Liu. Ensemble data assimilation in the whole atmosphere community climate model. *Journal of*

Geophysical Research: Atmospheres, 119(16):9793–9809, 2014. doi: https://doi.org/10.1002/2014JD021776.

N. M. Pedatella, H.-L. Liu, J. F. Conte, J. L. Chau, C. Hall, C. Jacobi, N. Mitchell, and M. Tsutsumi. Migrating semidiurnal tide during the september equinox transition in the northern hemisphere. *Journal of Geophysical Research: Atmospheres*, page e2020JD033822, 2020. doi: https://doi.org/10.1029/2020JD033822.

J. M. Picone, A. E. Hedin, D. P. Drob, and A. C. Aikin. Nrlmsise-00 empirical model of the atmosphere: Statistical comparisons and scientific issues. *Journal of Geophysical Research: Space Physics*, 107(A12):SIA 15–1–SIA 15–16, 2002. doi: https://doi.org/10.1029/2002JA009430.

G. W. Platzman. The atmospheric tide as a continuous spectrum: Lunar semidiurnal tide in surface pressure. *Meteorology and Atmospheric Physics*, 38(1-2): 70–88, 1988. doi: 10.1007/bf01029949.

R. A. Plumb and R. C. Bell. A model of the quasi-biennial oscillation on an equatorial beta-plane. *Quarterly Journal of the Royal Meteorological Society*, 108(456):335–352, 1982. doi: https://doi.org/10.1002/qj.49710845604.

L. Qian, A. G. Burns, B. A. Emery, B. Foster, G. Lu, A. Maute, A. D. Richmond, R. G. Roble, S. C. Solomon, and W. Wang. The ncar tie-gcm: A community model of the coupled thermosphere/ionosphere system. *Modeling the ionosphere-thermosphere system*, 201:73–83, 2014. doi: https://doi.org/10.1002/9781118704417.ch7.

I. M. Reid. MF and HF radar techniques for investigating the dynamics and structure of the 50 to 110 km height region: a review. *Progress in Earth and Planetary Science*, 2(1), oct 2015. doi: 10.1186/s40645-015-0060-7.

D. Riggin, C. Meyer, D. Fritts, M. Jarvis, Y. Murayama, W. Singer, R. Vincent, and D. Murphy. Mf radar observations of seasonal variability of semidiurnal motions in the mesosphere at high northern and southern latitudes. *Journal of Atmospheric and Solar-Terrestrial Physics*, 65(4):483–493, 2003. ISSN 1364-6826. doi: https://doi.org/10.1016/S1364-6826(02)00340-1.

M. L. Salby. Sampling theory for asynoptic satellite observations. part i: Space-time spectra, resolution, and aliasing. *Journal of Atmospheric Sciences*, 39(11): 2577 – 2600, 1982. doi: 10.1175/1520-0469(1982)039<2577:STFASO>2.0.CO;2.

R. Saravanan. An idealized primitive equation model. *Article available upon request.* 1992.

R. J. Stening, J. M. Forbes, M. E. Hagan, and A. D. Richmond. Experiments with a lunar atmospheric tidal model. *Journal of Geophysical Research: Atmospheres*, 102(D12):13465–13471, 1997. doi: https://doi.org/10.1029/97JD00778.

B. Stevens, J. Duan, J. C. McWilliams, M. Münnich, and J. D. Neelin. Entrainment, rayleigh friction, and boundary layer winds over the tropical pacific. *Journal of climate*, 15(1):30–44, 2002. doi: https://doi.org/10.1175/1520-0442(2002)015<0030:ERFABL>2.0.CO;2.

G. Stober, K. Baumgarten, J. P. McCormack, P. Brown, and J. Czarnecki. Comparative study between ground-based observations and navgem-ha analysis data in the mesosphere and lower thermosphere region. *Atmospheric Chemistry and Physics*, 20(20):11979–12010, 2020a. doi: https://doi.org/10.5194/acp-20-11979-2020.

G. Stober, K. Baumgarten, J. P. McCormack, P. Brown, and J. Czarnecki. Comparative study between ground-based observations and navgem-ha analysis data in the mesosphere and lower thermosphere region. *Atmospheric Chemistry and Physics*, 20(20):11979–12010, 2020b. doi: 10.5194/acp-20-11979-2020.

G. Stober, A. Kuchar, D. Pokhotelov, H. Liu, H.-L. Liu, H. Schmidt, C. Jacobi, K. Baumgarten, P. Brown, D. Janches, D. Murphy, A. Kozlovsky, M. Lester, E. Belova, and J. Kero. Interhemispheric differences of mesosphere/lower thermosphere winds and tides investigated from three whole atmosphere models and meteor radar observations. *Atmospheric Chemistry and Physics Discussions*, 2021:1–50, 2021. doi: https://doi.org/10.5194/acp-2021-142.

R. Temam and M. Ziane. Chapter 6 - some mathematical problems in geophysical fluid dynamics. volume 3 of *Handbook of Mathematical Fluid Dynamics*, pages 535–658. North-Holland, 2005. doi: https://doi.org/10.1016/S1874-5792(05)80009-6.

W. E. van Caspel, P. J. Espy, R. E. Hibbins, and J. P. McCormack. Migrating tide climatologies measured by a high-latitude array of SuperDARN HF radars. *Annales Geophysicae*, 38(6):1257–1265, 2020. doi: https://doi.org/10.5194/angeo-38-1257-2020.

W. E. van Caspel, P. J. Espy, R. E. Hibbins, G. Stober, P. Brown, C. Jacobi, J. Kero, and E. Belova. A case study of the solar and lunar semidiurnal tide response to the 2013 major sudden stratospheric warming event. Manuscript prepared for submission to: *Journal of Geophysical Research: Atmospheres*, 2022a.

W. E. van Caspel, P. J. Espy, D. A. Ortland, and R. E. Hibbins. The mid- to high-latitude migrating semidiurnal tide: Results from a mechanistic tide model and superdarn observations. *Journal of Geophysical Research: Atmospheres*, 127 (1):e2021JD036007, 2022b. doi: https://doi.org/10.1029/2021JD036007.

F. Vial and J. Forbes. Monthly simulations of the lunar semi-diurnal tide. *Journal of Atmospheric and Terrestrial Physics*, 56(12):1591–1607, 1994. ISSN 0021-9169. doi: https://doi.org/10.1016/0021-9169(94)90089-2.

Q. Wu, W. Ward, S. Kristoffersen, A. Maute, and J. Liu. Simulation and observation of lunar tide effect on high-latitude, mesospheric and lower thermospheric winds during the 2013 sudden stratospheric warming event. *Journal of Geophysical Research: Space Physics*, 124(2):1283–1291, 2019. doi: https://doi.org/10.1029/2018JA025476.

Y. Yamazaki and A. Maute. Sq and eej—a review on the daily variation of the geomagnetic field caused by ionospheric dynamo currents. *Space Science Reviews*, 206(1-4):299–405, 2017. doi: https://doi.org/10.1007/s11214-016-0282-z.

W. Yang, R. Seager, and M. A. Cane. Zonal momentum balance in the tropical atmospheric circulation during the global monsoon mature months. *Journal of the Atmospheric Sciences*, 70(2):583–599, 2013. doi: https://doi.org/10.1175/jas-d-12-0140.1.

E. Yiğit, P. Koucká Knížová, K. Georgieva, and W. Ward. A review of vertical coupling in the atmosphere–ionosphere system: Effects of waves, sudden stratospheric warmings, space weather, and of solar activity. *Journal of Atmospheric and Solar-Terrestrial Physics*, 141:1–12, 2016. ISSN 1364-6826. doi: https://doi.org/10.1016/j.jastp.2016.02.011. SI:Vertical Coupling.

X. Zhang and J. M. Forbes. Lunar tide in the thermosphere and weakening of the northern polar vortex. *Geophysical Research Letters*, 41(23):8201–8207, 2014. doi: 10.1002/2014GL062103.

Chapter 6

Publications

Paper I

van Caspel, W. E., Espy, P. J., Hibbins, R. E., & McCormack, J. P. (2020). Migrating tide climatologies measured by a high-latitude array of SuperDARN HF radars. *Annales Geophysicae* (Vol. 38, No. 6, pp. 1257-1265). https://doi.org/10.5194angeo-38-1257-2020

Note: The analysis used to calculate the tidal phases shown in Figures 3, 4, and 5 of this paper, has been found to contain an error. While the mean phase over the plotted time intervals is shown correctly, the variations around the mean should be mirrored. The corrected figures have been prepared for submission as an erratum to Annales Geophysicae, and have no implications for the conclusions of this work.

Ann. Geophys., 38, 1257–1265, 2020
https://doi.org/10.5194/angeo-38-1257-2020

Annales Geophysicae
Open Access

Migrating tide climatologies measured by a high-latitude array of SuperDARN HF radars

Willem E. van Caspel[1,2], **Patrick J. Espy**[1,2], **Robert E. Hibbins**[1,2], **and John P. McCormack**[3]

[1]Department of Physics, Norwegian University of Science and Technology (NTNU), Trondheim, Norway
[2]Birkeland Centre for Space Science, Bergen, Norway
[3]Space Science Division, Naval Research Laboratory, Washington DC, USA

Correspondence: Willem E. van Caspel (willem.e.v.caspel@ntnu.no)

Received: 3 July 2020 – Discussion started: 9 July 2020
Revised: 16 October 2020 – Accepted: 30 October 2020 – Published: 21 December 2020

Abstract. This study uses hourly meteor wind measurements from a longitudinal array of 10 high-latitude SuperDARN high-frequency (HF) radars to isolate the migrating diurnal, semidiurnal, and terdiurnal tides at mesosphere–lower-thermosphere (MLT) altitudes. The planetary-scale array of radars covers 180° of longitude, with 8 out of 10 radars being in near-continuous operation since the year 2000. Time series spanning 16 years of tidal amplitudes and phases in both zonal and meridional wind are presented, along with their respective annual climatologies. The method to isolate the migrating tides from SuperDARN meteor winds is validated using 2 years of winds from a high-altitude meteorological analysis system. The validation steps demonstrate that, given the geographical spread of the radar stations, the derived tidal modes are most closely representative of the migrating tides at 60° N. Some of the main characteristics of the observed migrating tides are that the semidiurnal tide shows sharp phase jumps around the equinoxes and peak amplitudes during early fall and that the terdiurnal tide shows a pronounced secondary amplitude peak around day of year (DOY) 265. In addition, the diurnal tide is found to show a bi-modal circular polarization phase relation between summer and winter.

1 Introduction

Atmospheric tides are global-scale waves excited primarily by radiative and latent heating effects in the troposphere and stratosphere (Chapman and Lindzen, 2012). The tides have a latitudinal spherical harmonic structure (termed Hough modes) and longitudinal zonal wavenumber (S) structure, and in the absence of dissipation their amplitudes increase exponentially with altitude due to the decreasing density of the atmosphere. In the mid- to high-latitude mesosphere–lower-thermosphere (MLT), tides are an important driver of short- and long-term variability in the winds, temperatures, and densities (Smith, 2012). The migrating diurnal (DW1; for diurnal, westward, $S = 1$), semidiurnal (SW2), and terdiurnal (TW3) tides are most closely tied to the daily insolation cycle, following the apparent motion of the sun with periods of oscillation of 24, 12, and 8 h, respectively. Non-migrating tides are waves whose periods of oscillation are also an integer fraction of a solar day but whose phase velocities are not sun-synchronous.

Observations capable of separating the longitudinal structure of the migrating tides from the non-migrating components have remained sparse, with the exception of satellites (e.g., Garcia et al., 2005; Ortland, 2017; Pancheva and Mukhtarov, 2011). Typical drawbacks associated with satellite measurements arise due to constraints imposed by asynoptic sampling (Salby, 1982), including slow local time precession and yaw cycle maneuvers. Single station tidal measurements using medium-frequency (MF), high-frequency (HF), or very-high-frequency (VHF) radars have been numerous (Reid, 2015), but because they lack longitudinal coverage, the migrating and non-migrating tides are aliased to a single local wave with an integer fraction of a solar day period. Such spatial aliasing is especially problematic when migrating and non-migrating tides are known to have different seasonal cycles (Sakazaki et al., 2018; Hibbins et al., 2019). A planetary-scale longitudinal chain of time-synchronized measurements can potentially bypass most, if not all, of the drawbacks associated with satellite and single station tide measurements, albeit along a single latitude. The array of SuperDARN (SD) radars used in this study is unique in that it covers 180° of longitude along a latitude band centered around 60° N and that 8 of the 10 radars have been providing hourly meteor wind measurements of the MLT near-continuously since the year 2000. As a result of the simultaneous temporal and spatial sampling by the SD radars, unambiguous amplitudes and phases of the migrating diurnal, semidiurnal, and terdiurnal tides can be isolated.

The following section gives a description of the data and method used to extract the migrating tides from the SD meteor winds. Section 3 presents time series spanning 16 years of hourly tidal amplitudes and phases in both the zonal and meridional winds, in addition to their respective annual climatologies. The method to extract migrating tides from the SD meteor winds is validated in Sect. 4 by means of sampling experiments with winds obtained from the NAVGEM-HA (Navy Global Environmental Model – High Altitude) meteorological analysis system, addressing the geographical spread and changing availability in time of the SD radars. Lastly, the results are discussed in Sect. 5.

2 Data and methodology

2.1 SuperDARN meteor winds

Figure 1 shows the geographical location and data availability between the years 2000 and 2016 of the 10 SD radars used in this study. The SD radars operate in a 10–15 MHz frequency band and are designed to measure ionospheric E- and F-region plasma phenomena. However, they also detect near-range meteor echoes in the first four range gates that can be used to determine neutral horizontal wind velocities (Hall et al., 1997). The phase shift of the return signal of each meteor echo is a measure of the component of the neutral wind velocity along the line of sight. An hourly mean horizontal wind vector is constructed from the aggregate line-of-sight wind vectors, over a 45° spread in azimuth, using a singular value decomposition (SVD). While the line-of-sight velocities are typically very well defined (errors below $1\,\mathrm{m\,s^{-1}}$, Chisham and Freeman, 2013), the SVD is applied only to line-of-sight velocities with a signal-to-noise ratio greater than 3.0 dB and a spectral width of at most $25\,\mathrm{m\,s^{-1}}$, to reduce contamination by sources such as auroral and sporadic E-region echoes. In addition to a hourly horizontal wind vector, the SVD also yields the standard deviation of the hourly winds, which typically ranges between 5 and $15\,\mathrm{m\,s^{-1}}$ for the meridional wind and between 10 and $30\,\mathrm{m\,s^{-1}}$ for the zonal wind. The seasonal mean vertical distribution of meteor echoes as observed by the SD radars is a Gaussian centered on 102–103 km altitude, extending from approximately 75 to 125 km altitude with a full width at half maximum of

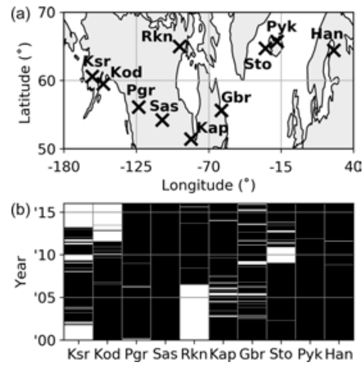

Figure 1. Abbreviated names and geographic locations **(a)** and time of operation between the years 2000 and 2016 (black marking **b**) of the SuperDARN radars used in this study.

25–35 km (Chisham and Freeman, 2013; Chisham, 2018). The SD meteor winds therefore represent a broad vertical average, which in earlier studies has been found to best correlate with neutral winds measured by traditional MF and meteor radars around 95 km altitude (Hall et al., 1997; Arnold et al., 2003).

On average each hourly SD meteor wind measurement is based on ∼ 700 meteor echoes. Before extracting the migrating tides, however, measurements based on fewer than 75 meteor echoes are discarded, as are those resulting from non-standard modes of operation. The latter amounts to discarding winds with absolute values above $100\,\mathrm{m\,s^{-1}}$ and winds fitted with a zero standard deviation (following Hibbins and Jarvis, 2008). The lower limit on the number of meteor echoes is to ensure quality of the fitted winds. Caution has been taken to ensure that no spurious tidal signals are introduced by the quality check, which may arise due to the diurnal cycle in meteor detections. This was verified by replacing all remaining data points with a value of $1\,\mathrm{m\,s^{-1}}$ and then performing spectral analysis as outlined in the following section, to confirm that tidal spectral contamination remains negligibly small.

2.2 Fourier analysis

The amplitude and phase of DW1, SW2, and TW3 are calculated by least-squares fitting the function $G(\lambda,t)$ in both space and time, where $G(\lambda,t)$ represents the migrating tides along with a mean wind, given by

$$G(\lambda,t)=\sum_{k=1}^{3}A_k\sin(k\,[\Omega t-\lambda]+\phi_k)+G_0, \qquad (1)$$

where $k=1,2,3$ represent DW1, SW2, and TW3, respectively, $\Omega=2\pi/24\,\mathrm{h}^{-1}$; λ is the geographic longitude in radians; and G_0 is the mean wind. The time development is determined by fitting $G(\lambda,t)$ over a 10 d window that is stepped forward in time with hourly steps over the range of available data. A 10 d window length is chosen such that each fit contains a proportionally sufficient number of data points to reliably extract the seasonal characteristics of the tides, without overly smoothing short-term variability.

The equidistant longitudinal spread of measurements is optimized over the range of available data to prevent skewing the fit to any particular longitude sector. To that end, for the radar pairs closely spaced in longitude, (Ksr, Kod), (Rnk, Kap), and (Sto, Pyk), only one of each of the pairs' measurements is used in the fit to Eq. (1), even if data are available for both. After performing the quality check and optimizing the longitudinal spread, fits are rejected if fewer than 960 hourly data points are present over the 10 d period, corresponding to an average continuous uptime of at least four radar stations. As a result of requiring a minimum of 960 hourly data points in each fit to Eq. (1), the estimated uncertainties on the fitted parameters become negligibly small (on the order of $0.5\,\mathrm{m\,s^{-1}}$ for the tidal amplitudes when employing the standard deviations of the hourly winds as an estimate of the measurement errors).

2.3 NAVGEM-HA

NAVGEM-HA is a data assimilation and modeling system that extends from the surface to the lower thermosphere. In addition to standard operational meteorological observations in the troposphere and stratosphere, NAVGEM-HA assimilates satellite-based observations of temperature, ozone, and water vapor in the stratosphere, mesosphere, and lower thermosphere (McCormack et al., 2017). NAVGEM-HA output is on a 1° latitude and longitude grid with a temporal frequency of 3 h, staying above the spatial and temporal Nyquist frequency of the tides studied in this work. For comparison with ground-based instruments, vertical profiles of NAVGEM-HA analyzed winds and temperatures are converted from the model vertical grid in geopotential altitude to a geometric altitude grid. To date, NAVGEM-HA winds and tides have been shown to be in good agreement with ground-based meteor radar observations (McCormack et al., 2017; Eckermann et al., 2018; Laskar et al., 2019; Stober et al., 2020) and with independent satellite-based wind observations as reported in Dhadly et al. (2018). In the present study we employ NAVGEM-HA analyzed winds at 82.5 km altitude, staying below altitudes where effects of increased numerical diffusion imposed at the NAVGEM-HA upper boundary may impact the tides, to validate the method of extracting migrating tidal signatures from the SD meteor wind data.

3 Results

3.1 Sixteen-year time series

Figures 2 and 3 show the amplitudes and phases of the DW1, SW2, and TW3 tides retrieved from SD zonal and meridional meteor winds between the years 2000 and 2016. Here the phases are shown as the local time of maximum (LTOM), and phases for tidal amplitudes less than $1.5\,\mathrm{m\,s^{-1}}$ are not shown for sake of clarity.

SW2 shows a strongly repeatable seasonal cycle, where amplitudes peak around early fall (September–October) and mid-winter (December–January) and where sharp phase jumps occur around spring and fall equinox. The early fall amplitude maximum of SW2 typically reaches values between 19 and $25\,\mathrm{m\,s^{-1}}$. In contrast, the mid-winter amplitude maximum typically lies between 10 and $14\,\mathrm{m\,s^{-1}}$. SW2 consistently reaches amplitude minima coincident with the equinoctial phase jumps. While the amplitude and phase progression between the zonal and meridional components are nearly identical, meridional amplitudes can at times be 4–$5\,\mathrm{m\,s^{-1}}$ larger, especially during mid-summer (June–July). In terms of its absolute phase separation, the meridional component of SW2 is found to lead the zonal component by 2.48 h on average, giving it a 32 min offset relative to a perfect circular polarization.

TW3 also shows a strongly repeatable seasonal cycle, where a broad amplitude maximum is centered on the winter half-year (October–March) and where the phase begins to shift to a later time starting October, stabilizes around the turn of the year, and then shifts back to its pre-winter value up to March. Wintertime amplitudes typically reach values between 4 and $6\,\mathrm{m\,s^{-1}}$, whereas the tide is nearly nonexistent throughout summer. At times the amplitude of TW3 can surpass those of SW2 and DW1, in particular around fall equinox, when SW2 reaches a minimum. In addition, a pronounced secondary TW3 amplitude peak is found near day of year (DOY) 265, which can be more clearly seen in the climatology presented in the next section. This peak is most pronounced in the zonal wind, where it can reach amplitudes in the range of 4–$7\,\mathrm{m\,s^{-1}}$. In terms of its phase, TW3 is found to be nearly circularly polarized during times when the wave has an appreciable amplitude, with the meridional component leading the zonal component by 1.98 h on average.

DW1 shows considerably more short-term and interannual variability in its amplitude, phase, and between the zonal and meridional components. This is reflected in the correlation coefficient of $r = -0.23$ between the time series of hourly zonal and meridional amplitudes of DW1, whereas for SW2 and TW3 this is $r = 0.90$ and $r = 0.66$, respectively. There is, however, a clear seasonal cycle present in both the amplitude and phase of DW1, which can be more clearly seen in the climatology presented in the next section.

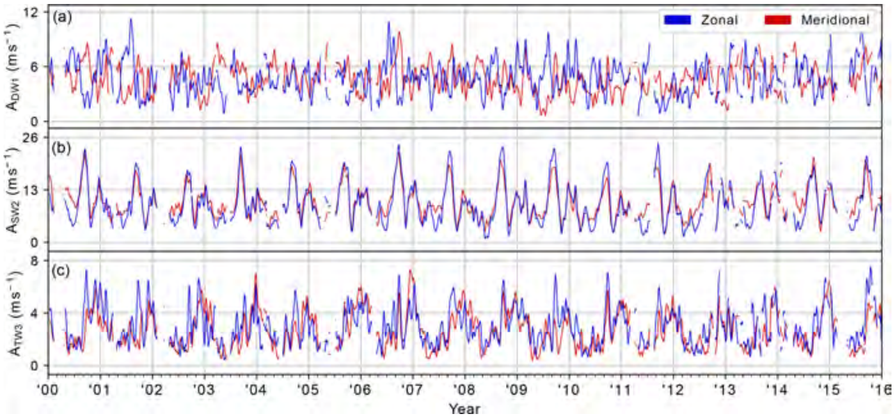

Figure 2. Amplitude of DW1 **(a)**, SW2 **(b)**, and TW3 **(c)** in SuperDARN zonal (red) and meridional (blue) meteor winds between the years 2000 and 2016.

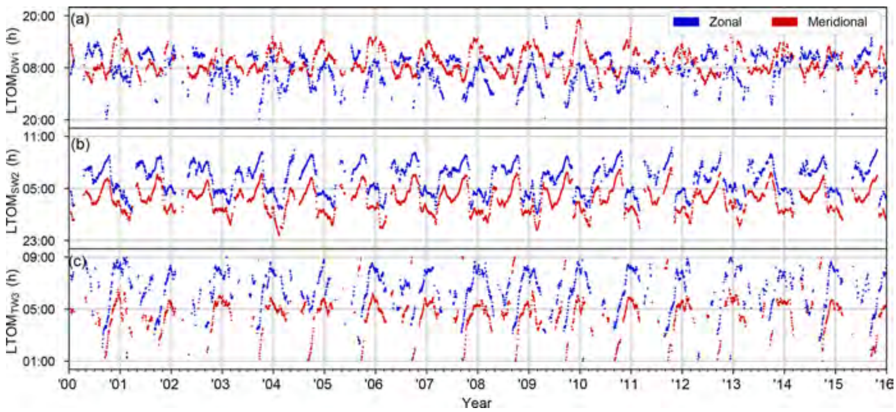

Figure 3. Phase of DW1 **(a)**, SW2 **(b)**, and TW3 **(c)** in SuperDARN zonal (red) and meridional (blue) meteor winds between the years 2000 and 2016. Phases are plotted as the local time of maximum (LTOM). Only phases for when tidal amplitudes are greater than 1.5 m s^{-1} are shown for clarity.

3.2 Climatologies

Figure 4 shows the yearly amplitude and phase climatologies of DW1, SW2, and TW3 based on the amplitudes and phases presented in the previous section. The climatologies are constructed by calculating the mean amplitude and phase for each DOY, where the mean phase is calculated using the circular mean (Fisher, 1995). The shaded area represents the standard deviation around the climatological mean amplitude and serves as a measure of year-to-year variability.

For the zonal (meridional) component, the climatological amplitude of SW2 in early fall and mid-winter peaks at 20.7 (18.8) m s^{-1} and 12.4 (12.4) m s^{-1}, respectively. Variability around the climatological mean of SW2 is largely constant throughout the year, with an average standard deviation of 2.2 (2.0) m s^{-1}. For TW3, wintertime zonal (meridional) amplitudes peak at 4.4 (5.1) m s^{-1}, while the DOY 265 amplitude peaks at 5.3 (4.1) m s^{-1}. The average standard deviation of the amplitude of TW3 is 1.0 (0.9) m s^{-1}, while variability around the climatological mean is highest coincident with the amplitude peak at DOY 265 by 1.7 (1.4) m s^{-1}.

The climatology of DW1 stands out in that amplitudes in the meridional wind broadly tend to maximize around 6.7 m s^{-1} near the equinoxes, whereas those in the zonal wind maximize around 6.7 m s^{-1} near the solstices. In addition, the climatological phase shows a circular polarization where the zonal component leads the meridional by approximately 6 h during the winter half-year but lags it by approximately 6 h during the summer half-year. The climatological phase thus shows a bi-modal circular polarization, with the polarization flipping sign broadly between summer and winter. Variability around the climatological amplitude of the zonal (meridional) component of DW1 stays largely constant throughout the year, with an average standard deviation of 1.6 (1.3) $\mathrm{m\,s^{-1}}$.

4 Validation

In this section sampling experiments with NAVGEM-HA are used to validate the method to extract migrating tides from the longitudinal chain of SD meteor wind measurements. The sampling experiments seek to address the geographical spread of the SD stations as well as the spatial sampling variations due to the changing availability of the individual stations with time (as shown in Fig. 1). Cross-contamination errors arising from the geographical spread of the SD stations are expected to be large relative to the error propagating from any individual measurement uncertainties, since each tidal fit includes at least 960 hourly data points, as discussed in Sect. 2.2.

4.1 Geographical spread

To address the geographical spread of the SD stations, migrating tides (Eq. 1) are fitted to NAVGEM-HA meridional winds sampled at the locations of available SD measurements (NAVGEM-SD), after quality checking and optimizing the longitudinal spread as discussed in Sect. 2.2. These are then compared against those fitted to a full longitude circle of data taken along 60° N (NAVGEM-360). Fits along a full longitude circle are orthogonal to any other longitudinal waves and so form a benchmark of the "true" migrating tides. As with the fits to SD, a 10 d time window is used where the window is now stepped forward in three hourly steps to accommodate the temporal resolution of NAVGEM-HA.

Figure 5 shows the migrating tides derived from NAVGEM-SD and NAVGEM-360 for the years 2014 and 2015, demonstrating that there is no structural deviation between the two for all three tidal components. The largest amplitude deviations remain incidental, whereas the phases are in close agreement at all times. On average, the phase difference between NAVGEM-SD and NAVGEM-360 is 5.9, 5.6 and 6.0 min for DW1, SW2, and TW3, respectively. The geographical spread of the SD radars is therefore concluded to not lead to significant cross-contamination errors between the migrating tides.

The corresponding tides measured by the array of SD radars are also shown in Fig. 5 (green curves). These are, however, not intended to serve as a detailed comparison between the modeled and observed tides. For such a comparison the top level of the NAVGEM-HA system would have to be extended past the vertical extent of the SD meteor echo distribution ($\sim$ 125 km), which is beyond the scope of the current work. Nevertheless, the SW2 and TW3 tides from SD and NAVGEM-HA at 82.5 km share similar characteristics in their seasonal amplitude and phase cycle, supporting the use of NAVGEM-HA to validate the SD tidal analysis method. A possible reason for the difference between the modeled and observed DW1 tide is discussed in Sect. 5.

4.2 Root-mean-square error analysis

To examine the quality of the tides fitted to NAVGEM-SD, they are compared to those fitted to NAVGEM-360 by looking at the root-mean-square error (RMSE) between their respective tidal fields. Here the tidal fields themselves can be fully reconstructed on a 360° longitude–time grid using the three hourly fitted amplitudes and phases. To account for the changing availability of the SD stations with time, the RMSE is reported using 2014 NAVGEM-HA meridional winds sampled at the locations of active SD stations for each year between 2000 and 2016. The resulting year-by-year RMSE values, calculated between the yearly reconstructed tidal fields of NAVGEM-SD and NAVGEM-360, are shown in Fig. 6. For each year the RMSE is comparatively low relative to the absolute tidal amplitudes shown in Fig. 5, ensuring the validity of the method to extract the migrating tides over the range of hourly SD data used in this study. It also shows that the stations changing with time do not induce any substantial long-term trends.

In the above, sampling NAVGEM-360 at 60° N is motivated by NAVGEM-SD most closely corresponding to NAVGEM-360 at this latitude, which is now demonstrated. To that end, the RMSE is examined between NAVGEM-SD and NAVGEM-360, where the latter is taken at each latitude between 52 and 68° N. Figure 7 demonstrates that the RMSE for the SW2 and TW3 tidal fields reaches a clear minimum at 60° N, while the RMSE of DW1 decreases also for latitudes greater than 60° N. However, the relative difference between the RMSE of DW1 at 60 and 68° N is comparatively low (-2.4 %). The migrating tides extracted from NAVGEM-SD are therefore concluded to most closely correspond to those at 60° N. Following this conclusion, the migrating tides extracted from SD are taken to be most closely representative of those at 60° N.

5 Discussion

The SW2 and TW3 tides isolated from 16 years of SD meteor winds show a well-defined and strongly recurring seasonal cycle. The main features of SW2, namely its amplitude peaks around early fall and mid-winter and sharp phase jumps around the equinoxes, are in qualitative agreement with previous observational and model studies of the mid- and high-latitude migrating semidiurnal tide (Wu et al., 2011; Xu et al., 2011; Forbes and Vial, 1989). The SW2 presented in this work indicates that the early fall amplitude peaks in the zonal and meridional winds are significantly higher than

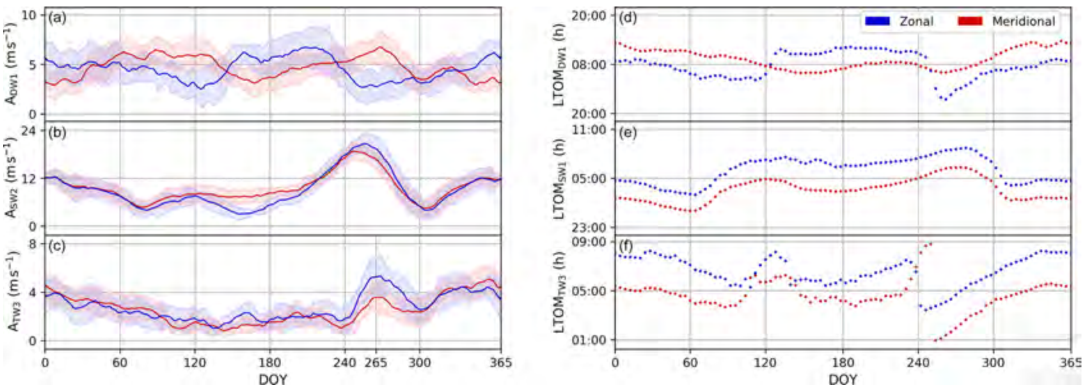

Figure 4. Climatologies of the amplitude **(a–c)** and phase **(d–f)** of the DW1 **(a)**, SW2 **(b)**, and TW3 **(c)** based on SuperDARN meridional (red) and zonal (blue) meteor winds between the years 2000 and 2016. Shading marks the standard deviation around the climatological mean. The amplitude of TW3 on DOY 265, referenced extensively in the text, is indicated in **(c)**.

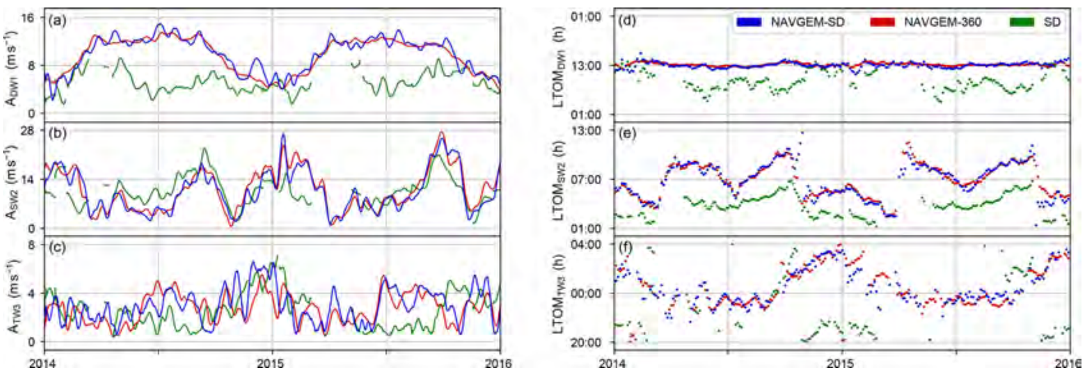

Figure 5. Amplitude and phase of DW1 **(a, d)**, SW2 **(b, e)**, and TW3 **(c, f)** in NAVGEM-SD (blue) and NAVGEM-360 (red) meridional winds at 82.5 km altitude for the years 2014 and 2015. Phases are plotted as LTOM. Green curves show the corresponding meridional tides from around 95 km altitude as measured by the array of SuperDARN (SD) radars.

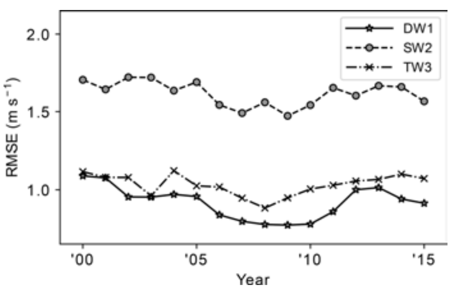

Figure 6. Yearly RMSE between the tidal fields constructed from fits to NAVGEM-360 and NAVGEM-SD sampled at active SuperDARN stations for each year between 2000 and 2016.

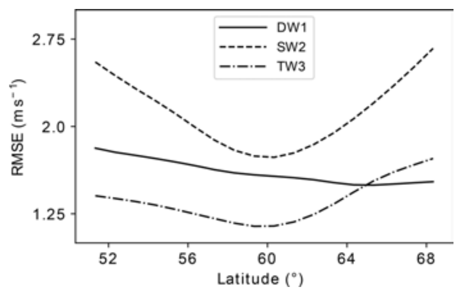

Figure 7. Yearly RMSE between the tidal fields constructed from fits to 2014 NAVGEM-SD and NAVGEM-360 taken along each latitude between 52 and 68° N.

those in mid-winter, by 71 % and 56 % on average, respectively.

The seasonal cycle of TW3, showing a broad wintertime amplitude maximum and a near 4 h LTOM phase progression tracing a half-circle throughout winter, is also in qualitative agreement with previous (satellite) observational and model studies of the mid- and high-latitude migrating terdiurnal tide (Smith, 2000; Akmaev, 2001; Smith and Ortland, 2001). The pronounced amplitude peak around DOY 265 observed by SD uniquely stands out, however, possibly owing to the high temporal resolution offered by the radars. The DOY 265 amplitude peak appears to be an enhancement superimposed on the broad wintertime maximum. There are a number of mechanisms that can excite a time-localized forcing of TW3, such as non-linear wave–wave interactions and diurnal tide and gravity wave interactions (Teitelbaum et al., 1989; Miyahara and Forbes, 1991). Whether conditions are favorable for any such mechanisms to come into effect around DOY 265 remains to be examined. Here we note that a similar time-localized amplitude peak has been described in the zonal and meridional winds above 100 km altitude at 60° N in the Canadian Middle Atmosphere Model (CMAM) (Du and Ward, 2010). Further, we note that traditional single point radar measurements of the 8 h wave are prone to contamination by gravity waves, for which 8 h falls in the middle of the typical mid- to high-latitude spectrum at MLT heights (e.g., Conte et al., 2018). Gravity wave contamination is expected to be comparatively low for the TW3 tide retrieved from SD, however, since the horizontal scale of gravity waves is much smaller than the longitudinal extent covered by the radars.

The DW1 tide shows considerably more short-term and interannual variability and a different seasonal behavior between the zonal and meridional components. A possible cause of this is that DW1 has a relatively short vertical wavelength. Whereas the semidiurnal and terdiurnal tides have a vertical wavelength on the order of 100 km in the MLT (Chapman and Lindzen, 2012; Yuan et al., 2008; Smith, 2000), the diurnal tide has a vertical wavelength on the order of 25–35 km (e.g., Avery et al., 1989). The vertical wavelength of DW1 is therefore much nearer to the vertical average represented by the SD meteor winds, which can cause DW1 to partly cancel out over the meteor echo range. Nevertheless, the climatology of the meridional component of DW1 shows close agreement with the seasonal cycle of the diurnal (1,1) Hough mode calculated from TIMED Doppler Interferometer (TIDI) and NAVGEM-HA meridional winds by Dhadly et al. (2018). It is possible that certain diurnal modes are selectively filtered by SD based on their respective vertical wavelength and that the (1,1) mode is the dominant remaining mode, even though the amplitude of this mode broadly peaks around 25° N (Chapman and Lindzen, 2012). Future work could focus on investigating whether the climatology of the zonal component of DW1 in SD can also be associated with the diurnal (1,1) Hough mode.

6 Conclusions

This study has leveraged the longitudinal coverage of 10 high-latitude SuperDARN (SD) radars to isolate the DW1, SW2, and TW3 tides from 16 years of hourly meteor wind measurements of the mid- to high-latitude MLT. Based on sampling experiments with NAVGEM-HA, it is demonstrated that the SD tides are closely representative of the (global) migrating tides along 60° N. The amplitude and phase structure of SW2 and TW3 show a strongly recurring seasonal cycle, whereas DW1 shows considerably more year-to-year variability. Notable observations are that the climatological early fall amplitude maximum of SW2 in the zonal (meridional) wind is 8.3 (6.4) $\mathrm{m\,s^{-1}}$ greater than the mid-winter maximum and that TW3 is marked by a secondary amplitude peak around DOY 265 that reaches values of $5.3 \pm 1.7\,\mathrm{m\,s^{-1}}$ in the zonal wind. In addition, DW1 is found to show a bi-modal circular phase polarization relation, where the zonal component leads the meridional during most of the year and vice versa during summer.

Many open questions remain in terms of how tidal variability is coupled to variability in their forcing mechanisms and propagation conditions. For future work, the time series of validated SD tidal measurements presented in this work can serve as a valuable source of data in studying the long- and short-term trends and variability of the migrating tides in the high-latitude MLT. The method and validation steps outlined in this work will also contribute to similar analyses of SD meteor winds from the continuously expanding global network of radars.

Data availability. SuperDARN data are available from Virginia Tech at http://vt.superdarn.org/tiki-index.php, last access: 7 December 2020.

Author contributions. WEC, PJE and REH developed the concept, while WEC performed the data analysis and wrote the paper. JPM provided NAVGEM-HA data and contributed to Sect. 2.3. PJE, REH and JPM gave feedback on the development of this work.

Competing interests. The authors declare that they have no conflict of interest.

Acknowledgements. The authors acknowledge the use of the SuperDARN meteor wind data product. The SuperDARN project is funded by national scientific funding agencies of Australia, China, Canada, France, Japan, Italy, Norway, South Africa, the United Kingdom, and the United States. Development of NAVGEM-HA was supported by the Chief of Naval Research and the Department of Defense High Performance Computing Modernization Project. The authors thank two anonymous reviewers for their assistance in improving this work.

Financial support. This research has been supported by the Research Council of Norway (grant no. 223525/F50).

Review statement. This paper was edited by Dalia Buresova and reviewed by two anonymous referees.

References

Akmaev, R. A.: Seasonal variations of the terdiurnal tide in the mesosphere and lower thermosphere: A model study, Geophys. Res. Lett., 28, 3817–3820, https://doi.org/10.1029/2001gl013002, 2001.

Arnold, N. F., Cook, P. A., Robinson, T. R., Lester, M., Chapman, P. J., and Mitchell, N.: Comparison of D-region Doppler drift winds measured by the SuperDARN Finland HF radar over an annual cycle using the Kiruna VHF meteor radar, Ann. Geophys., 21, 2073–2082, https://doi.org/10.5194/angeo-21-2073-2003, 2003.

Avery, S., Vincent, R., Phillips, A., Manson, A., and Fraser, G.: High-latitude tidal behavior in the mesosphere and lower thermosphere, J. Atmos. Sol.-Terr. Phy., 51, 595–608, https://doi.org/10.1016/0021-9169(89)90057-3, 1989.

Chapman, S. and Lindzen, R. S.: Atmospheric tides: thermal and gravitational, Springer Science & Business Media, 179 pp., 2012.

Chisham, G.: Calibrating SuperDARN Interferometers Using Meteor Backscatter, Radio Sci., 53, 761–774, https://doi.org/10.1029/2017rs006492, 2018.

Chisham, G. and Freeman, M. P.: A reassessment of SuperDARN meteor echoes from the upper mesosphere and lower thermosphere, J. Atmos. Sol.-Terr. Phy., 102, 207–221, https://doi.org/10.1016/j.jastp.2013.05.018, 2013.

Conte, J. F., Chau, J. L., Laskar, F. I., Stober, G., Schmidt, H., and Brown, P.: Semidiurnal solar tide differences between fall and spring transition times in the Northern Hemisphere, Ann. Geophys., 36, 999–1008, https://doi.org/10.5194/angeo-36-999-2018, 2018.

Dhadly, M. S., Emmert, J. T., Drob, D. P., McCormack, J. P., and Niciejewski, R. J.: Short-Term and Interannual Variations of Migrating Diurnal and Semidiurnal Tides in the Mesosphere and Lower Thermosphere, J. Geophys. Res., 123, 7106–7123, https://doi.org/10.1029/2018ja025748, 2018.

Du, J. and Ward, W. E.: Terdiurnal tide in the extended Canadian Middle Atmospheric Model (CMAM), J. Geophys. Res.-Atmos., 115, D24106, https://doi.org/10.1029/2010jd014479, 2010.

Eckermann, S. D., Ma, J., Hoppel, K. W., Kuhl, D. D., Allen, D. R., Doyle, J. A., Viner, K. C., Ruston, B. C., Baker, N. L., Swadley, S. D., Whitcomb, T. R., Reynolds, C. A., Xu, L., Kaifler, N., Kaifler, B., Reid, I. M., Murphy, D. J., and Love, P. T.: High-Altitude (0-100 km) Global Atmospheric Reanalysis System: Description and Application to the 2014 Austral Winter of the Deep Propagating Gravity Wave Experiment (DEEPWAVE), Mon. Weather Rev., 146, 2639–2666, https://doi.org/10.1175/mwr-d-17-0386.1, 2018.

Fisher, N. I.: Statistical analysis of circular data, cambridge university press, 257 pp., 1995.

Forbes, J. and Vial, F.: Monthly simulations of the solar semidiurnal tide in the mesosphere and lower thermosphere, J. Atmos. Sol.-Terr. Phy., 51, 649–661, https://doi.org/10.1016/0021-9169(89)90063-9, 1989.

Garcia, R. R., Lieberman, R., Russell, J. M., and Mlynczak, M. G.: Large-Scale Waves in the Mesosphere and Lower Thermosphere Observed by SABER, J. Atmos. Sci., 62, 4384–4399, https://doi.org/10.1175/jas3612.1, 2005.

Hall, G. E., MacDougall, J. W., Moorcroft, D. R., St.-Maurice, J.-P., Manson, A. H., and Meek, C. E.: Super Dual Auroral Radar Network observations of meteor echoes, J. Geophys. Res., 102, 14603–14614, https://doi.org/10.1029/97ja00517, 1997.

Hibbins, R. E. and Jarvis, M. J.: A long-term comparison of wind and tide measurements in the upper mesosphere recorded with an imaging Doppler interferometer and SuperDARN radar at Halley, Antarctica, Atmos. Chem. Phys., 8, 1367–1376, https://doi.org/10.5194/acp-8-1367-2008, 2008.

Hibbins, R. E., Espy, P. J., Orsolini, Y. J., Limpasuvan, V., and Barnes, R. J.: SuperDARN Observations of Semidiurnal Tidal Variability in the MLT and the Response to Sudden Stratospheric Warming Events, J. Geophys. Res.-Atmos., 124, 4862–4872, https://doi.org/10.1029/2018jd030157, 2019.

Laskar, F. I., McCormack, J. P., Chau, J. L., Pallamraju, D., Hoffmann, P., and Singh, R. P.: Interhemispheric Meridional Circulation During Sudden Stratospheric Warming, J. Geophys. Res., 124, 7112–7122, https://doi.org/10.1029/2018ja026424, 2019.

McCormack, J., Hoppel, K., Kuhl, D., de Wit, R., Stober, G., Espy, P., Baker, N., Brown, P., Fritts, D., Jacobi, C., Janches, D., Mitchell, N., Ruston, B., Swadley, S., Viner, K., Whitcomb, T., and Hibbins, R.: Comparison of mesospheric winds from a high-altitude meteorological analysis system and meteor radar observations during the boreal winters of 2009-2010 and 2012-2013, J. Atmos. Sol.-Terr. Phy., 154, 132–166, https://doi.org/10.1016/j.jastp.2016.12.007, 2017.

Miyahara, S. and Forbes, J. M.: Interactions between Gravity Waves and the Diurnal Tide in the Mesosphere and Lower Thermosphere, J. Meteorol. Soc. Jpn., 69, 523–531, https://doi.org/10.2151/jmsj1965.69.5_523, 1991.

Ortland, D. A.: Daily estimates of the migrating tide and zonal mean temperature in the mesosphere and lower thermosphere derived from SABER data, J. Geophys. Res.-Atmos., 122, 3754–3785, https://doi.org/10.1002/2016jd025573, 2017.

Pancheva, D. and Mukhtarov, P.: Atmospheric Tides and Planetary Waves: Recent Progress Based on SABER/TIMED Temperature Measurements (2002-2007), in: Aeronomy of the Earth's Atmosphere and Ionosphere, Springer Netherlands, 19–56, https://doi.org/10.1007/978-94-007-0326-1_2, 2011.

Reid, I. M.: MF and HF radar techniques for investigating the dynamics and structure of the 50 to 110 km height region: a review, Progress in Earth and Planetary Science, 2, 33, https://doi.org/10.1186/s40645-015-0060-7, 2015.

Sakazaki, T., Fujiwara, M., and Shiotani, M.: Representation of solar tides in the stratosphere and lower mesosphere in state-of-the-art reanalyses and in satellite observations, Atmos. Chem. Phys., 18, 1437–1456, https://doi.org/10.5194/acp-18-1437-2018, 2018.

Salby, M. L.: Sampling Theory for Asynoptic Satellite Observations, Part I: Space-Time Spectra, Resolution, and Aliasing, J. Atmos. Sci., 39, 2577–2600, https://doi.org/10.1175/1520-0469(1982)039<2577:STFASO>2.0.CO;2, 1982.

Smith, A. K.: Structure of the terdiurnal tide at 95 km, Geophys. Res. Lett., 27, 177–180, https://doi.org/10.1029/1999gl010843, 2000.

Smith, A. K.: Global Dynamics of the MLT, Surv. Geophys., 33, 1177–1230, https://doi.org/10.1007/s10712-012-9196-9, 2012.

Smith, A. K. and Ortland, D. A.: Modeling and Analysis of the Structure and Generation of the Terdiurnal Tide, J. Atmos. Sci., 58, 3116–3134, https://doi.org/10.1175/1520-0469(2001)058<3116:MAAOTS>2.0.CO;2, 2001.

Stober, G., Baumgarten, K., McCormack, J. P., Brown, P., and Czarnecki, J.: Comparative study between ground-based observations and NAVGEM-HA analysis data in the mesosphere and lower thermosphere region, Atmos. Chem. Phys., 20, 11979–12010, https://doi.org/10.5194/acp-20-11979-2020, 2020.

Teitelbaum, H., Vial, F., Manson, A., Giraldez, R., and Massebeuf, M.: Non-linear interaction between the diurnal and semidiurnal tides: terdiurnal and diurnal secondary waves, J. Atmos. Terr. Phy., 51, 627–634, https://doi.org/10.1016/0021-9169(89)90061-5, 1989.

Wu, Q., Ortland, D., Solomon, S., Skinner, W., and Niciejewski, R.: Global distribution, seasonal, and inter-annual variations of mesospheric semidiurnal tide observed by TIMED TIDI, J. Atmos. Sol.-Terr. Phy., 73, 2482–2502, https://doi.org/10.1016/j.jastp.2011.08.007, 2011.

Xu, X., Manson, A. H., Meek, C. E., Jacobi, C., Hall, C. M., and Drummond, J. R.: Mesospheric wind semidiurnal tides within the Canadian Middle Atmosphere Model Data Assimilation System, J. Geophys. Res., 116, D17102, https://doi.org/10.1029/2011jd015966, 2011.

Yuan, T., Schmidt, H., She, C. Y., Krueger, D. A., and Reising, S.: Seasonal variations of semidiurnal tidal perturbations in mesopause region temperature and zonal and meridional winds above Fort Collins, Colorado (40.6° N, 105.1° W), J. Geophys. Res., 113, D20103, https://doi.org/10.1029/2007jd009687, 2008.

Paper II

van Caspel, W. E., Espy, P. J., Ortland, D. A., & Hibbins, R. E. (2022). The mid- to high-latitude migrating semidiurnal tide: Results from a mechanistic tide model and SuperDARN observations. *Journal of Geophysical Research: Atmospheres*, 127, e2021JD036007. https://doi.org/10.1029/2021JD036007

AGU ADVANCING EARTH AND SPACE SCIENCE

JGR Atmospheres

RESEARCH ARTICLE
10.1029/2021JD036007

Key Points:

- Simulations of the migrating semidiurnal (SW2) tide are validated against observations from a high-latitude array of Super Dual Auroral Radar Network meteor radars
- Numerical experiments investigate the impact of the background atmosphere, tidal dissipation, and tidal forcing on the simulation results
- The simulated SW2 is largely shaped by the background atmosphere, while being sensitive to eddy diffusion and surface friction

Correspondence to:
W. E. van Caspel,
willem.e.v.caspel@ntnu.no

Citation:
van Caspel, W. E., Espy, P. J., Ortland, D. A., & Hibbins, R. E. (2022). The mid- to high-latitude migrating semidiurnal tide: Results from a mechanistic tide model and SuperDARN observations. *Journal of Geophysical Research: Atmospheres*, *127*, e2021JD036007. https://doi.org/10.1029/2021JD036007

Received 8 OCT 2021
Accepted 30 DEC 2021

The Mid- to High-Latitude Migrating Semidiurnal Tide: Results From a Mechanistic Tide Model and SuperDARN Observations

Willem E. van Caspel[1,2], Patrick J. Espy[1,2], David A. Ortland[3], and Robert E. Hibbins[1,2]

[1]Department of Physics, Norwegian University of Science and Technology (NTNU), Trondheim, Norway, [2]Birkeland Centre for Space Science, Bergen, Norway, [3]Northwest Research Associates, Inc., Redmond, WA, USA

Abstract Simulations of the solar thermal migrating semidiurnal (SW2) tide in the mesosphere-lower-thermosphere (MLT) are compared against meteor wind observations from a longitudinal chain of high-latitude Super Dual Auroral Radar Network radars. The simulations span the year 2015 and are performed using a mechanistic primitive equation model. The model employs a whole-atmosphere tide forcing based on temperature tendency fields from the Specified Dynamics Whole Atmosphere Community Climate Model with Thermosphere and Ionosphere Extension, and a background atmospheric specification based on zonal wind and temperature data from the Navy Global Environmental Model-High Altitude meteorological analysis system. Results show that the model accurately reproduces the observed seasonal variability of the SW2 tide in both the amplitude and phase. Numerical experiments are performed to investigate how the tidal forcing, dissipation terms, and seasonal variations in the background atmosphere shape the seasonal variations of the simulated SW2 tide. Notable results are that the background atmosphere most strongly impacts the SW2 tide forced in the troposphere, and that the specification of a narrow surface friction profile enhances the net SW2 amplitude in the MLT between April and October. Eddy diffusion is found to damp the simulated tide predominantly around summer solstice and in December.

1. Introduction

Atmospheric tides are global-scale waves whose periods are an integer fraction of a solar day (Chapman & Lindzen, 1970). The tides are forced primarily by radiative and latent heating effects in the lower atmosphere (Hagan, 1996), but obtain their largest amplitudes in the mesosphere-lower-thermosphere (MLT) region (80–120 km altitude). There they are expressed as pronounced oscillations in a broad range of atmospheric fields, such as density, pressure, and wind. The migrating tides are those tides which follow the apparent motion of the sun, having a longitudinal zonal wavenumber (S) and latitudinal spherical harmonic (Hough mode) structure. In the current work, the focus lies on the migrating semidiurnal (SW2; for Semidiurnal, Westward $S = 2$) tide. The SW2 tidal winds maximize in the mid- and high-latitude MLT (Manson et al., 2002; Wu et al., 2011), where they form a major source of day-to-day and inter-seasonal variability of the MLT-ionosphere system (Arras et al., 2009; G. Shepherd et al., 1998; Smith, 2012). The SW2 tide is recognized as an important vertical coupling mechanism (Forbes, 2009; Pedatella & Forbes, 2010), and as a contributing factor to the vertical mixing and energy budget of the upper atmosphere (Becker, 2017; Forbes et al., 1993).

The numerical study of the SW2 tide has a long history (e.g., Forbes & Garrett, 1979). Nevertheless, open questions remain about the mechanisms governing the tide's seasonal and short-term variability (Conte et al., 2018; G. Liu et al., 2021; Pedatella et al., 2020; Zhang et al., 2021). Many recent studies are in part driven by the increasing availability of high-altitude and tide-resolving general circulation models. A challenging aspect of using such models is that the representation of the SW2 tide can vary significantly from model to model (McCormack et al., 2021; Pancheva et al., 2020; Stober et al., 2021), while the cause of these differences is often obscured by the complexity of the models.

In the current work, a development of the mechanistic tide model from Ortland (2017) is used to simulate the SW2 tide observed in the MLT by a longitudinal array of Super Dual Auroral Radar Network (SuperDARN) meteor radars. The purpose of the simulations is to mechanistically identify which processes contribute to the seasonal variations of the SW2 tide in the mid- to high-latitude MLT. To this end, the model employs a realistic background atmosphere based on zonal mean zonal winds and temperatures from the Navy Global Environmental

Model-High Altitude (NAVGEM-HA), and a whole-atmosphere tidal forcing based on heating rates from the Specified Dynamics Whole Atmosphere Community Climate Model with Thermosphere Extension (SD-WACCMX). Dissipative processes are parameterized between the surface and thermosphere, which includes a specification of ion drag, Newtonian cooling, surface friction, and a seasonally dependent eddy diffusion.

Section 2 discusses the model and data used in this work. This includes a description of the model configuration, its dissipation terms, tidal forcing scheme, background atmospheric specification, and output analysis. In Section 3, the simulated SW2 tidal amplitude and phase are validated against observation for the year 2015, with reference to climatological observations. Section 4 describes a series of numerical experiments investigating how the background atmosphere, tidal forcing, and dissipation terms shape the seasonal variations of the simulated SW2 tide. In Section 5, the impact of the background atmosphere is investigated in more detail, where a distinction is made between the SW2 tide forced in the troposphere, stratosphere, and mesosphere-thermosphere (MT) regions. A discussion of the results is given in Section 6.

2. Data and Model Description

2.1. Primitive Equation Model

The model is a development of the primitive equations in sigma-coordinates model (PRISM) described in detail in Ortland (2017) and references therein. Earlier works have used the model to study tide-gravity wave interactions (Ortland & Alexander, 2006), tropical waves (Ortland & Alexander, 2014; Ortland et al., 2011), planetary waves (Lieberman et al., 2021), and tide-planetary wave interactions (Lieberman et al., 2015). PRISM is a three-dimensional nonlinear and time-dependent spectral model, which numerically integrates the vorticity and divergence form of the primitive equations. For a comprehensive discussion of the primitive equations, the reader is referred to Holton (2003).

In the current work, PRISM is configured to have 121 vertical levels between the surface and 7.5×10^{-6} Pa (~430 km altitude), with a vertical grid spacing of approximately 0.1 km in the troposphere and 2.0 km in the MLT. A realistic surface topography is included by incorporating the surface geopotential field from the European Centre for Medium-Range Weather Forecasts (ECMWF) ERA5 reanalysis model (Hersbach et al., 2020). The horizontal resolution of PRISM is truncated at zonal wavenumber $S = 3$ and associated Legendre polynomial of degree $N = 23$, while a step size of $\Delta t = 0.3$ hr is used in the semi-implicit time-integration scheme. Higher order horizontal, vertical, or temporal resolutions were found to have very little impact on the simulated SW2 tide. No parameterization of gravity waves is included in the current work.

2.2. Dissipation

The model employs a number of one-dimensional vertical dissipation profiles, which act to damp the vorticity (ξ), divergence (D), and temperature (Θ) fields. Damping is achieved by subtracting the model state at time-step $n-1$ to the tendency equation at time-step n at each of the model levels l, as

$$\frac{\partial \chi_l^n}{\partial t} = \cdots - \nu_l \chi_l^{n-1}; \quad \chi_l = \xi_l, D_l, \Theta_l, \tag{1}$$

where ν_l represents the dissipation coefficients in units of s^{-1}, and where the three dots represent the model tendency equation without damping. Figure 1 gives an overview of the dissipation terms used in this study, where the coefficients have been scaled to units of days^{-1} (d^{-1}).

A parameterization of ion drag, represented by a Rayleigh friction acting on the vorticity and divergence fields, is included to crudely represent the exchange of momentum between neutral molecules and ions moving under the influence of Earth's magnetic field. The coefficients of ion drag (ν_i) follow those calculated by Hong and Lindzen (1976) for solar maximum conditions, using the expression $\nu_i(z) = 10^{-4} \times \tanh\left[(z-110)/30\right]$ s^{-1} with z in units of kilometer. Damping due to radiative cooling by CO_2 and O_3 in the troposphere and stratosphere is parameterized as a Newtonian cooling. The Newtonian cooling profile broadly follows those from Hagan et al. (1993) and Wood and Andrews (1997), and reduces to a value of zero above 70 km altitude.

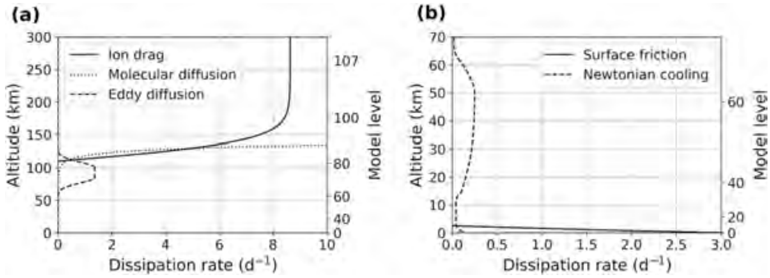

Figure 1. Vertical profiles of the coefficients of ion drag, molecular diffusion, and peak eddy diffusion (a), and the vertical profiles of the surface friction and Newtonian cooling coefficients (b).

Following Vial (1986) (hereafter V86) and others (e.g., Forbes & Vincent, 1989; Wood & Andrews, 1997), vertical eddy diffusion of momentum is parameterized as an effective Rayleigh friction. For a wave with vertical wavenumber k_z this approximation is written as

$$\upsilon_{\text{eff,t}} = K_t k_z^2, \tag{2}$$

where K_t (m^2 s^{-1}) represents eddy diffusion and $v_{\text{eff,t}}$ is the corresponding effective Rayleigh friction coefficient. Following V86, a value of $k_z = 2\pi/25$ km^{-1} is adopted for the simulation of the semidiurnal tide. This wavelength is characteristic of the semidiurnal (2, 5) Hough mode, which is the lowest order Hough mode which is expected to be affected by dissipation at meteor echo altitudes. Lower order Hough modes are typically only weakly affected by dissipation, owing to their longer vertical wavelengths (Forbes & Garrett, 1979).

The notation of V86 is adopted for a vertical profile of eddy diffusion, which is written as

$$K_t(z) = \begin{cases} K_0 \exp\left[-((z-z_1)/a_1)^2\right], & z \le z_1 \\ K_0, & z_1 \le z \le z_2 \\ K_0 \exp\left[-((z-z_2)/a_2)^2\right], & z \ge z_2, \end{cases} \tag{3}$$

where z is in units of kilometer. While V86 considers values in the range of z_1 = 91.7–96.6 km, z_2 = 100.1–102.9 km, a_1 = 7.7–8.4 km, and a_2 = 7.8 km, the current work adopts the values of z_1 = 85 km, z_2 = 100 km and $a_1 = a_2$ = 12 km. These values yield a vertical profile that is representative of a seasonal mid- and high-latitude average based on the Garcia and Solomon (1985) model, whose vertical and latitudinal variations are illustrated in more detail in Hagan et al. (1995). The mid- and high-latitude vertical profile of the Garcia and Solomon (1985) model is generally broader than that of V86, reaching its highest dissipation rates between 70 and 110 km altitude depending on season.

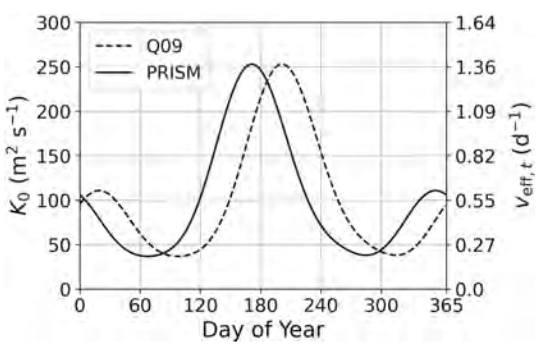

Figure 2. Seasonal variations of the eddy diffusion coefficient at ~97 km altitude applied at the lower boundary of the Thermosphere-Ionosphere-Electrodynamics General Circulation Model by Q09 (dashed line), and the 30-day shifted profile used by PRISM (solid line). The right-hand axis shows the effective Rayleigh friction coefficient calculated using Equation 2.

The K_0-term in Equation 3 controls the magnitude of the eddy diffusion profile, and for this the eddy diffusion coefficient specified at the lower boundary (~97 km altitude) of the Thermosphere-Ionosphere-Electrodynamics General Circulation Model by Qian et al. (2009) (hereafter Q09) is used. A key feature of the K_0 from Q09 is that it follows the seasonal variations in global eddy diffusion, as inferred from satellite drag and O/N_2 observations. The eddy diffusion itself is attributed to seasonal variations in the mixing caused by dissipating gravity waves. In the current work, however, the seasonal variations of Q09 are shifted forward in time by 30 days. The effect of this shift is to bring the seasonal variations nearer to that of the mid- to high-latitude variations of the Garcia and Solomon (1985) model, whose temporal variations are illustrated in more detail in Pilinski and Crowley (2015). The shifted profile is illustrated in Figure 2 along with the Q09 profile, in addition to the

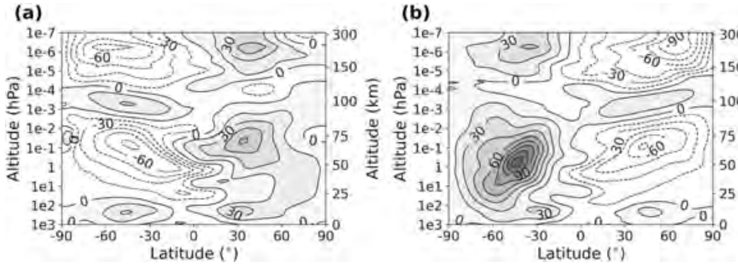

Figure 3. NAVHWER zonal mean zonal winds for January (a) and July (b) 2015 conditions. Contours show eastward (solid) and westward (dashed) winds spaced in 15 ms^{-1} intervals.

corresponding effective Rayleigh friction values calculated using Equation 2. The impact of eddy diffusion and of the 30-day shift are discussed in more detail in Section 4.

Following V86, molecular diffusion of momentum is parameterized as an effective Rayleigh friction using $\upsilon_{\mathrm{eff,m}}(z) = 5.28 \times 10^{-13}\exp\left[-z/7\right]\ \mathrm{s}^{-1}$, where z is in units of kilometer. In addition, following V86 a Prandtl number of 1 is assumed, which implies that the Rayleigh friction terms representing eddy and molecular diffusion of momentum are equally applied as Newtonian cooling terms for the eddy and molecular diffusion of heat.

Momentum sinks arising from turbulent surface fluxes and unresolved topography have often been parameterized as a Rayleigh friction term in coarse resolution general circulation models (e.g., McLandress, 2002; T. G. Shepherd et al., 1996; Stevens et al., 2002). In the current work, the surface Rayleigh friction profile from Chen et al. (2007) is adopted. This profile has a surface value of A_0 and decreases linearly in sigma-coordinates between $\sigma = 1$ and $\sigma = 0.7$ (~3 km altitude). While Chen et al. (2007) consider values of A_0 in the range of 0.6–4.0 d^{-1}, a value of $A_0 = 3.0\ \mathrm{d}^{-1}$ is employed in the current work. The model sensitivity to surface friction, as well as the choice of A_0, is discussed in more detail in Section 4.

The 10 highest model levels (~300–430 km altitude) act as a "sponge layer" to prevent spurious model top wave-reflections. For this, an altitude-dependent damping rate of $\alpha_s\left(1 + \tanh\left[(z - 250)/40\right]\right)$ is applied to all dynamical fields, where $\alpha_s = 25\ \mathrm{d}^{-1}$ and z is in units of kilometer.

2.3. Background Atmosphere

The mean zonal winds and temperatures of the background atmosphere can be freely specified in PRISM. This is achieved by relaxing the zonal mean spherical harmonic coefficients toward a zonal mean assimilation state, for which a nudging rate of $D = 1/3\ \mathrm{d}^{-1}$ is used. Since only the zonal mean spherical harmonics are involved in the nudging, the simulated tides are not affected by this.

The mean zonal winds and temperatures in the middle atmosphere (85–0.001 hPa) are nudged to daily mean zonal mean fields calculated from 3-hourly NAVGEM-HA data. NAVGEM-HA is a meteorological analysis system extending up to the lower thermosphere (~116 km), assimilating satellite observations of temperature, water vapor, and ozone in the Middle Atmosphere, as well as standard operational meteorological observations in the troposphere and stratosphere (McCormack et al., 2017). Seasonal and short-term variations in the NAVGEM-HA winds and temperatures have been shown to be in good agreement with independent satellite-based wind observations (Dhadly et al., 2018), and with ground-based meteor radar observations (Eckermann et al., 2018; Laskar et al., 2019; McCormack et al., 2017; Stober et al., 2020).

Between the surface and 85 hPa the mean zonal winds and temperatures are nudged to daily mean zonal mean fields calculated from the ERA5 reanalysis data set (Hersbach et al., 2020). Above 0.001 hPa, the assimilated fields are based on daily mean zonal mean zonal winds and temperatures from the empirical Horizontal Wind Model version 2014 (HWM14, Drob et al., 2015) and the NRLMSISE-00 reference model (Picone et al., 2002), respectively. In the following sections, the composite atmosphere between the surface and thermosphere is referred to as the NAVHWER atmosphere. The NAVHWER zonal mean zonal winds for January and July 2015 conditions are illustrated in Figure 3, up to the base of the sponge layer. Diagnostic simulations where the boundaries between

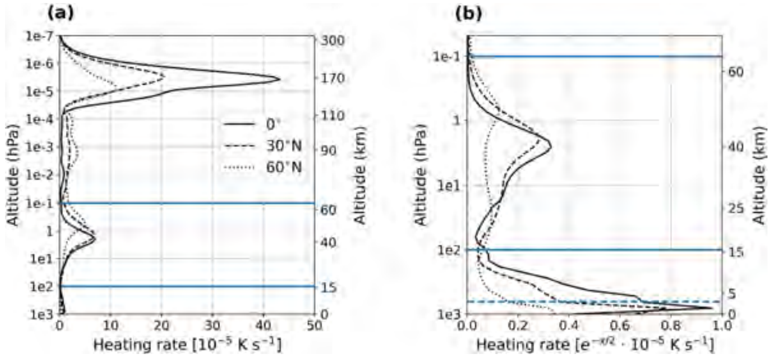

Figure 4. Vertical profiles of the migrating semidiurnal amplitude in the Specified Dynamics Whole Atmosphere Community Climate Model with Thermosphere and Ionosphere Extension temperature tendency fields for January 2015 at 0°, 30°, and 60° latitude (a). The amplitudes are scaled by a factor $\exp(-x/2)$ in panel (b), where $x = -\ln(p/p_0)$. The solid blue lines demark the boundaries of the tropospheric, stratospheric and mesosphere-thermosphere forcing regions referred to in the text. The dashed blue line indicates the upper boundary of surface friction.

the different data sets used to construct the NAVWHER atmosphere are artificially smoothed, find that any discontinuities which may be present between the data sets have a negligible impact on the simulated SW2 tide.

2.4. Tidal Forcing

The SW2 tide is forced by incorporating 3-hourly global temperature tendency fields (K s^{-1}), also referred to as heating rates, from the Specified Dynamics Whole Atmosphere Community Climate Model with Thermosphere Extension version 2.1 (SD-WACCMX, H.-L. Liu et al., 2018). SD-WACCMX is a comprehensive whole atmosphere-ionosphere numerical model extending from the surface up to 500–700 km altitude, where the winds and temperatures below ∼50 km altitude are specified to data from the Modern-Era Retrospective analysis for Research and Applications Version 2 (MERRA-2, Gelaro et al., 2017). The SD-WACCMX model includes parameterizations of the major chemical and radiative processes between the troposphere and thermosphere, including those of the ionosphere and of non-local-thermal-equilibrium processes. The version of SD-WACCMX used in this study has a horizontal latitude-longitude resolution of 1.9 by 2.5°, with a vertical resolution between 1.0 and 3.5 km. All available SD-WACCMX temperature tendency fields are incorporated in the simulations presented in this work, which include the temperature tendencies due to shortwave radiation, longwave radiation, moist processes, NO cooling, and gravity wave dissipation.

To force the tides, the SD-WACCMX temperature tendencies are first interpolated from their native vertical hybrid sigma-pressure grid to the PRISM sigma-coordinate grid. These interpolated fields are then interpolated linearly in time onto the PRISM temperature tendency equation at timestep n for each model level l (represented by), as

$$\frac{\partial \Theta_l^n}{\partial t} = \dots + \left.\frac{\partial \Theta_l^n}{\partial t}\right|_{\mathrm{SD\text{-}WACCMX}}. \tag{4}$$

As a result, the model time-integration step will then generate atmospheric heating and cooling in accordance with the prescribed SD-WACCMX temperature tendency fields. This in turn excites a broad spectrum of atmospheric buoyancy waves, including the thermal tides. While the current work focuses on the SW2 tide, the SD-WACCMX temperature tendencies in principle excite a full spectrum of migrating and non-migrating tides. Here we note that PRISM does not include any other parameterizations of diabatic processes.

Figure 4 shows the amplitude of the SW2 component of the SD-WACCMX temperature tendency fields (the "SW2 forcing") for January 2015 conditions at 0°, 30°, and 60° latitude, calculated using 2D Fourier analysis. Figure 4a shows that the peak SW2 heating rates occur in the thermosphere, with a secondary peak located in the stratosphere. The forcing is generally stronger toward the equator. In Figure 4b the forcing has been scaled by a factor $\exp(-x/2)$ following Forbes (1982), where $x = -\ln(p/p_0)$ and p_0 is the surface pressure. This scaling factor compares the relative importance of the forcing strength by altitude, by adjusting for the decreasing density of the atmosphere as it appears in the tidal equations (Chapman & Lindzen, 1970). As a result, the relative forcing strength becomes comparable between the troposphere and stratosphere regions, with that of the stratosphere peaking near 40 km and that of the troposphere peaking near the surface. In addition, the relative forcing strength is close to zero near to the tropopause (100 hPa), and converges to zero for altitudes around ∼60–65 km.

In Section 5 the distinction is made between the MLT amplitude of the SW2 tides forced in the troposphere, stratosphere, and MT regions. To that end, the solid blue lines in Figure 4 mark the altitude regions broadly encompassing the tropospheric forcing (1,000–100 hPa), the stratospheric forcing (100–0.1 hPa), and MT forcing (0.1–10^{-7} hPa). The dotted blue line in Figure 4b indicates the highest altitude where surface friction applies.

2.5. SuperDARN Observations and Model Sampling

The 10 SuperDARN radars used in this study are the same as those used in the study of van Caspel et al. (2020), and span 180° of longitude around a 14° latitude band centered on 60° North. The SuperDARN radars make time-synchronized hourly horizontal wind measurements based on the back-scatter signal of meteor ablation trails in the MLT (Hussey et al., 2000). While a detailed description and validation of the method used to extract the SW2 tide from the array of SuperDARN measurements is given in van Caspel et al. (2020), a brief description of the method is included here.

The vertical distribution of meteor echoes observed in the first four range gates of the SuperDARN radars extends between 75 and 125 km altitude and is approximately a Gaussian centered on 100 km altitude with a Full Width at Half Maximum (FHWM) between 25 and 35 km (Chisham & Freeman, 2013). The average FWHM of the first four range gates as used in this study is approximately 30 km. The SW2 tidal signal is extracted from the hourly SuperDARN winds by least squares fitting a function representing the migrating diurnal, semidiurnal, and terdiurnal tide, including a mean wind, in both space and time to data from all stations. While van Caspel et al. (2020) employed a 10-day sliding window to perform the tidal fit, a 16-day window is used in the current work. This is done to reduce the impact of any possible lunar (12.42 hr) tide contamination (Maute et al., 2016; Sandford et al., 2006), and of low-frequency planetary wave modulation (Teitelbaum & Vial, 1991). Furthermore, because of the large number of data points included in each fit, the uncertainties on the fitted tidal parameters becomes negligibly small (less than 0.5 ms^{-1} and 20 min for the tidal amplitudes and phases, respectively) when taking into account the uncertainty estimates on the hourly SuperDARN winds.

To compare the model to observation, 3-hourly instantaneous PRISM output is first interpolated to the locations of available SuperDARN measurements. The sampled data are then interpolated to a 75–125 km altitude grid with 2.5 km spacing by numerically integrating the barometric formula. A SuperDARN "observational filter" is then applied to the interpolated data, represented by a Gaussian vertical averaging kernel following the SuperDARN meteor echo distribution. For this, a Gaussian centered on 100 km altitude with a FWHM of 30 km is used. We note that, while the mean height and FWHM of the SuperDARN meteor echo distribution can exhibit seasonal variations on the order of a few km (Chisham, 2018), such variations only minimally impact the SW2 simulation results.

In the following, the sampled and vertically averaged model winds are referred to as PRISM-SDARN. The model winds are analyzed using the same method used for the hourly SuperDARN winds, but now using a 16-day sliding window that is stepped forward in 3-hourly steps, to accommodate the temporal resolution of the model output.

3. Simulation Results

Figure 5 compares the PRISM-SDARN and observed SuperDARN SW2 tidal amplitude and phase for the year 2015, with reference to the climatological amplitude and phase based on observations between the years 2000 and 2016 (van Caspel et al., 2020). The tidal phases are expressed in terms of local time of maximum (hr), which for the migrating tides is independent of longitude.

The main seasonal characteristics of the observed tide are its amplitude maxima in September and in winter, and its rapid phase transitions coincident with amplitude minima in March and late October. These features show little year-to-year variability (van Caspel et al., 2020), and are consistent with numerous other northern hemisphere

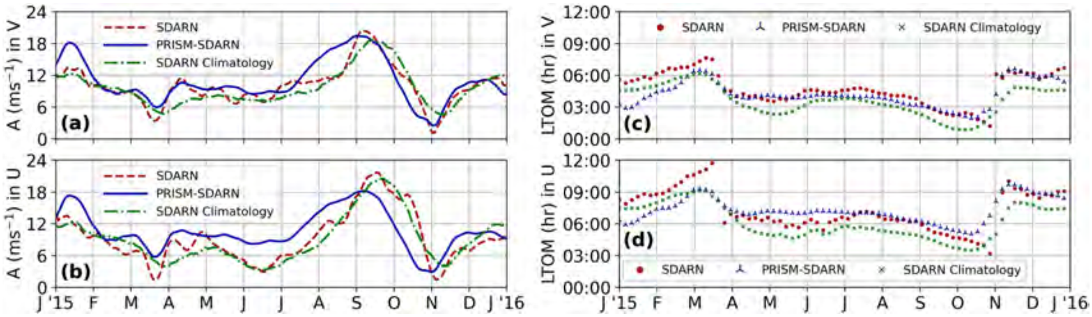

Figure 5. Simulated PRISM-SDARN (blue) and observed Super Dual Auroral Radar Network (SDARN, red) migrating semidiurnal amplitude and phase in the meridional (a, c) and zonal (b, d) wind for the year 2015, and the climatological observed amplitude and phase (green) based on observations between the years 2000 and 2016 (van Caspel et al., 2020).

observations of the mid- and high-latitude SW2 tide (e.g., He & Chau, 2019; Wu et al., 2011). Figure 5 demonstrates that the observed seasonal behavior of the SW2 amplitude and phase for the year 2015 are closely representative of the climatological seasonal variations.

The PRISM-SDARN simulation results display good year-round agreement with the observed tide, with all of the seasonal characteristics being well reproduced. For the tidal amplitudes, the largest discrepancies occur in January and between August and October. In January, the model overestimates amplitudes by up to 5 ms^{-1}, while between August-October amplitudes can differ by as much as 12 (6) ms^{-1} in the zonal (meridional) wind. The amplitude differences between August–October mostly represent variations in the temporal evolution of the September maximum. Another difference between model and observation is that the observed amplitudes are consistently smaller (greater) in the zonal wind than in the meridional in June (September; van Caspel et al., 2020), as can also be seen in Figure 5. In contrast, the modeled zonal and meridional amplitudes are nearly identical at all times.

For the tidal phases, the main discrepancy occurs between January and March. During this time, the modeled phase is approximately 2.5 hr earlier than observation. Nevertheless, the phases show excellent agreement during the rest of the year. By comparison of Figures 5d and 5c, it follows that both the simulated and observed tide display a circular phase relation, where the meridional component leads the zonal by approximately 3 hr.

The results from this section give confidence that the model adequately describes the main processes governing the seasonal variations of the SW2 tide. That is to say, that the tidal forcing scheme, background atmospheric specification, dissipation terms, and output sampling technique, are sufficiently realistic to reproduce the observed seasonal behavior of the tide. In the following section, numerical experiments are performed to investigate which aspects of the model most strongly control the simulation results.

4. Model Analysis

Numerical experiments are performed to investigate the impact of the background atmosphere, tidal forcing, eddy diffusion, and surface friction on the ability of the model to simulate the SW2 tide observed by SuperDARN. In these experiments, only the meridional component of the tide is considered, since it was established in the previous section that the modeled tide is circularly polarized but otherwise nearly identical between the zonal and meridional wind. We further note that the simulations presented in this work are insensitive to the specification of ion drag, molecular diffusion, and Newtonian cooling. A separate sensitivity study for these parameterizations is therefore not included. An overview of the numerical experiments of this section is given in Table 1.

4.1. Experiment Results

Figures 6a and 6d compare PRISM-SDARN against a simulation made using a zero-wind background atmosphere (ZeroWind). The background atmosphere of the ZeroWind experiment is constructed using a single global

Table 1
Numerical Experiment Design

Experiment	Configuration
PRISM-SDARN	Standard model configuration (see Section 2)
ZeroWind	As PRISM-SDARN, zero-wind background atmosphere
NoEdDiff	As PRISM-SDARN, no eddy diffusion
NoEdShift	As PRISM-SDARN, no 30-day shift Q09 eddy diffusion profile
SurfEnhan	As PRISM-SDARN, surface friction coefficient $A_0 = 4.5\ \mathrm{d}^{-1}$
SurfReduc	As PRISM-SDARN, surface friction coefficient $A_0 = 1.5\ \mathrm{d}^{-1}$

Note. SDARN, Super Dual Auroral Radar Network.

mean yearly mean vertical temperature profile, yielding zero zonal mean zonal winds everywhere. The amplitude and phase of the SW2 tide observed by SuperDARN are included here for reference.

In the ZeroWind simulation, the tidal phase and amplitude see little to no seasonal variation. As a result, it can be concluded that the NAVWHER atmosphere strongly impacts the simulated SW2 tide, giving rise to the seasonal phase characteristics and to the amplitude maxima in September and winter. The ZeroWind experiment also demonstrates that any seasonal variations in the tidal forcing itself only minimally impact the simulated tide.

Figures 6b and 6e compare PRISM-SDARN against simulations where the eddy diffusion has been turned off (NoEdDiff), and where the employed seasonal variations of Q09 have not been shifted forward by 30 days. The NoEdDiff experiment demonstrates that eddy diffusion primarily acts to damp the tide between March and mid-September and in December. This in turn contributes to the rapid amplitude increase toward the September maximum, which in the model falls broadly between August and September. The impact of eddy diffusion on the simulated tidal phase is very minimal. The NoEdShift experiment demonstrates that employing the global seasonal variations of Q09 without applying a 30-day shift toward the mid- to high-latitude variations of the Garcia and Solomon (1985) model, damps the tide less strongly between May and June, more strongly between July and September, and slightly less strongly in December. Here the changes between May-June and July-September represent especially strong departures from PRISM-SDARN and the (climatological) observed tide.

Figures 6c and 6f compare PRISM-SDARN against simulations where the surface friction coefficient has been reduced by a factor of 0.5 (SurfReduc), and where it has been enhanced by a factor of 1.5 (SurfEnhan). These

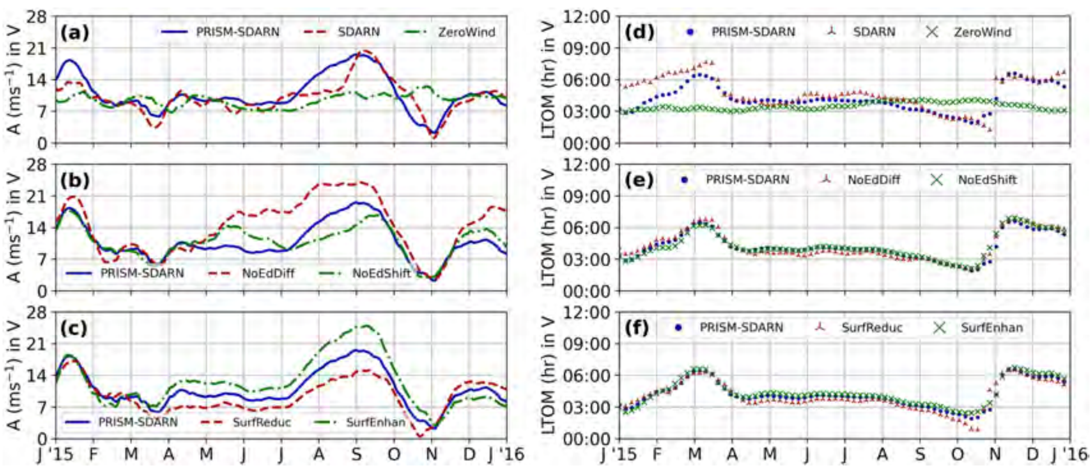

Figure 6. Meridional component of the migrating semidiurnal (SW2) observed by Super Dual Auroral Radar Network (SDARN) and the SW2 simulation results for the ZeroWind and PRISM-SDARN (a, d), NoEdDiff and NoEdShift (b, e), and SurfReduc and SurfEnhan (c, f) simulations as listed in Table 1.

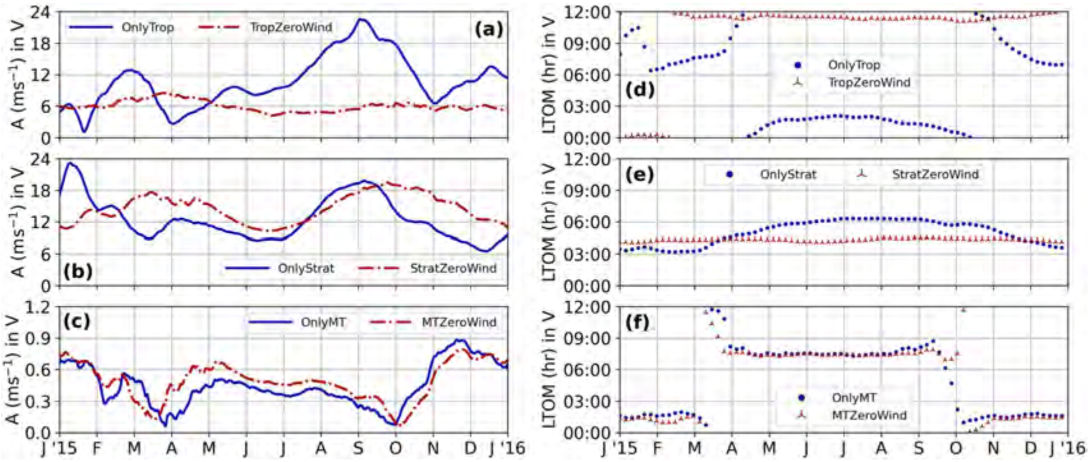

Figure 7. Meridional migrating semidiurnal forcing response for the OnlyTrop and TropZeroWind (a, d), OnlyStrat and StratZeroWind (b, e), and OnlyMT and MTZeroWind (c, f) numerical experiments. Note the different *y*-axis scaling in panel (c).

experiments demonstrate that the main impact of increased surface friction is to enhance the simulated amplitudes between April–October, with the enhancement being most pronounced between August–September. Furthermore, the amplitude increase shows an almost perfectly linear relationship with the strength of the surface friction coefficient A_0. This relation is also confirmed in diagnostic simulations for values of A_0 outside of the range shown here, starting from zero and up to 10 d^{-1}. The simulated phase is impacted by surface friction to a lesser extent, but is generally delayed as surface friction increases. The yearly mean LTOM is 03:59, 04:09, and 04:18 hr for the SurfReduc, PRISM-SDARN, and SurfEnhan simulations, respectively. This delay is consistent with the results of Sakazaki and Hamilton (2017), who found a doubling of their specification of surface friction to delay the phase of the SW2 component of the surface tide by about 10 min. We further note that the impact of surface friction is not exclusive to the simulated SW2 tide observed by SuperDARN, but that the model indicates that it extends across the mid- and high-latitude MLT.

Diagnostic simulations without either surface friction or eddy diffusion also find the simulated magnitude of the August–September amplitude maximum to be substantially smaller than that of the observed tide. The inclusion of surface friction is therefore required to make the simulated amplitude match the observed September maximum. Owing to this sensitivity, the surface friction value of $A_0 = 3.0$ d^{-1} was determined to yield the best agreement with observation. This choice of A_0 does, however, fall well within the range of surface friction values described in literature. For example, Stevens et al. (2002) find a surface Rayleigh friction value of 1.9 d^{-1} over the tropical pacific ocean, while Yang et al. (2013) find surface Rayleigh friction values up to 5.5 d^{-1} over land.

5. Forcing Decomposition

To investigate the impact of the background atmosphere on the simulated SW2 tide in more detail, a distinction is made between the SW2 tide forced in the troposphere, stratosphere, and MT regions (see Section 2.4). This is motivated by the vertical propagation path to SuperDARN meteor echo heights (75–125 km) being considerably different for the tides forced within these regions. For example, the peak forcing altitude in the troposphere occurs near the surface, in the stratosphere near 40 km, and in the MT near 170 km (as shown in Figure 4). To compare the baseline effect on the forcing response from the different regions, Figure 7 compares the tropospheric (OnlyTrop), stratospheric (OnlyStrat), and MT (OnlyMT) SW2 forcing simulations against corresponding zero-wind tropospheric (TropZeroWind), stratospheric (StratZeroWind), and MT (MTZeroWind) simulations. An overview of these experiments is given in Table 2.

By comparison with the TropZeroWind simulations, the OnlyTrop experiment demonstrates that the seasonal variations of the NAVHWER atmosphere induce strong seasonal variations in both the amplitude and phase

Table 2
Forcing Decomposition Experiment Design

Experiment	Configuration
OnlyTrop	As PRISM-SDARN, tide forced only between 1,000–100 hPa
OnlyStrat	As PRISM-SDARN, tide forced only between 100–0.1 hPa
OnlyMT	As PRISM-SDARN, tide forced only between 0.1–10^{-7} hPa
TropZeroWind	As OnlyTrop, zero-wind background atmosphere
StratZeroWind	As OnlyStrat, zero-wind background atmosphere
MTZeroWind	As OnlyMT, zero-wind background atmosphere

Note. SDARN, Super Dual Auroral Radar Network.

of the tropospheric SW2 forcing response. The amplitude of the forcing response is enhanced by as much as a factor of 4, while a roughly bi-modal phase behavior is established between the summer and winter half-year. An exception to the latter occurs in January, when the phase is delayed coincident with a local amplitude minimum.

The stratospheric forcing response is comparatively less affected by the seasonal variations in the background atmosphere. The main amplitude enhancement occurs in January, with lower amplitudes during much of the rest of the year. The phase is delayed by 2.5 hr at most, and shows no signs of major seasonal variations. Further, while it is impossible to determine if the behavior of the stratospheric and tropospheric forcing response during January represents a seasonal effect or isolated event based on a 1-year simulation, it is interesting to note that January was marked by a minor sudden stratospheric warming event (Manney et al., 2015).

Both the amplitude and phase of the MT forcing response show a bi-modal seasonal behavior, which is largely unchanged between the OnlyMT and MTZeroWind simulations. The amplitudes broadly maximize during the summer and winter seasons, having minima in March and October. The bi-modal characteristics of the MT forcing response are reminiscent of the mid- to high-latitude structure of the SW2 forcing in the MLT described by Hagan (1996). There an anti-symmetric latitudinal structure in the SW2 tide forcing between summer and winter solstice is associated with changes in the forcing brought about by the secondary ozone maximum. Consistent with their results is that the MT forcing response in our simulations is entirely attributable to shortwave radiation effects. However, since the MT forcing response is comparatively insignificant relative to those of the troposphere and stratosphere, a more detailed investigation into its drivers is not included in the current work.

6. Conclusion and Discussion

This study uses a primitive equation model to simulate the SW2 tide observed by a longitudinal array of SuperDARN meteor radars for the year 2015, to mechanistically identify which processes contribute to the seasonal variations of the SW2 tide in the mid- to high-latitude MLT. The model convincingly reproduces the observed seasonal variations in the tidal amplitude and phase, which include amplitude maxima in September and in winter, and rapid phase transitions coincident with amplitude minima in March and October.

By comparison with zero-wind simulations, the seasonal characteristics of the SW2 tide are found to be shaped largely by the seasonal variations in the background atmosphere. While this result is consistent with literature (e.g., Hagan et al., 1999; Lindzen & shung Hong, 1974), numerical experiments find it to be almost entirely attributable to the SW2 tide forced in the troposphere. The background atmosphere amplifies the amplitude of the tropospheric forcing response by as much as a factor of 4, while also giving rise to rapid phase transitions in March and April. In contrast, the amplitude of the stratospheric forcing response is impacted only by a factor of 0.8–0.9 throughout most of the year, while its phase displays no major seasonal variations. As a consequence of the tropospheric amplification, the contribution to the net simulated tide becomes comparable in magnitude between the tides forced in the troposphere and stratosphere regions, consistent with the results of Hagan (1996). The contribution to the net simulated tide by the tide forced in the mesosphere-thermosphere region is found to be much smaller, reaching an amplitude of at most 0.9 ms^{-1}.

Tidal damping by eddy diffusion is parameterized as a seasonally dependent effective Rayleigh friction. The primary effect of eddy diffusion is to reduce the simulated SW2 amplitudes by a factor of ~0.5 broadly around summer solstice and in December. The tidal damping around summer solstice represents an important factor in bringing the model into agreement with observation. In simulations without eddy diffusion, the summertime amplitude maximum is much broader than observation, with amplitudes beginning to increase as early as May. Tidal dissipation by eddy diffusion may therefore be an important factor contributing to the summertime discrepancies between modeled and observed semidiurnal tides (e.g., Pancheva et al., 2020; Stober et al., 2020, 2021).

The specification of a narrow surface friction layer is found to increase the net amplitude of the simulated SW2 tide in the MLT between April and October. Especially the increased amplitudes between August and September represent an important factor in bringing the amplitude of the simulated tide in agreement with observation. Using diagnostic simulations where surface reflections are artificially removed, the effect of surface friction is identified as being caused by its dampening effect on the surface reflection of the tide. This in turn changes the complex interference pattern between the tides forced in the different source regions and their respective surface reflections. Given the implications of surface friction as a coupling mechanism between the boundary layer and semidiurnal tidal variability in the MLT, the mechanism and impact of surface friction will be investigated in more detail in a future study by means of a Hough-mode decomposition. In addition, future efforts can focus on the implementation of a more realistic spatially and temporally varying implementation of surface friction. This would include, for example, longitudinal ocean and land contrasts (Chiang & Zebiak, 2000; Yang et al., 2013). Based on our results for the SW2 tide, we anticipate that surface friction may serve as a possible excitation mechanism for non-migrating semidiurnal tides. A more realistic specification of surface friction would also include different zonal and meridional surface friction coefficients (Stevens et al., 2002). The lack of such a distinction may be a factor contributing to the simulated tide having the same amplitude in the zonal and meridional wind, whereas the observed tides frequently show different amplitudes.

Data Availability Statement

SuperDARN data are available from Virginia Tech at http://vt.superdarn.org/tiki-index.php, last access: September 2021. SD-WACCMX data are available at https://www.earthsystemgrid.org CCSM run SD-WACCM-X v2.1, Atmosphere History Data, 3-Hourly Instantaneous Values, version 7, last access: September 2021.

Acknowledgments
The current research was supported by the Research Council of Norway (grant no. 223525/F50). The authors acknowledge the use of NAVGEM-HA data and SuperDARN meteor wind data. Development of NAVGEM-HA was supported by the Chief of Naval Research and the Department of Defense High Performance Computing Modernization Project. The SuperDARN project is funded by national scientific funding agencies of Australia, China, Canada, France, Japan, Italy, Norway, South Africa, the United Kingdom, and the United States. The authors are deeply indebted to R. S. Lieberman, whose kindness and support made the modeling aspect of this work possible. We also thank the support from the NASA TIMED program.

References

Arras, C., Jacobi, C., & Wickert, J. (2009). Semidiurnal tidal signature in sporadic e occurrence rates derived from GPS radio occultation measurements at higher midlatitudes. *Annales Geophysicae*, *27*(6), 2555–2563. https://doi.org/10.5194/angeo-27-2555-2009

Becker, E. (2017). Mean-flow effects of thermal tides in the mesosphere and lower thermosphere. *Journal of the Atmospheric Sciences*, *74*(6), 2043–2063. https://doi.org/10.1175/JAS-D-16-0194.1

Chapman, S., & Lindzen, R. S. (1970). *Atmospheric tides*. Springer Netherlands. https://doi.org/10.1007/978-94-010-3399-2

Chen, G., Held, I. M., & Robinson, W. A. (2007). Sensitivity of the latitude of the surface westerlies to surface friction. *Journal of the Atmospheric Sciences*, *64*(8), 2899–2915. https://doi.org/10.1175/jas3995.1

Chiang, J. C. H., & Zebiak, S. E. (2000). Surface wind over tropical oceans: Diagnosis of the momentum balance, and modeling the linear friction coefficient. *Journal of Climate*, *13*(10), 1733–1747. https://doi.org/10.1175/1520-0442(2000)013<1733:swotod>2.0.co;2

Chisham, G. (2018). Calibrating SuperDARN interferometers using meteor backscatter. *Radio Science*, *53*(6), 761–774. https://doi.org/10.1029/2017rs006492

Chisham, G., & Freeman, M. P. (2013). A reassessment of SuperDARN meteor echoes from the upper mesosphere and lower thermosphere. *Journal of Atmospheric and Solar-Terrestrial Physics*, *102*, 207–221. https://doi.org/10.1016/j.jastp.2013.05.018

Conte, J. F., Chau, J. L., Laskar, F. I., Stober, G., Schmidt, H., & Brown, P. (2018). Semidiurnal solar tide differences between fall and spring transition times in the northern hemisphere. *Annales Geophysicae*, *36*(4), 999–1008. https://doi.org/10.5194/angeo-36-999-2018

Dhadly, M. S., Emmert, J. T., Drob, D. P., McCormack, J. P., & Niciejewski, R. J. (2018). Short-term and interannual variations of migrating diurnal and semidiurnal tides in the mesosphere and lower thermosphere. *Journal of Geophysical Research: Space Physics*, *123*(8), 7106–7123. https://doi.org/10.1029/2018ja025748

Drob, D. P., Emmert, J. T., Meriwether, J. W., Makela, J. J., Doornbos, E., Conde, M., et al. (2015). An update to the horizontal wind model (HWM): The quiet time thermosphere. *Earth and Space Science*, *2*(7), 301–319. https://doi.org/10.1002/2014ea000089

Eckermann, S. D., Ma, J., Hoppel, K. W., Kuhl, D. D., Allen, D. R., Doyle, J. A., et al. (2018). High-altitude (0–100 km) global atmospheric reanalysis system: Description and application to the 2014 austral winter of the deep propagating gravity wave experiment (DEEPWAVE). *Monthly Weather Review*, *146*(8), 2639–2666. https://doi.org/10.1175/mwr-d-17-0386.1

Forbes, J. M. (1982). Atmospheric tide: 2. The solar and lunar semidiurnal components. *Journal of Geophysical Research*, *87*(A7), 5241–5252. https://doi.org/10.1029/ja087ia07p05241

Forbes, J. M. (2009). Vertical coupling by the semidiurnal tide in Earth's atmosphere. In T. Tsuda, R. Fujii, K. Shibata, & M. A. Geller (Eds.), *Climate and weather of the Sun-Earth system (CAWSES): Selected papers from the 2007 Kyoto Symposium* (pp. 337–348). TERRAPUB.

Forbes, J. M., & Garrett, H. B. (1979). Theoretical studies of atmospheric tides. *Reviews of Geophysics*, *17*(8), 1951–1981. https://doi.org/10.1029/RG017i008p01951

Forbes, J. M., Roble, R. G., & Fesen, C. G. (1993). Acceleration, heating, and compositional mixing of the thermosphere due to upward propagating tides. *Journal of Geophysical Research*, *98*(A1), 311–321. https://doi.org/10.1029/92JA00442

Forbes, J. M., & Vincent, R. A. (1989). Effects of mean winds and dissipation on the diurnal propagating tide: An analytic approach. *Planetary and Space Science*, *37*(2), 197–209. https://doi.org/10.1016/0032-0633(89)90007-X

Garcia, R. R., & Solomon, S. (1985). The effect of breaking gravity waves on the dynamics and chemical composition of the mesosphere and lower thermosphere. *Journal of Geophysical Research*, *90*(D2), 3850–3868. https://doi.org/10.1029/JD090iD02p03850

Gelaro, R., McCarty, W., Suárez, M. J., Todling, R., Molod, A., Takacs, L., et al. (2017). The modern-era retrospective analysis for research and applications, version 2 (MERRA-2). *Journal of Climate*, *30*(14), 5419–5454. https://doi.org/10.1175/jcli-d-16-0758.1

Hagan, M. E. (1996). Comparative effects of migrating solar sources on tidal signatures in the middle and upper atmosphere. *Journal of Geophysical Research*, *101*(D16), 21213–21222. https://doi.org/10.1029/96jd01374

Hagan, M. E., Burrage, M. D., Forbes, J. M., Hackney, J., Randel, W. J., & Zhang, X. (1999). GSWM-98: Results for migrating solar tides. *Journal of Geophysical Research*, *104*(A4), 6813–6827. https://doi.org/10.1029/1998ja900125

Hagan, M. E., Forbes, J. M., & Vial, F. (1993). Numerical investigation of the propagation of the quasi-two-day wave into the lower thermosphere. *Journal of Geophysical Research*, *98*(D12), 23193–23205. https://doi.org/10.1029/93JD02779

Hagan, M. E., Forbes, J. M., & Vial, F. (1995). On modeling migrating solar tides. *Geophysical Research Letters*, *22*(8), 893–896. https://doi.org/10.1029/95GL00783

He, M., & Chau, J. L. (2019). Mesospheric semidiurnal tides and near-12 h waves through jointly analyzing observations of five specular meteor radars from three longitudinal sectors at boreal midlatitudes. *Atmospheric Chemistry and Physics*, *19*(9), 5993–6006. https://doi.org/10.5194/acp-19-5993-2019

Hersbach, H., Bell, B., Berrisford, P., Hirahara, S., Horányi, A., Muñoz-Sabater, J., et al. (2020). The ERA5 global reanalysis. *Quarterly Journal of the Royal Meteorological Society*, *146*(730), 1999–2049. https://doi.org/10.1002/qj.3803

Holton, J. R. (2003). *An introduction to dynamic meteorology* (4th ed.). Academic Press.

Hong, S.-S., & Lindzen, R. S. (1976). Solar semidiurnal tide in the thermosphere. *Journal of the Atmospheric Sciences*, *33*(1), 135–153. https://doi.org/10.1175/1520-0469(1976)033<0135:sstitt>2.0.co;2

Hussey, G. C., Meek, C. E., André, D., Manson, A. H., Sofko, G. J., & Hall, C. M. (2000). A comparison of northern hemisphere winds using SuperDARN meteor trail and mf radar wind measurements. *Journal of Geophysical Research*, *105*(D14), 18053–18066. https://doi.org/10.1029/2000JD900272

Laskar, F. I., McCormack, J. P., Chau, J. L., Pallamraju, D., Hoffmann, P., & Singh, R. P. (2019). Interhemispheric meridional circulation during sudden stratospheric warming. *Journal of Geophysical Research: Space Physics*, *124*(8), 7112–7122. https://doi.org/10.1029/2018ja026424

Lieberman, R. S., France, J., Ortland, D. A., & Eckermann, S. D. (2021). The role of inertial instability in cross-hemispheric coupling. *Journal of the Atmospheric Sciences*, *78*(4), 1113–1127. https://doi.org/10.1175/JAS-D-20-0119.1

Lieberman, R. S., Riggin, D. M., Ortland, D. A., Oberheide, J., & Siskind, D. E. (2015). Global observations and modeling of nonmigrating diurnal tides generated by tide-planetary wave interactions. *Journal of Geophysical Research: Atmospheres*, *120*(22), 11419–11437. https://doi.org/10.1002/2015JD023739

Lindzen, R. S., & shung Hong, S. (1974). Effects of mean winds and horizontal temperature gradients on solar and lunar semidiurnal tides in the atmosphere. *Journal of the Atmospheric Sciences*, *31*(5), 1421–1446. https://doi.org/10.1175/1520-0469(1974)031<1421:eomwah>2.0.co;2

Liu, G., Lieberman, R. S., Harvey, V. L., Pedatella, N. M., Oberheide, J., Hibbins, R. E., et al. (2021). Tidal variations in the mesosphere and lower thermosphere before, during, and after the 2009 sudden stratospheric warming. *Journal of Geophysical Research: Space Physics*, *126*(3), e2020JA028827. https://doi.org/10.1029/2020JA028827

Liu, H.-L., Bardeen, C. G., Foster, B. T., Lauritzen, P., Liu, J., Lu, G., et al. (2018). Development and validation of the whole atmosphere community climate model with thermosphere and ionosphere extension (WACCM-x 2.0). *Journal of Advances in Modeling Earth Systems*, *10*(2), 381–402. https://doi.org/10.1002/2017ms001232

Manney, G. L., Lawrence, Z. D., Santee, M. L., Read, W. G., Livesey, N. J., Lambert, A., et al. (2015). A minor sudden stratospheric warming with a major impact: Transport and polar processing in the 2014/2015 Arctic winter. *Geophysical Research Letters*, *42*(18), 7808–7816. https://doi.org/10.1002/2015GL065864

Manson, A. H., Meek, C., Hagan, M., Koshyk, J., Franke, S., Fritts, D., et al. (2002). Seasonal variations of the semi-diurnal and diurnal tides in the MLT: Multi-year MF radar observations from 2–70°n, modelled tides (GSWM, CMAM). *Annales Geophysicae*, *20*(5), 661–677. https://doi.org/10.5194/angeo-20-661-2002

Maute, A., Fejer, B. G., Forbes, J. M., Zhang, X., & Yudin, V. (2016). Equatorial vertical drift modulation by the lunar and solar semidiurnal tides during the 2013 sudden stratospheric warming. *Journal of Geophysical Research: Space Physics*, *121*(2), 1658–1668. https://doi.org/10.1002/2015JA022056

McCormack, J. P., Harvey, V. L., Pedatella, N., Koshin, D., Sato, K., Coy, L., et al. (2021). Intercomparison of middle atmospheric meteorological analyses for the northern hemisphere winter 2009-2010. *Atmospheric Chemistry and Physics Discussions*, *2021*, 1–48. https://doi.org/10.5194/acp-2021-224

McCormack, J. P., Hoppel, K., Kuhl, D., de Wit, R., Stober, G., Espy, P., et al. (2017). Comparison of mesospheric winds from a high-altitude meteorological analysis system and meteor radar observations during the boreal winters of 2009–2010 and 2012–2013. *Journal of Atmospheric and Solar-Terrestrial Physics*, *154*, 132–166. https://doi.org/10.1016/j.jastp.2016.12.007

McLandress, C. (2002). The seasonal variation of the propagating diurnal tide in the mesosphere and lower thermosphere. Part ii: The role of tidal heating and zonal mean winds. *Journal of the Atmospheric Sciences*, *59*(5), 907–922. https://doi.org/10.1175/1520-0469(2002)059<0907:tsvotp>2.0.co;2

Ortland, D. A. (2017). Daily estimates of the migrating tide and zonal mean temperature in the mesosphere and lower thermosphere derived from SABER data. *Journal of Geophysical Research: Atmospheres*, *122*(7), 3754–3785. https://doi.org/10.1002/2016jd025573

Ortland, D. A., & Alexander, M. J. (2006). Gravity wave influence on the global structure of the diurnal tide in the mesosphere and lower thermosphere. *Journal of Geophysical Research*, *111*(A10). https://doi.org/10.1029/2005JA011467

Ortland, D. A., & Alexander, M. J. (2014). The residual-mean circulation in the tropical tropopause layer driven by tropical waves. *Journal of the Atmospheric Sciences*, *71*(4), 1305–1322. https://doi.org/10.1175/JAS-D-13-0100.1

Ortland, D. A., Alexander, M. J., & Grimsdell, A. W. (2011). On the wave spectrum generated by tropical heating. *Journal of the Atmospheric Sciences*, *68*(9), 2042–2060. https://doi.org/10.1175/2011JAS3718.1

Pancheva, D., Mukhtarov, P., Hall, C., Meek, C., Tsutsumi, M., Pedatella, N., & Nozawa, S. (2020). Climatology of the main (24-h and 12-h) tides observed by meteor radars at Svalbard and Tromsø: Comparison with the models CMAM-DAS and WACCM-X. *Journal of Atmospheric and Solar-Terrestrial Physics*, *207*, 105339. https://doi.org/10.1016/j.jastp.2020.105339

Pedatella, N. M., & Forbes, J. M. (2010). Evidence for stratosphere sudden warming-ionosphere coupling due to vertically propagating tides. *Geophysical Research Letters*, *37*(11). https://doi.org/10.1029/2010GL043560

Pedatella, N. M., Liu, H.-L., Conte, J. F., Chau, J. L., Hall, C., Jacobi, C., et al. (2020). Migrating semidiurnal tide during the September equinox transition in the northern hemisphere. *Journal of Geophysical Research: Atmospheres*, e2020JD033822. https://doi.org/10.1029/2020JD033822

Picone, J. M., Hedin, A. E., Drob, D. P., & Aikin, A. C. (2002). NRLMSISE-00 empirical model of the atmosphere: Statistical comparisons and scientific issues. *Journal of Geophysical Research*, *107*(A12), SIA15–1–SIA15–16. https://doi.org/10.1029/2002ja009430

Pilinski, M. D., & Crowley, G. (2015). Seasonal variability in global eddy diffusion and the effect on neutral density. *Journal of Geophysical Research: Space Physics*, *120*(4), 3097–3117. https://doi.org/10.1002/2015JA021084

Qian, L., Solomon, S. C., & Kane, T. J. (2009). Seasonal variation of thermospheric density and composition. *Journal of Geophysical Research*, *114*(A1). https://doi.org/10.1029/2008JA013643

Sakazaki, T., & Hamilton, K. (2017). Physical processes controlling the tide in the tropical lower atmosphere investigated using a comprehensive numerical model. *Journal of the Atmospheric Sciences*, *74*(8), 2467–2487. https://doi.org/10.1175/jas-d-17-0080.1

Sandford, D. J., Muller, H. G., & Mitchell, N. J. (2006). Observations of lunar tides in the mesosphere and lower thermosphere at arctic and middle latitudes. *Atmospheric Chemistry and Physics*, *6*(12), 4117–4127. https://doi.org/10.5194/acp-6-4117-2006

Shepherd, G., Roble, R. G., Zhang, S.-P., McLandress, C., & Wiens, R. H. (1998). Tidal influence on midlatitude airglow: Comparison of satellite and ground-based observations with time-GCM predictions. *Journal of Geophysical Research*, *103*(A7), 14741–14751. https://doi.org/10.1029/98JA00884

Shepherd, T. G., Semeniuk, K., & Koshyk, J. (1996). Sponge layer feedbacks in middle-atmosphere models. *Journal of Geophysical Research*, *101*(D18), 23447–23464. https://doi.org/10.1029/96JD01994

Smith, A. K. (2012). Global dynamics of the MLT. *Surveys in Geophysics*, *33*(6), 1177–1230. https://doi.org/10.1007/s10712-012-9196-9

Stevens, B., Duan, J., McWilliams, J. C., Münnich, M., & Neelin, J. D. (2002). Entrainment, Rayleigh friction, and boundary layer winds over the tropical pacific. *Journal of Climate*, *15*(1), 30–44. https://doi.org/10.1175/1520-0442(2002)015<0030:erfabl>2.0.co;2

Stober, G., Baumgarten, K., McCormack, J. P., Brown, P., & Czarnecki, J. (2020). Comparative study between ground-based observations and NAVGEM-HA analysis data in the mesosphere and lower thermosphere region. *Atmospheric Chemistry and Physics*, *20*(20), 11979–12010. https://doi.org/10.5194/acp-20-11979-2020

Stober, G., Kuchar, A., Pokhotelov, D., Liu, H., Liu, H.-L., Schmidt, H., et al. (2021). Interhemispheric differences of mesosphere/lower thermosphere winds and tides investigated from three whole atmosphere models and meteor radar observations. *Atmospheric Chemistry and Physics Discussions*, 1–50. https://doi.org/10.5194/acp-2021-142

Teitelbaum, H., & Vial, F. (1991). On tidal variability induced by nonlinear interaction with planetary waves. *Journal of Geophysical Research*, *96*(A8), 14169–14178. https://doi.org/10.1029/91JA01019

van Caspel, W. E., Espy, P. J., Hibbins, R. E., & McCormack, J. P. (2020). Migrating tide climatologies measured by a high-latitude array of SuperDARN HF radars. *Annales Geophysicae*, *38*(6), 1257–1265. https://doi.org/10.5194/angeo-38-1257-2020

Vial, F. (1986). Numerical simulations of atmospheric tides for solstice conditions. *Journal of Geophysical Research*, *91*(A8), 8955. https://doi.org/10.1029/ja091ia08p08955

Wood, A. R., & Andrews, D. G. (1997). A spectral model for simulation of tides in the middle atmosphere. III: Results for the semidiurnal tide. *Journal of Atmospheric and Solar-Terrestrial Physics*, *59*(1), 79–97. https://doi.org/10.1016/1364-6826(95)00188-3

Wu, Q., Ortland, D., Solomon, S., Skinner, W., & Niciejewski, R. (2011). Global distribution, seasonal, and inter-annual variations of mesospheric semidiurnal tide observed by TIMED TIDI. *Journal of Atmospheric and Solar-Terrestrial Physics*, *73*(17), 2482–2502. https://doi.org/10.1016/j.jastp.2011.08.007

Yang, W., Seager, R., & Cane, M. A. (2013). Zonal momentum balance in the tropical atmospheric circulation during the global monsoon mature months. *Journal of the Atmospheric Sciences*, *70*(2), 583–599. https://doi.org/10.1175/jas-d-12-0140.1

Zhang, J., Limpasuvan, V., Orsolini, Y. J., Espy, P. J., & Hibbins, R. E. (2021). Climatological westward-propagating semidiurnal tides and their composite response to sudden stratospheric warmings in SuperDARN and SD-WACCM-X. *Journal of Geophysical Research: Atmospheres*, *126*(3), e2020JD032895. https://doi.org/10.1029/2020JD032895

Paper III

van Caspel, W. E., Espy, P. J., Hibbins, R. E., Stober, G., Chartier, A., Brown, P., Jacobi, C., Kero, J., & Belova, E. A case study of the solar and lunar semidiurnal tide response to the 2013 major sudden stratospheric warming event. *Prepared for Submission to Journal of Geophysical Research: Atmospheres*.

A case study of the solar and lunar semidiurnal tide response to the 2013 major sudden stratospheric warming event

Willem E. van Caspel[1,2], Patrick Espy[1,2], Robert Hibbins[1,2], Gunter Stober[3], Alex Chartier[4], Peter Brown[5], Christoph Jacobi[6], Johan Kero[7], Evgenia Belova[7]

[1]Department of Physics, Norwegian University of Science and Technology (NTNU), Trondheim, Norway
[2]Birkeland Centre for Space Science, Bergen, Norway
[3]Institute of Applied Physics and Oeschger Center for Climate Change Research, Microwave Physics, University of Bern, Bern, Switzerland
[4]John Hopkins University Applied Physics Laboratory, Laurel, MD, USA
[5]Department of Physics and Astronomy, Western University, London, Ontario, Canada
[6]Leipzig University, Leipzig, Germany
[7]Swedish Institute of Space Physics, Kiruna, Sweden

Key Points:

- The semidiurnal tide (SDT) response to the 2013 sudden stratospheric warming is investigated using meteor wind observations and mechanistic tidal model simulations
- Individual lunar and solar SDT simulations are performed to assess their relative importance in establishing the net simulated SDT response
- The dominant solar SDT response is driven by changing propagation conditions and non-linear interactions with quasi-stationary planetary waves

Corresponding author: Willem van Caspel, `willem.e.v.caspel@ntnu.no`

Abstract

The semidiurnal tide (SDT) response to the 2013 major sudden stratospheric warming (SSW) is investigated using a range of mid- and high-latitude meteor radars and mechanistic primitive equation model simulations. In the model, the background atmosphere is specified to daily mean winds and temperatures from the Navy Global Environmental Model – High Altitude (NAVGEM-HA) meteorological analysis system. The solar (thermal) SDT component is forced by incorporating hourly global temperature tendency fields from the ERA5 forecast model, and the lunar SDT component is forced by incorporating the lunar gravitational potentials and the lunar ocean, Earth, and load tide contributions. The net simulated SDT response is validated against meteor wind observations made by the CMOR (43.3°N, 80.8°W), Collm (51.3°N, 13.0°E), and Kiruna (67.5°N, 20.1°E) radars in the mesosphere-lower-thermosphere (MLT). In addition, the simulated migrating SDT response is validated against meteor wind observations made by a longitudinal chain of high-latitude SuperDARN radars. Numerical experiments are performed to identify the individual role of the solar and lunar SDT components on the simulation results, including the individual impact of the background atmosphere, non-linear wave-wave interactions, and the SSW-induced stratospheric ozone perturbation. Results find that the majority of the net SDT response can be attributed to that of the solar SDT, which is driven by the changing propagation conditions through the background atmosphere and by non-linear wave-wave interactions. Nevertheless, the modeled lunar SDT is found to enhance most strongly for altitudes between 105-130 km, where it can reach amplitudes of up to 35-40% of that of the solar SDT in the lower thermosphere.

1 Introduction

Sudden stratospheric warmings (SSWs) are large-scale dynamical events during which the wintertime stratospheric temperatures are rapidly increased by tens of degrees of Kelvin, accompanied by a reversal of the otherwise climatological westerly winds of the stratospheric polar vortex (Baldwin et al., 2021). SSWs are caused by planetary waves propagating from the troposphere up into the stratosphere, leading to the subsequent displacement or splitting of the polar vortex. While the majority of the dynamical changes associated with SSWs occur in the mid- and high-latitude stratosphere, their impact can extend from the troposphere up into the thermosphere (Limpasuvan et al., 2016). For the mid- and high-latitude mesosphere-lower-thermosphere (MLT, 80-110 km altitude), one of the major sources of SSW-induced variability is associated with the induced changes to the semidiurnal atmospheric tide (Baldwin et al., 2021).

The semidiurnal tide (SDT) is a near 12-hour oscillation in the winds, temperature, density, and pressure (Chapman & Lindzen, 1970). While the SDT is predominantly excited by radiative and latent heating effects in the troposphere and stratosphere, its largest amplitudes are obtained in the MLT due to the decreasing density of the atmosphere in altitude (Hagan, 1996). At these altitudes, the SDT is furthermore observed in a range of ionospheric parameters, such as equatorial $E\times B$ plasma drift velocities, F-region electron densities, and ion temperatures (Pedatella et al., 2014). The SDT thereby represents an important mechanism coupling the variability of the lower and middle atmosphere to that of the ionosphere and upper atmosphere (Pedatella & Forbes, 2010; Forbes, 2009). Consequently, the SDT response to SSWs has been a much studied subject (Goncharenko et al., 2021). Open questions nevertheless remain about the spatio-temporal drivers of the atmospheric and ionospheric SDT response, especially regarding the influence of the different migrating and non-migrating solar and lunar SDT components (Goncharenko et al., 2022; J. Liu et al., 2021; G. Liu et al., 2021; J. Zhang et al., 2021; Wu et al., 2019).

A challenging aspect of the SSW-induced SDT response is that it involves a large number of physical mechanisms. These include the changing propagation conditions of the solar (thermal) 12.00 hr and lunar 12.42 hr (M_2) and 12.66 hr (N_2) SDT components (Forbes & Zhang, 2012; Jin et al., 2012), non-linear wave-wave interactions with quasi-stationary planetary waves (H.-L. Liu et al., 2010), and changes in the thermal forcing caused by a redistribution of stratospheric ozone (Goncharenko et al., 2012). Investigating the SDT response is furthermore complicated by the difficult nature of separating the individual contributions of the different forcing mechanisms to the net observed or simulated SDT. For example, a time window of at least 15 days is required to separate the lunar and solar SDT components (Lin et al., 2019), while satellite observations of migrating and non-migrating tides are also limited to time resolutions upwards of 15 days (J. Liu et al., 2021; X. Zhang & Forbes, 2014a). The use of long window lengths can lead to a highly smoothed and possibly cross-contaminated view of the SDT response, considering that SSW-induced SDT variability can occur on the timescales of a few days (Stober et al., 2020).

In this study, SDT observations from a range of Northern Hemisphere mid- and high-latitude meteor radars are simulated using a mechanistic tide model for the 2013 major SSW event. The model is a development of the primitive equations in sigma-coordinates model (PRISM) used by van Caspel et al. (2022) to simulate the seasonal variations of the mid- to high-latitude migrating solar SDT component. Leveraging the mechanistic nature of PRISM, the individual contributions of the different forcing mechanism on the neutral atmospheric SDT response can be investigated.

In Section 2 the model implementation of the solar and lunar tidal forcing and background atmospheric specification is discussed. Section 3 validates the simulated SDT response against neutral wind observations from the CMOR (43.3°N, 80.8°W), Collm (51.3°N, 13.0°E), and Kiruna (67.5°N, 20.1°E) meteor radars, in addition to the migrating SDT measured by an array of high-latitude SuperDARN meteor radars. Section 3 also compares individual simulations of the solar and lunar SDT response against the net observed and simulated SDT. In Section 4, numerical experiments are performed to isolate the impact of the changing propagation conditions through the background atmosphere, non-linear wave-wave interactions between the migrating SDT and quasi-stationary planetary waves, and stratospheric ozone perturbations. The results are discussed and concluded in Section 5.

2 Model Description

PRISM is a non-linear and time dependent spectral model, having a model top around 430 km altitude. The model includes a specification of tidal dissipation by ion drag, Newtonian cooling, eddy and molecular diffusion of momentum and heat, and surface friction. For the simulations presented in the current work, the horizontal resolution is truncated at zonal wavenumber S = 9 and meridional wavenumber N = 24. While a detailed description of the model is given by van Caspel et al. (2022) and references therein, those aspects of the model which have been modified for the current work are discussed in more detail in the following.

2.1 Background Atmosphere

The background atmosphere in PRISM can be freely specified by relaxing the model toward an assimilation state. For this, a nudging rate of $D = 1/3$ days^{-1} (d^{-1}) is employed in the current work. This nudging rate is high enough for the spatial and temporal evolution of the polar vortex to be well represented in the model, while being low enough to have no impact on the simulated SDT wave-field. However, the artificially imposed planetary waves of the polar vortex can impact the zonal mean model state through first-order wave-mean flow interactions (Pedatella & Liu, 2013). To reduce the impact of this effect, the zonal mean spherical harmonic coefficients are nudged with a rate of $D_0 = 1$ d^{-1}. While this nudging factor may suppress the non-migrating zonal mean semidiurnal tide, diagnostic simulations find that this tidal component does not contribute to the simulation results.

The background atmosphere between 85-0.001 hPa (∼10-95 km altitude) is nudged towards daily mean winds and temperatures calculated from 3-hourly data from the NAVGEM-HA meteorological analysis system. NAVGEM-HA assimilates satellite observations of ozone, water vapor, and temperatures in the stratosphere and mesosphere, in addition to standard operational meteorological observations in the troposphere (McCormack et al., 2017). NAVGEM-HA mean winds and temperatures have been shown to be in good agreement with observations for the 2013 SSW (McCormack et al., 2017; Stober et al., 2020). Fig. 1a illustrates the temporal evolution of the 2013 SSW in NAVGEM-HA and PRISM, using the definition of polar vortex weakening (PVW) as defined by X. Zhang and Forbes (2014b). Using this definition, which considers the zonal mean zonal winds at 48 km altitude and 70°N and the zonal mean temperatures at 40 km altitude and 90°N, the day of peak PVW occurs on the 11th of January 2013 (or 41 days after the starting date for the analysis, the 1st of December 2012). During peak PVW, the zonal mean zonal winds at 48 km altitude and 70°N are at their most easterly, and the zonal mean temperatures at 40 km altitude and 90°N reach their maximum value. Within the context of this work, the SSW onset is taken to occur when the zonal mean zonal winds at 48 km altitude and 70°N reverse, on the 4th of January. The recovery phase is taken to commence when the zonal mean zonal winds return to their climatological westerlies on the 23rd of January. To illustrate the representation of the polar vortex in PRISM, Fig. 1b shows the amplitude development of the quasi-stationary planetary waves with zonal wavenumber $S = 1$ (PW1) and $S = 2$ (PW2) in the NAVGEM-HA and PRISM zonal winds at 48 km altitude. The wave amplitudes are calculated by least-squares fitting $S = 1$ and $S = 2$ waves to 4-day running mean zonal wind data averaged between 50-70°N.

Below 85 hPa, PRISM is nudged towards daily mean winds and temperatures calculated from 1-hourly ERA5 forecast model data. Above 0.001 hPa, the model is nudged to climatological daily mean wind and temperature fields calculated from the empirical Horizontal Wind Model version 2014 (HWM14, Drob et al., 2015) and the NRLMSISE-00 reference model (Picone et al., 2002), respectively. Diagnostic simulations where the boundaries between the different datasets used to construct the composite atmosphere are artificially smoothed, find that any discontinuities that may be present between the datasets have no impact on the simulated SDT (van Caspel et al., 2022).

2.2 Thermal Tide Forcing

The solar (thermal) SDT component is forced by incorporating hourly global temperature tendency fields (TTFs) from the ERA5 forecast model (Hersbach et al., 2020). The ERA5 TTFs include radiative and latent heating effects from the surface up to ∼80 km altitude. The ERA5 forecast model is initialized twice daily at 06:00 and 18:00 UTC based on a large observational data set, and the 12 hr segments of hourly data following each initialization are used to construct a continuous dataset of TTFs. While the ERA5 TTFs extend only up to ∼80 km altitude, the contribution to the net simulated SDT by the tide forced above this altitude is only on the order of a few ms^{-1} in the MLT (van Caspel et al., 2022).

One shortcoming of the ERA5 TTFs is that the radiative transfer model used to calculate the heating rates does not include interactive ozone chemistry. Heating by stratospheric ozone is instead calculated based on a climatological zonal mean specification (ECMWF, 2020). The ERA5 TTFs can therefore not be used to capture the impact of the SSW-induced redistribution of stratospheric ozone on the solar SDT forcing. The impact of this effect is shown to be small, however, by means of a numerical experiments using TTFs from the Specified Dynamics Whole Atmosphere Community Climate Model with Thermosphere Extension version 2.1 (SD-WACCMX, H.-L. Liu et al., 2018) in Section 4.2.1.

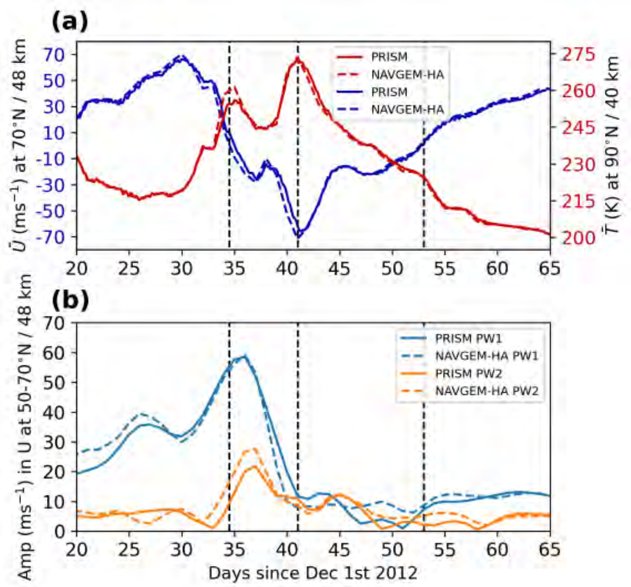

Figure 1. Panel **(a)** shows the time development of PVW as simulated by PRISM (solid lines) and by the assimilated NAVGEM-HA model (dotted lines). Panel **(b)** shows the time development of the PW1 and PW2 amplitudes in the zonal wind at 48 km altitude averaged between 50-70°N. The vertical dashed lines mark the SSW onset, peak PVW, and recovery phase as defined in Section 2.1.

The employed SD-WACCMX TTFs are the same as those described in van Caspel et al. (2022), and extend from the surface up to the thermosphere. While SD-WACCMX TTFs do include interactive ozone chemistry, diagnostic simulations nevertheless find that the short-term variability of the solar SDT forcing is better described by the ERA5 forecast model than by SD-WACCMX.

2.3 Lunar Tide Forcing

Following the approach of Pedatella et al. (2012), the lunar M_2 (12.42 hr) and N_2 (12.66 hr) SDT components are forced by prescribing an additional momentum forcing, arising from the horizontal gradient of the lunar tidal potentials. Following the notation of Pedatella et al. (2012), the tidal potential is described by its contributions from the lunar gravitational potentials (Ω), the ocean, load, and solid Earth tide vertical displacements ($g\zeta$, where $g = 9.81$ ms^{-1} and ζ is the vertical displacement in meters), and the contributions arising from the tidally induced redistribution of solid Earth mass (Ω^e). The potential perturbation arising from the tidally induced redistribution of ocean mass represents only a very minor contribution to the net tidal potential (Vial & Forbes, 1994), and is ignored in this work.

The gravitational lunar potentials are described by

$$\begin{aligned}\Omega_{M_2} &= -0.7933 P_2^2(\theta)\cos(2\tau)\\ \Omega_{N_2} &= -0.1518 P_2^2(\theta)\cos(2\tau - s + p)\end{aligned}$$

in units of $\mathrm{m^2s^{-2}}$, where $P_2^2(\theta) = 3\sin^2\theta$ is an associated Legendre polynomial and θ is co-latitude (Chapman & Lindzen, 1970). In the above time factors, $\tau = t + h - s$ where h, s, and p are given by

$$\begin{aligned} h &= 279.69668 + 36000.76892T + 0.00030T^2 \\ s &= -270.43659 + 481267.89057T + 0.00198T^2 \\ p &= 334.32956 + 4069.03403T - 0.01032T^2 - 0.00001T^3 \end{aligned}$$

in units of degrees, T represents the time since Greenwich mean noon on 1899 December 31 in units of a Julian century (36525 days), and t is the angular measure of mean solar time ($15° = 1$ hr). The M_2 potential describes the classical double tidal bulge, whereas the N_2 potential describes the $\sim 20\%$ variations of the M_2 potential caused by the ellipticity of the lunar orbit.

The Earth tide accounts for the vertical displacement of the Earth's crust in response to the lunar gravitational potentials. The Earth tide is also accompanied by a geopotential perturbation arising from the associated redistribution of crustal mass. Both the Earth tide and the associated mass-redistribution potentials can be expressed as Love-number multiplications of the lunar gravitational potentials, where the Love numbers are given by $h_2 = -0.609$ and $k_2 = 0.302$, respectively (Hollingsworth, 1971). The Earth tide potential can then be written as $(\zeta^e_{M_2} + \zeta^e_{N_2})g = h_2(\Omega_{M_2} + \Omega_{N_2})$, and the associated mass-redistribution potential as $\Omega^e_{M_2} + \Omega^e_{N_2} = k_2(\Omega_{M_2} + \Omega_{N_2})$.

To force the lunar ocean and load tidal components in PRISM, hourly M_2 and N_2 elevation fields from the FES2014 ocean tide atlas are incorporated. The FES2014 model combines the hydrodynamic modeling of the ocean tides with ensemble data assimilation techniques, providing global instantaneous ocean and load tide elevation fields (Lyard et al., 2021). The load tide represents the vertical displacement of the ocean crust in response to the loading by the ocean tides.

To demonstrate the efficacy of the lunar tide implementation, climatological migrating lunar SDT (lunar SW2, for Semidiurnal, Westward S = 2) simulations are compared against those simulated by the Global Scale Wave Model (GSWM) and the Whole-Atmosphere Community Climate Model (WACCM), as described in detail by Pedatella et al. (2012). For the PRISM simulation, the lunar tide forcing for the year 2013 is propagated through a climatological background atmosphere based on monthly mean zonal mean zonal winds and temperatures from the upper atmosphere research satellite (UARS) reference atmosphere project (URAP, Swinbank & Ortland, 2003). The URAP atmosphere extends from the surface up to ∼110 km altitude, and is padded to HWM14 and MSISE-00 fields for altitudes above 110 km. No thermal forcing is included in the PRISM lunar validation simulation, such that the amplitude of the lunar SW2 can easily be extracted using 2-D Fourier analysis. Fig. 2 shows the simulated January and June mean lunar SW2 amplitudes in the zonal wind. The vertical and latitudinal structure of the lunar SW2 is in close correspondence with those simulated by the GSWM and WACCM models, as shown in Pedatella et al. (2012), with peak amplitudes in the summer hemisphere between 40-50° around 110-125 km altitude. We note that, while Pedatella et al. (2012) finds that the GSWM amplitudes are a factor of 2-3 greater than those simulated by the WACCM, the magnitude of the PRISM amplitudes are in close agreement with those of the GSWM. For example, peak amplitudes in January are around 18 $\mathrm{ms^{-1}}$ in PRISM, 8 $\mathrm{ms^{-1}}$ in WACCM, and 22 $\mathrm{ms^{-1}}$ in the GSWM.

3 Model Validation and Comparison

In this section, the net simulated SDT response is validated against the local SDT measured at the CMOR, Collm, and Kiruna meteor radar stations, and against the migrating SDT measured by the SuperDARN meteor radars. In addition, the relative importance of the solar and lunar SDT components is investigated by comparing individ-

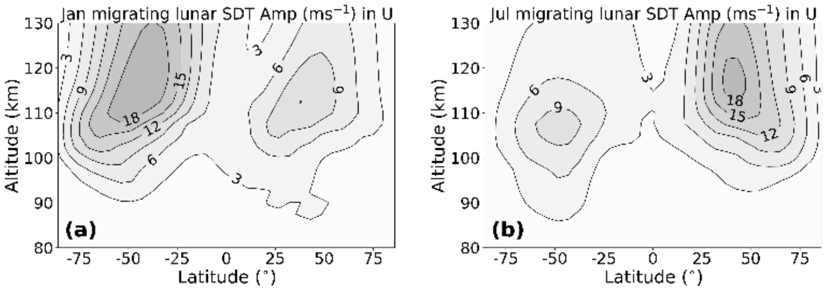

Figure 2. Monthly mean lunar SW2 amplitude in the zonal wind simulated by the PRISM lunar validation simulation for January **(a)** and July **(b)** conditions.

Table 1. Numerical experiment design.

Experiment	Configuration
PRISM	Standard model configuration (see section 2)
OnlyLunar	As PRISM, includes only lunar tide forcing
OnlySolar	As PRISM, includes only solar (thermal) tide forcing
PRISM-SDARN	As PRISM, model sampled using SuperDARN observational filter
OnlyLunar-SDARN	As OnlyLunar, model sampled using SuperDARN observational filter
OnlySolar-SDARN	As OnlySolar, model sampled using SuperDARN observational filter

ual lunar and solar SDT simulations against the net simulated and observed SDT variability. The simulations performed in this section are listed in Table 1, which will be discussed in more detail in the text. Furthermore, the results presented here are found to be similar between the zonal and meridional wind components, and therefore only the zonal component is considered throughout the following.

3.1 Local Meteor Radar SDT Response

The PRISM simulation results are first compared against the net local SDT measurements made by the Collm (51.3°N,13.0°E), CMOR (43.3°N,80.8°W), and Kiruna (67.9°N,21.1°E) meteor radars. These radars provide hourly horizontal winds by measuring so-called meteor position data (Hocking et al., 2001), while details of the aforementioned radars are given in Stober et al. (2021). The wind measurements used in this study span the 85 to 97 km altitude region with a 2 km vertical spacing. To extract the SDT amplitude and phase from the hourly meteor radar winds, a least-squares 4-day sliding window fit of an offset and a 24, 12 and 8 hour sine wave representative of the mean wind and the diurnal, semidiurnal and terdiurnal tide is applied. Here the fitted SDT includes only a 12.00 hr component, which aliases the solar and lunar SDT components. To compare the model to observation, hourly PRISM output is interpolated to the geographic locations of the meteor radars, and is analyzed using the same least-squares fitting routine.

The amplitude of the SDT measured and simulated at the three radar sites is shown in Fig. 3. At the CMOR radar site (Fig. 3a and 3d), both the model and observations show a major amplitude enhancement occurring roughly 5 days after peak PVW, where amplitudes reach values of up to 70 ms^{-1}. This enhancement is preceded by a 10-day

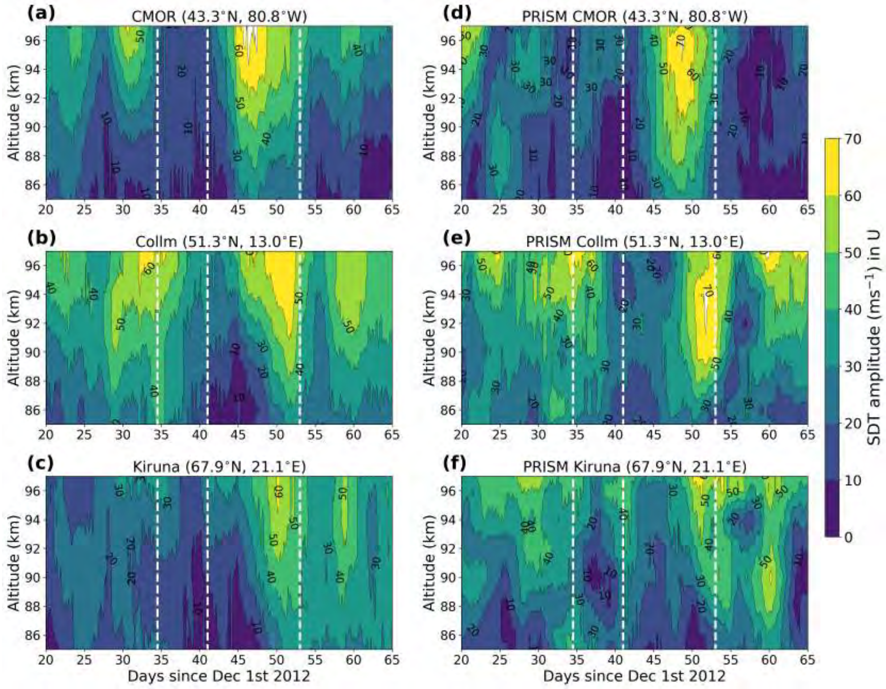

Figure 3. Comparison of the local SDT amplitude in the zonal wind measured by the meteor radars and simulated by PRISM at the CMOR **(a,d)**, Collm **(b,e)**, and Kiruna **(c,f)** radar sites. Contours are spaced in 10 ms^{-1} intervals. The vertical dashed lines mark the SSW onset, peak PVW, and recovery onset as defined in Section 2.1.

amplitude minimum, having values of around 10-20 ms^{-1}, beginning around the time of the SSW onset. The simulated SDT is underestimated by about 10-20 ms^{-1} in the period following the recovery phase onset.

At the Collm radar site (Fig. 3b and 3e), the observed and simulated SDT also show a 60-70 ms^{-1} amplitude enhancement, although here the peak amplitudes occur nearer to 10 days rather than 5 days after peak PVW. As observed at the CMOR radar site, the SDT enhancement is preceded by a roughly 10-day amplitude minimum. In addition, a quasi 10-day periodicity is clearly distinguishable in both the observed and simulated amplitudes, reaching local amplitude maxima around days 23, 34, 50, and 60. This periodicity is also discernible at the CMOR site, and to a lesser extent also at the Kiruna site. At the Kiruna radar site (Fig. 3c and 3f), the simulated and observed SDT shows behavior similar to that of Collm, reaching peak amplitudes around 10 days after peak PVW preceded by a 10 day amplitude minimum. However, for the Kiruna site the model shows more variability in the vertical compared to observation, and overestimates amplitudes by around 20 ms $^{-1}$ between days 20 and 40. Over the course of the SSW, the observed tidal amplitude variability is nevertheless convincingly reproduced by the PRISM model at all three radar sites. We note that the SDT amplitudes observed at the Trondheim meteor radar site (64.4°N,10.5°E), are of a similar magnitude as those described here for the Collm radar, displaying a similar temporal evolution (Hibbins et al., 2019). resource://pdf.js/web/images/annotation-noicon.svg

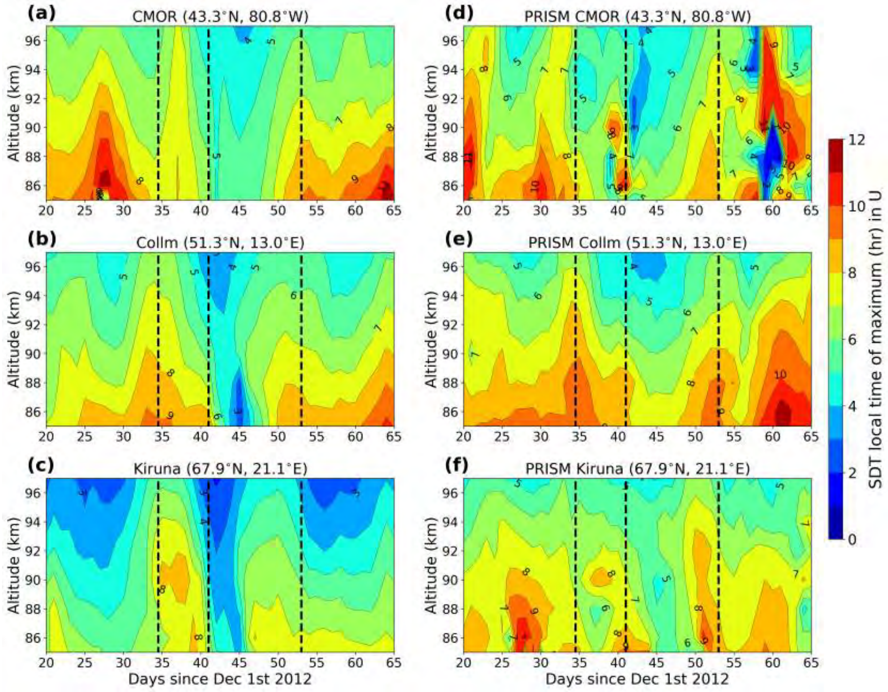

Figure 4. Comparison of the SDT phase (LTOM) in the zonal wind simulated by PRISM and measured by the meteor radars at the CMOR **(a,d)**, Collm **(b,e)**, and Kiruna **(c,f)** radar sites. Contours are spaced in 1 hr intervals. The vertical dashed lines mark the SSW onset, peak PVW, and recovery onset as defined in Section 2.1.

Fig. 4 shows the phase of the simulated and observed SDT at the three radar sites, expressed here in terms of the local time of maximum (LTOM). The local time at each radar site is calculated as $t_{local} = t_{UTC} + 24 \cdot \lambda/360$, where λ is the station longitude in degrees. The observed phase displays similar characteristics at all three radar sites, where the LTOM shifts to an earlier time by about 3-4 hr over the course of a 5-day period following peak PVW. While this behavior is reproduced by the model, the simulated phase shift is nearer to 2-3 hr rather than 3-4 hr. Moreover, the simulated phase at the Kiruna site is overestimated by about 2 hrs on average, while the phase at the CMOR site displays more variability between day 50 and 65.

3.2 Solar and Lunar Meteor Radar SDT Response

The previous section established that the simulated SDT at the CMOR, Collm, and Kiruna meteor radar sites is in good agreement with observation. This gives confidence in that PRISM realistically describes the mechanisms controlling the different sources of SDT variability at these radar sites. Leveraging this result, numerical experiments are performed to assess the individual contributions of the lunar and solar SDT components to the net simulated SDT. This is achieved by performing simulations where only the lunar SDT forcing components (OnlyLunar) or only the thermal forcing component (OnlySolar) are included, as shown in Table 1. Here we note that in the following, the sum of the OnlySolar and OnlyLunar experiments closely resembles that of the full PRISM sim-

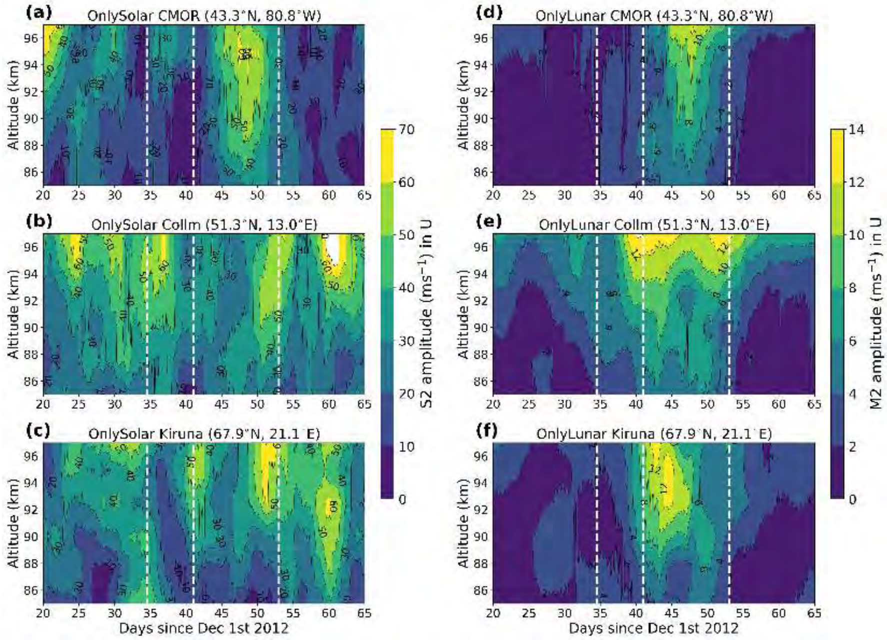

Figure 5. Comparison of the zonal local SDT amplitude simulated by the OnlySolar and OnlyLunar experiments at the CMOR **(a,d)**, Collm **(b,e)**, and Kiruna **(c,f)** radar sites. Contours are spaced in 10 ms^{-1} intervals. Note the different color scaling for the left-hand and right-hand panels. The vertical dashed lines mark the SSW onset, peak PVW, and recovery onset as defined in Section 2.1.

ulation, which indicates that non-linear interactions between the solar and lunar tides are of minor importance. However, each of the simulations performed in the following contains some degree of background SDT amplitude variability on the order of a few ms^{-1}, which we attribute to internal variability caused by gravity waves.

Fig. 5 compares the simulated solar and lunar SDT amplitudes at the CMOR, Collm, and Kiruna meteor radar sites. Here the tidal amplitudes are calculated using the same 4-day sliding window method as before, but in the least-squares fit to the OnlyLunar simulation the 12 hr wave has been replaced by a 12.42 hr wave instead. Fig. 5a-c shows that the simulated solar SDT closely resembles that of the full PRISM simulation (as shown in Fig. 3d-f). The most notable differences are that the amplitude enhancements following peak PVW are about 5-10 ms^{-1} smaller, while the amplitude minima preceding the enhancements are about 5-10 ms^{-1} less deep.

Fig. 5d-f shows that the lunar SDT enhances broadly between peak PVW and the recovery onset, reaching amplitudes between 12-14 ms^{-1} at all three radar sites. At the time of the solar SDT enhancement following peak PVW, the lunar SDT amplitudes are nevertheless only about 15-20% of that of the solar SDT. Similarly, diagnostic analysis finds that the phase variations of the net SDT is almost entirely attributable to that of the solar SDT over the course of the SSW.

3.3 SuperDARN Migrating SDT Response

Whereas the previous simulations were compared against single station observations that measure the net sum of all the SDT components in the wind field, here the PRISM simulation results are compared specifically against the migrating semidiurnal (SW2) tide derived from a mid- to high-latitude array of 10 SuperDARN meteor radars. The SuperDARN radars are the same as those used in earlier works to measure and simulate the seasonal variations of the SW2 tide in the MLT (van Caspel et al., 2022, 2020). The SuperDARN radars span 180° of longitude around a 14° latitude band centered on 60°N, and their time-synchronized hourly horizontal wind measurements can be used to unambiguously separate the mid- to high-latitude migrating tidal components. While a detailed description of the SuperDARN measurement and model sampling technique are given by van Caspel et al. (2022) and van Caspel et al. (2020), a brief description is included here.

The SuperDARN meteor echo distribution is approximately a Gaussian centered on 100 km altitude with a Full Width at Half Maximum (FWHM) of 30 km (Chisham, 2018; Chisham & Freeman, 2013). To compare PRISM to SuperDARN, hourly model output is first sampled at the locations of available SuperDARN measurements. A vertical averaging kernel representing the SuperDARN meteor echo distribution (the 'observational filter') is then applied to the sampled model winds. After sampling and vertically averaging, the model winds are referred to as PRISM-SDARN. The PRISM-SDARN winds are then analyzed using the same method used to analyze the hourly SuperDARN winds, by least-squares fitting a wave surface representing the migrating diurnal, semidiurnal, and terdiurnal tide, including a mean wind, over a 4-day sliding window in both space and time. For the observed SW2 tide, uncertainties on the fitted tidal parameters are estimated by taking into account the standard deviations of the hourly wind observations. In the following, the corresponding 'SuperDARN sampled' OnlySolar and OnlyLunar simulations are referred to as OnlySolar-SDARN and OnlyLunar-SDARN. In the migrating tidal fit to the OnlyLunar-SDARN winds, the 12 hr SW2 wave is replaced by a 12.42 hr SW2 wave.

Fig. 6a compares the observed SW2 amplitudes against those simulated by PRISM-SDARN and by the corresponding OnlySolar-SDARN and OnlyLunar-SDARN experiments. One of the notable features of the observed SW2 tide, is that it shows a pronounced low-frequency amplitude modulation with local amplitude maxima around day 34, 48, and 60. PRISM-SDARN reproduces this modulation, even though the simulated local amplitude maximum on day 48 (60) is around 3 days earlier (later) than what is observed. In contrast, the local amplitude maxima on days 48 and 60 are absent in the OnlySolar-SDARN simulation, while the amplitude maximum on day 34 is smaller than what is observed. The presence of the lunar SW2 component in the PRISM simulation therefore improves the comparison with the oscillatory features of the amplitude data, even though there remain discrepancies in the magnitude and period of this oscillatory component. As shown by the OnlyLunar-SDARN simulation, the lunar SW2 amplitudes reach a maximum nearly coincident with peak PVW. This suggest that the low-frequency amplitude modulation in PRISM-SDARN is partly due to the quasi 15-day beating between the solar and lunar SW2 tides, which will be discussed in more detail in Section 4.3.

The tidal phases shown in Fig. 6b demonstrate that PRISM-SDARN underestimates the observed LTOM by about 3 hrs on average. The observed temporal evolution of the phase is nevertheless qualitatively reproduced, with the phase reaching its earliest LTOM shortly after peak PVW. The close agreement between the phase of the OnlySolar-SDARN and PRISM-SDARN simulations, shows that the phase variations of the net SW2 are almost entirely attributable to that of the solar SW2 component.

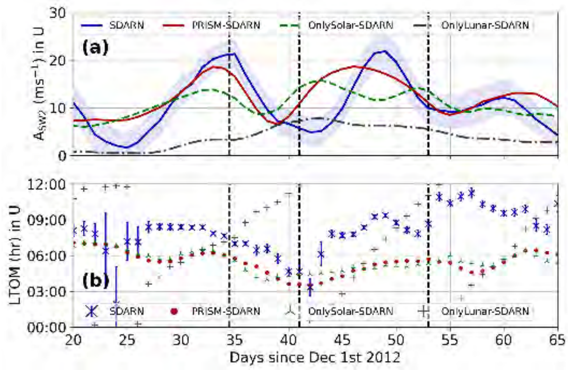

Figure 6. Comparison of the amplitude **(a)** and phase **(b)** of the zonal SW2 tide observed by SuperDARN (blue, SDARN), simulated by PRISM-SDARN (red), and simulated by the OnlySolar-SDARN (green) and OnlyLunar-SDARN (grey) numerical experiments. The shading and error bars represent the 2σ fitting uncertainties on the SuperDARN measurements. The vertical dashed lines mark the SSW onset, peak PVW, and recovery onset as defined in Section 2.1.

Table 2. Mechanism analysis numerical experiment design.

Experiment	Configuration
FixedAtmos	As OnlySolar (see Table 1), atmosphere fixed to zonal mean Dec 20th 2012
FixedForcing	As OnlySolar, forcing includes only SW2 fixed to Dec 20th 2012
WACStrat	As OnlySolar, forcing only between 100-0.1 hPa based on SD-WACCMX
Lunarshift-SDARN	As OnlyLunar-SDARN, lunar phase shifted forward by 7.5 solar days

4 Model Analysis

In this section, the model output is investigated in more detail to gain insight into the driving mechanisms of the simulation results. To this end, the simulated SDT is first decomposed into its migrating and non-migrating components. The mechanisms driving the variability of these tidal components is then investigated in more detail by means of numerical experiments. These experiments identify the individual effects of the changing propagation conditions through the background atmosphere, non-linear wave-wave interactions between the SW2 tide and quasi-stationary planetary waves, and variations in the tidal forcing caused by the stratospheric ozone perturbation. In addition, the impact of the age of the moon (lunar phase) on the PRISM-SDARN simulation result is investigated in an experiment where the lunar phase is artificially shifted forward by 7.5 solar days. An overview of the numerical experiments of this section is given in Table 2.

4.1 Migrating and Non-Migrating SDT Response

The migrating and non-migrating SDT components are calculated by performing a 2-D Fourier decomposition of the simulated zonal wind field, where a 4-day sliding window is employed. Diagnostic analysis finds that the two largest non-migrating SDT components are the westward zonal wavenumber S = 1 (SW1) and westward zonal wavenumber S = 3 (SW3) tides. Other non-migrating SDT components are therefore not considered in the following.

Fig. 7a-c shows the SW2, SW1, and SW3 tides in the PRISM simulation at 97 km altitude, which corresponds to the highest altitude of the Collm, CMOR, and Kiruna meteor radar measurements discussed in Section 3.1. This figure illustrates that the largest amplitudes in the Northern Hemisphere occur in the SW2 component. A notable feature is that the SW2 amplitudes are reduced by 20-30 ms^{-1} over the course of a 10-day period centered roughly on the day of peak PVW. Furthermore, while the SW2 tide generally peaks between 50-70°N, its amplitude is increased between 30-45°N roughly between day 43 and 48, corresponding to the latitude band where the CMOR radar is located (43.3°N). Amplitudes nevertheless stay below 45 ms^{-1} at all latitudes up until day 60. The simulated net SDT amplitude enhancement up to 70 ms^{-1} at the three meteor radar sites, as discussed in Section 3, is therefore strongly dependent on the contributions of constructively interfering non-migrating SDT components. For example, non-migrating tides contribute close to 50% of the net simulated SDT amplitude at the CMOR radar site during its enhancement around day 47. The SW1 tide achieves its highest amplitudes between peak PVW and the recovery phase onset, reaching amplitudes up to 27 ms^{-1}. The largest SW1 tide amplitudes are, however, constrained to the high-latitudes. For the SW3 tide, amplitudes intermittently reach values between 10-20 ms^{-1} both before a, after, and during the SSW. A clear SW3 tide response to the SSW is therefore not readily discernible in the PRISM simulation. Fig. 7d-f shows the latitude-time development of the SW2, SW1, and SW3 tides from the OnlySolar simulations. These panels illustrate that the migrating and non-migrating SDTs in PRISM can be largely attributed to the solar SDT component, consistent with the results described in Section 3.

Fig. 8 shows the altitude-time development of the SW2 amplitudes at 60°N from the PRISM, OnlySolar, and OnlyLunar simulations. While 60°N corresponds to the central latitude of the SuperDARN radar stations, the shown altitude-time behavior is nevertheless representative of that across the mid- and high-latitudes. Here we note that, consistent with the results for the solar SW2 tide, diagnostic analysis finds that the largest amplitudes for the lunar SW2 tide also occur in its migrating component.

Fig. 8a shows that the PRISM SW2 amplitudes enhance between 105-130 km altitude for a 10-day period following peak PVW, coincident with an amplitude decrease below these altitudes. Note that the reduced amplitudes below 105 km altitude are also expressed in Fig. 7a. Fig. 8b shows that the altitude-time structure of the solar SW2 tide closely follows that of the net SW2 simulated by PRISM. The largest differences occur in the peak amplitudes between 105-130 km altitude around day 50 and 63, which are about 20 ms^{-1} smaller in the OnlySolar simulation.

The difference between the PRISM and OnlySolar simulations between 105-130 km altitude can be attributed to the presence of an enhanced lunar SW2 tide, which is shown to occur in the OnlyLunar simulation in Fig. 8c. The lunar SW2 reaches amplitudes of 22-24 ms^{-1} around 115 km altitude for a roughly 20-day period following peak PVW. During this time, and between 105-130 km altitude, the lunar SW2 amplitudes are around 35-40% of that of the solar SW2 tide. Furthermore, diagnostic simulations where the N_2 forcing is not included find that the 15-day amplitude variations in the OnlyLunar simulation are caused by the presence of the N_2 tide (i.e., by the variations in the lunar tide forcing caused by the ellipticity of the lunar orbit). Furthermore, diagnostic simulations wherein planetary waves are suppressed, find that the altitude-time development for the solar and lunar SW2 components in Fig. 8 is almost entirely due to the changing propagation conditions through the (zonal mean) background atmosphere.

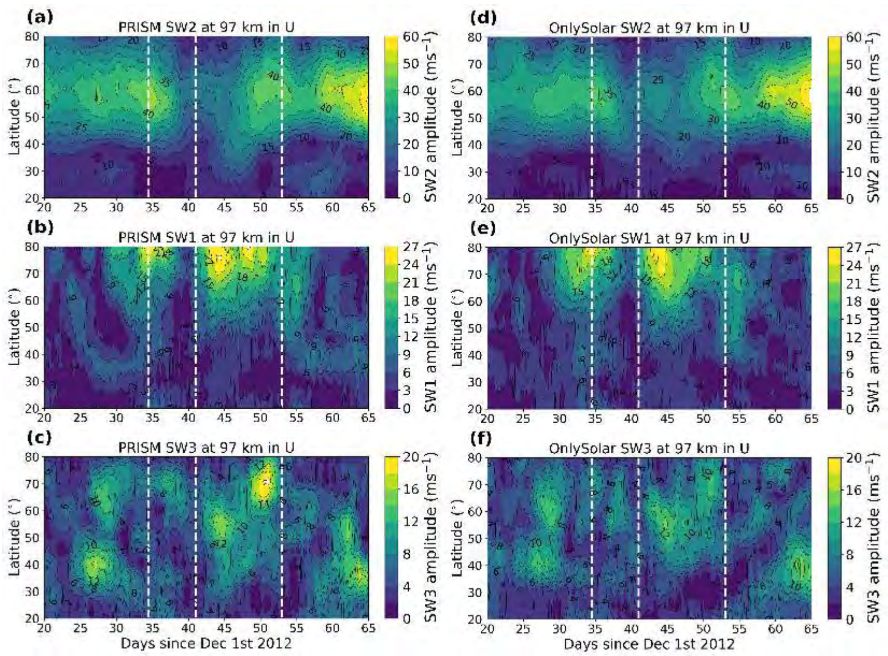

Figure 7. Latitude-time development of the SW2, SW1, and SW3 amplitude at 97 km altitude in the zonal wind for the PRISM **(a,b,c)** simulation and the OnlySolar **(d,e,f)** numerical experiment listed in Table 2. The vertical dashed lines mark the SSW onset, peak PVW, and recovery onset as defined in Section 2.1. Note the different colour bar scaling for the different tidal components.

4.2 Response Mechanisms

Numerical experiments are performed to identify the individual impact of the changing propagation conditions through the background atmosphere, non-linear wave-wave interactions between the SW2 tide and quasi-stationary planetary waves, and changes to the tidal forcing brought about by the stratospheric ozone perturbation. For this, only the solar SDT is considered, since the previous section established that the majority of the SDT variability is driven by the solar component.

Fig. 9a-c shows the latitude-time development of the SW2, SW1, and SW3 tides at 97 km altitude for the FixedForcing experiment, corresponding to the altitude shown in Fig. 7. In the FixedForcing experiment only the SW2 component of the thermal forcing is included, fixed to that of the 20th of December 2012. Since the forcing includes no non-migrating tides, the presence of any SW1 and SW3 tides can therefore be attributed to being the product of non-linear wave-wave interactions. The resulting SW2 tide shown in Fig. 9a shows similar characteristics to that of the OnlySolar simulation (as shown in Fig. 7d), with a 10-day amplitude minimum broadly around the time peak PVW. The SW1 tide shown in Fig. 9b also closely corresponds to that of the OnlySolar simulation, reaching peak amplitudes up to 24 ms^{-1}. For the SW3 tide shown in Fig. 9c, the FixedForcing experiment identifies a pronounced non-linear wave-wave forcing occurring around day 45 between 50-60°N, with the resulting SW3 tide reaching amplitudes of up to 18 ms^{-1}.

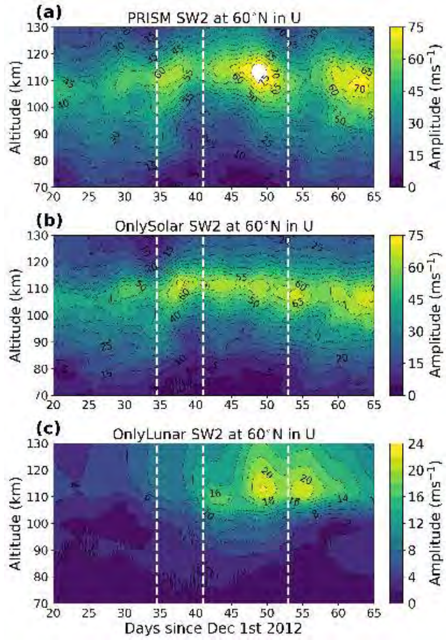

Figure 8. Altitude-time development of the SW2 tidal amplitude in the zonal wind at 60°N for the PRISM **(a)**, OnlySolar **(b)**, and OnlyLunar **(c)** simulations. The vertical dashed lines mark the SSW onset, peak PVW, and recovery onset as defined in Section 2.1. Note the different colour bar scaling in panel **c**.

Fig. 9d-f shows the latitude-time development of the SW2, SW1, and SW3 tides for the FixedAtmos experiments. In the FixedAtmos experiment the full thermal forcing is included, while the atmosphere is fixed to that of the 20th of December 2012. In addition, no planetary waves are included in this simulation, such that any variations in the non-migrating tides is attributable to variations in the thermal forcing of these tidal components. A striking feature of the resulting SW2 tide is that it shows quasi 10-day variations on the order of 10-20 ms^{-1}, which are also expressed in the PRISM and OnlySolar simulations at the CMOR, Collm, and Kiruna meteor radar sites (as discussed in Section 3). Fig. 9e shows that the thermal forcing component of the SW1 tide is considerably smaller than the wave-wave forcing component, and that it shows no readily discernible response to the SSW. The SW3 tide is frequently excited by thermal heating, reaching amplitudes up to 12 ms^{-1} in the mid- and high-latitudes. Since the thermal variations of the SW3 tide are similar in magnitude to those produced by the wave-wave forcing, the wave-wave forcing response is effectively ‘masked’ by the thermally excited SW3 tide in the OnlySolar and PRISM simulations. Here we note that, since the employed ERA5 temperature tendencies do not include interactive ozone and extend only up to ∼80 km altitude, the variations in the thermal forcing described here can be attributed to variations in the tropospheric forcing component.

4.2.1 Ozone Forcing

As discussed in Section 2, the employed ERA5 TTFs in the PRISM simulation do not include interactive ozone chemistry. The ERA5 TTFs can therefore not be used to

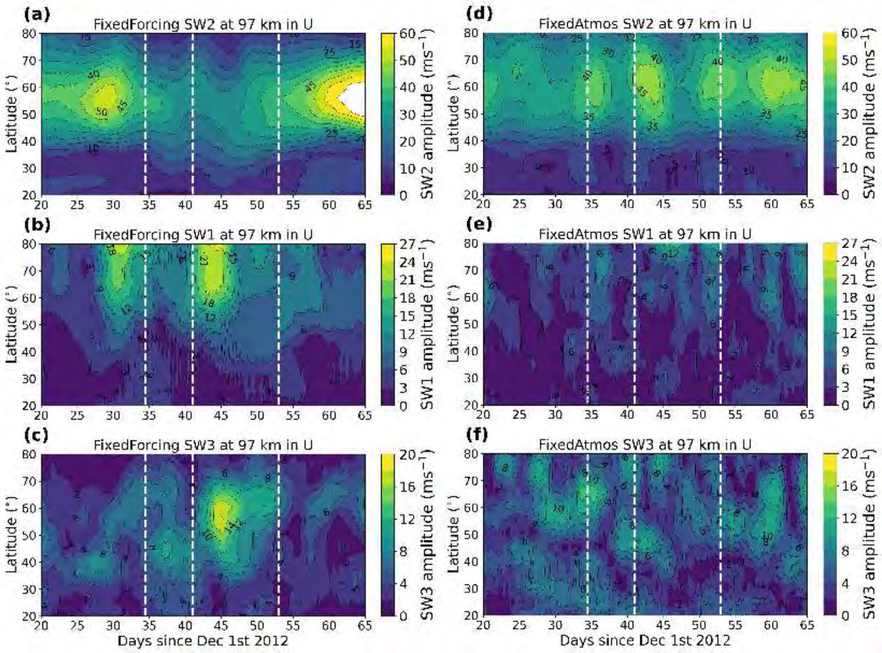

Figure 9. Latitude-time development of the SW2, SW1, and SW3 amplitude at 97 km altitude in the zonal wind for the FixedForcing **(a,b,c)** and FixedAtmos **(d,e,f)** numerical experiments listed in Table 2. The vertical dashed lines mark the SSW onset, peak PVW, and recovery onset as defined in Section 2.1. Note the different colour bar scaling for the different tidal components.

describe changes in the SDT forcing caused by the SSW-induced redistribution of (equatorial) stratospheric ozone. To investigate the impact of this effect, a simulation is performed using 3-hourly TTFs from the SD-WACCMX model. The SD-WACCMX model *does* include interactive ozone chemistry, while also capturing the dynamics of the 2013 SSW by virtue of its assimilated MERRA-2 reanalysis winds and temperatures (Siskind et al., 2021).

To isolate the effects of stratospheric ozone, the WACStrat experiment includes only the SD-WACCMX TTFs forcing between 100-0.1 hPa (10-70 km altitude), which captures the entire stratospheric ozone forcing altitude region (van Caspel et al., 2022). As for the FixedAtmos experiment, the background atmosphere in the WACStrat experiment is fixed to that of the 20th of December 2013 and includes no planetary waves in the winds and temperatures. Any variations in the migrating and non-migrating tides can therefore be attributed to variations in the stratospheric ozone forcing itself.

In Fig. 10a the distribution of stratospheric ozone at 40 km altitude in SD-WACCMX is illustrated on the day of peak PVW. Here a clear zonal wavenumber S = 1 structure is present in the ozone mixing ratios around 40°N, which can be ascribed to the zonally asymmetric transport of ozone in response to the SSW. Fig. 10b, c, and d show the resulting SW1, SW2, and SW3 tidal amplitudes at 97 km altitude. These panels illustrate that the ozone-induced variations in the migrating and non-migrating tidal forcing results in amplitude variations only on order of a few ms^{-1}. The amplitude of the SW2 forcing response is decreased by 3-4 ms^{-1} about 5 days after peak PVW, while the SW1 component peaks at 2 ms^{-1} at 65°N 5 days before peak PVW. The largest variations occur in the SW3 component, which reaches amplitudes up to 4-5 ms^{-1} five days before peak PVW at 50°N. These SW3 amplitude variations are nevertheless considerably smaller than those induced by wave-wave interactions and by the variations in the tropospheric thermal forcing component, as described in the previous section.

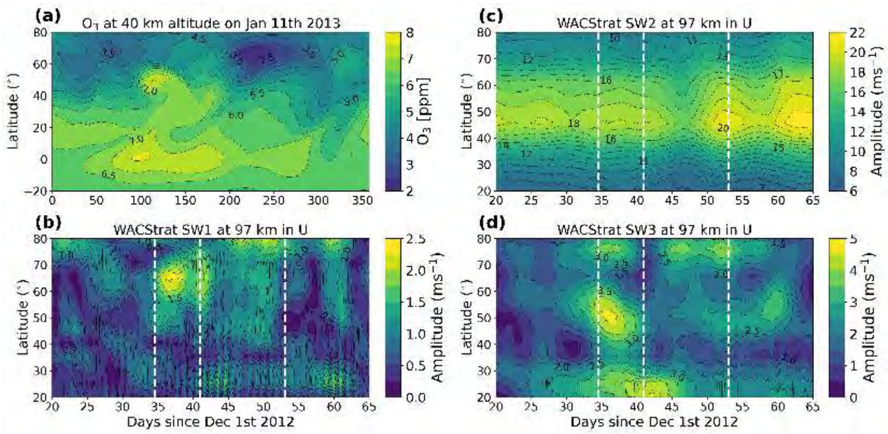

Figure 10. SD-WACCMX ozone mixing ratios at 40 km altitude on the 11th of January 2013 **(a)**, and the latitude-time development of the amplitude of the SW1 **(b)**, SW2 **(c)**, and SW3 **(d)** tidal components at 97 km altitude as simulated by the WACStrat experiment (see Table 2). The vertical dashed lines mark the SSW onset, peak PVW, and recovery onset as defined in Section 2.1. Note the differences in colour bar scaling for each of the panels.

4.3 Lunar Phase Dependence

In Section 3.3, the presence of the lunar SW2 tide was found to improve the model performance relative to observation. The presence of the enhanced lunar SW2 tide was found to magnify the 15-day beating pattern between the solar and lunar SW2 tidal components, which expresses itself as a quasi 15-day modulation of the net ('aliased') SW2 amplitude (e.g., Maute et al., 2016). The phase of this beating pattern depends on the relative phase between the solar and lunar tidal components, which suggests that the net simulated SW2 tide also depends on the lunar phase at the time of the SSW. This is illustrated in Fig. 11, which compares the LunarShift-SDARN experiment against observation, and against the PRISM-SDARN and OnlySolar-SDARN simulations. In the LunarShift-SDARN experiment, the model configuration is the same as for PRISM-SDARN, but here the age of the moon has been shifted forward by 7.5 solar days, or by one quarter of a lunar cycle. Fig. 11 illustrates that the impact of the lunar phase shift is to also shift the phase of the solar-lunar beating pattern forward by half a cycle. Consequently, the resulting peaks and troughs of the net SW2 amplitude in the LunarShift-SDARN experiment are almost exactly out of phase with those from PRISM-SDARN and observation. By comparison to the OnlySolar-SDARN simulation, the presence of the phase-shifted lunar tide in the LunarShift-SDARN simulation can also be seen to make the simulation results worse, rather than better, relative to observation. For example, the smaller amplitudes in the LunarShift-SDARN than in the OnlySolar-SDARN simulation around days 33, 47, and 60, represents deviations away from observation.

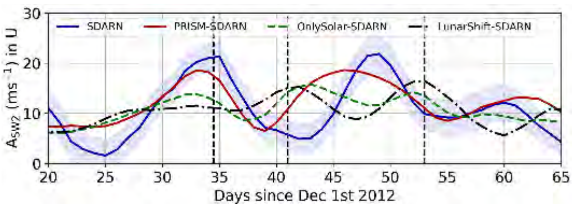

Figure 11. Comparison of the zonal SW2 tidal amplitude observed by SuperDARN (blue, SDARN), simulated by PRISM-SDARN (red), and simulated by the OnlySolar-SDARN (green) and LunarShift-SDARN (black) numerical experiments. The shading and error bars represent the 2σ fitting uncertainties on the SuperDARN measurements. The vertical dashed lines mark the SSW onset, peak PVW, and recovery onset as defined in Section 2.1.

5 Discussion and Conclusion

This study presents a detailed investigation of the SDT response to the 2013 SSW, using a range of Northern Hemisphere mid- and high-latitude meteor wind observations and mechanistic tidal model simulations. The net simulated SDT response compares favourably with measurements at the CMOR (43.3°N, 80.8°W), Collm (51.3°N, 13.0°E), and Kiruna (67.5°N, 20.1°E) meteor radars, and with SW2 tide observations made by a longitudinal array of SuperDARN radars. The simulated SDT response is investigated by decomposing the forcing into its individual lunar and solar SDT components, and by decomposing the model output into its migrating and non-migrating SDT components. Detailed numerical experiments investigate the relative importance of the changing propagation conditions through the background atmosphere, non-linear wave-wave interactions between the SW2 tide and quasi-stationary planetary waves, and changes to the tidal forcing brought about by the stratospheric ozone perturbation. For the latter, the impact on the net simulated tide is found to be comparatively insignificant, leading to amplitude perturbations only on the order of 2-5 ms^{-1} around 97 km altitude.

The Collm, CMOR, and Kiruna meteor radars are used to assess the changes in the SDT over the course of the 2013 SSW between 85 and 97 km altitude. Within this altitude region the observed SDT shows a marked 10-day amplitude minimum centered roughly on the day of peak PVW, followed by a major and rapid enhancement over the course of ~5 days. The observed tidal phases show a 3-4 hr advancement over the course of a ~5 day period following peak PVW. Individual simulations of the solar and lunar SDT components at the aforementioned radar sites, find that the net simulated SDT response can be almost entirely attributed to that of the solar SDT component. During the major amplitude enhancement, lunar SDT amplitudes are only around 15-20% of that of the solar SDT within the altitude range of the three meteor radars. The solar SDT response itself is found to be driven by the changing propagation conditions through the background atmosphere, and by non-linear wave-wave interactions between its migrating component and quasi-stationary planetary waves. The non-migrating tides generated by the latter mechanism contribute up to 50% of the net SDT amplitudes simulated at the meteor radar sites.

The 10-day amplitude minimum preceding the amplitude enhancement coincides with a decrease of simulated SW2 tidal amplitudes for altitudes below 105 km, driven by changing tidal propagation conditions through the background atmosphere. This is furthermore coincident with an amplitude increase between 105-130 km altitude, where the lunar SW2 tidal component is also found to enhance more strongly. Between 105-130 km altitude, simulated lunar SW2 amplitudes can reach up to 35-40% of that of the solar SW2. These enhanced lunar SW2 amplitudes are also expressed in the PRISM-SDARN simulation, whose vertical averaging kernel follows the SuperDARN meteor echo distribution and extends up to 125 km altitude. Here the model is considerably improved when the lunar SDT forcing is included, which establishes a quasi 15-day beating pattern between the solar and lunar SW2 components that is in broad agreement with the observed amplitude variations.

In our simulations, the minimal role of the lunar SDT below 105 km altitude contrasts earlier reports of a strongly enhanced lunar SDT below this altitude (Conte et al., 2017; Chau et al., 2015). We suggest that at least some of this discrepancy can be attributed to the challenges of separating the solar and lunar SDT components from a single time series. To illustrate this complication, the commonly used method of applying a 16-day sliding window fit containing both the 12.00 hr (solar) and 12.42 hr (lunar) SDT components is demonstrated. Fig. 12 shows the resulting solar and lunar SDT amplitudes simulated and observed at the CMOR radar site. While the resulting variations in the lunar and solar SDT amplitudes qualitatively agree with to those described in Section 3.1, with an amplitude enhancement occurring roughly 5 days after peak PVW, large quantitative differences are introduced. For example, the resulting lunar SDT amplitudes overestimate the actual lunar SDT in PRISM by nearly 250%, while the solar SDT is underestimated by about 30%. This cross-contamination effect also occurs for simulations without a lunar tide forcing at all, as shown in the fit to the OnlySolar simulation results in Fig. 3.1c and f. Similar analysis finds that the OnlySolar simulation also yields 'cross-contaminated' lunar SDT amplitudes up to 24 and 16 ms^{-1} at the Collm and Kiruna sites, respectively. Diagnostic simulations with a fixed atmosphere furthermore find that the lunar SDT contamination is not caused by the presence of lunar periodicities in the solar forcing itself, but by variability in the solar SDT caused by the changing propagation conditions and wave-wave interactions.

In summary, this study finds that the SDT response to the 2013 major SSW is strongly dependent on altitude, latitude, longitude, and even on the lunar phase. The SDT response is predominantly driven by the solar SDT, which in turn is driven by the changing propagation conditions through the background atmosphere and by non-linear wave-wave interactions between the migrating SDT and quasi-stationary planetary waves. While the current work presents a case study for a single SSW event, the mechanisms driving the simulated SDT response are expected to vary considerably depending on the magnitude, length, and planetary-wave structure of other SSWs. Consequently, the SDT response recorded at any given location is also expected to vary considerably between different SSWs, which can complicate the climatological analysis of the SDT response at any given location. It is further demonstrated that the SSW-induced variability in the solar SDT can easily cross-contaminate attempts to observationally quantify the lunar SDT, which can cause the amplitude of the latter to be greatly overestimated.

Acknowledgments

The current research was supported by the Research Council of Norway (grant no. 223525/F50). The authors acknowledge the use of NAVGEM-HA data and SuperDARN meteor wind data. Development of NAVGEM-HA was supported by the Chief of Naval Research and the Department of Defense High Performance Computing Modernization Project. The SuperDARN project is funded by national scientific funding agencies of Australia, China, Canada, France, Japan, Italy, Norway, South Africa, the United Kingdom, and the United States.

SuperDARN data are available from https://www.frdr-dfdr.ca/repo/collection/superdarn. Hourly ERA5 model level forecast data are available through the climate data store (CDS). SD-WACCMX data are available at https://www.earthsystemgrid.org CCSM run SD-WACCM-X v2.1, Atmosphere History Data, 3-Hourly Instantaneous Values, version 7.

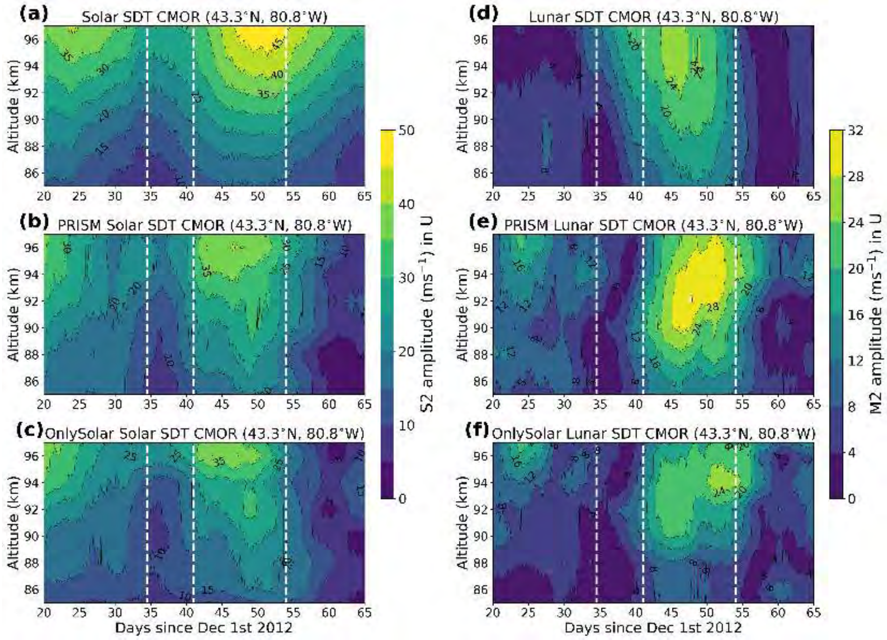

Figure 12. Solar and lunar SDT zonal amplitude extracted using a 16-day sliding window for the CMOR meteor winds **(a,d)**, PRISM simulation **(b,e)**, and OnlySolar experiment **(c,f)**. Note the different color scaling for the left-hand and right-hand panels. The vertical dashed lines mark the SSW onset, peak PVW, and recovery onset as defined in Section 2.1.

The code used to compute FES2014 was developed in collaboration between Legos, Noveltis, CLS Space Oceanography Division and CNES, and is available under GNU General Public License. The Esrange meteor radar operation, maintenance and data collection is provided by Esrange Space Center of Swedish Space Corporation.

References

Baldwin, M. P., Ayarzagüena, B., Birner, T., Butchart, N., Butler, A. H., Charlton-Perez, A. J., ... Pedatella, N. M. (2021). Sudden stratospheric warmings. *Reviews of Geophysics*, *59*(1), e2020RG000708. doi: 10.1029/2020RG000708

Chapman, S., & Lindzen, R. S. (1970). *Atmospheric tides*. Springer Netherlands. doi: https://doi.org/10.1007/978-94-010-3399-2

Chau, J. L., Hoffmann, P., Pedatella, N. M., Matthias, V., & Stober, G. (2015). Upper mesospheric lunar tides over middle and high latitudes during sudden stratospheric warming events. *Journal of Geophysical Research: Space Physics*, *120*(4), 3084-3096. doi: 10.1002/2015JA020998

Chisham, G. (2018). Calibrating SuperDARN interferometers using meteor backscatter. *Radio Science*, *53*(6), 761–774. doi: https://doi.org/10.1029/2017rs006492

Chisham, G., & Freeman, M. P. (2013). A reassessment of SuperDARN meteor echoes from the upper mesosphere and lower thermosphere. *Journal of Atmospheric and Solar-Terrestrial Physics*, *102*, 207–221. doi: https://doi.org/10.1016/j.jastp.2013.05.018

Conte, J. F., Chau, J. L., Stober, G., Pedatella, N., Maute, A., Hoffmann, P., … Murphy, D. J. (2017). Climatology of semidiurnal lunar and solar tides at middle and high latitudes: Interhemispheric comparison. *Journal of Geophysical Research: Space Physics*, *122*(7), 7750-7760. doi: https://doi.org/10.1002/2017JA024396

Drob, D. P., Emmert, J. T., Meriwether, J. W., Makela, J. J., Doornbos, E., Conde, M., … Klenzing, J. H. (2015). An update to the horizontal wind model (HWM): The quiet time thermosphere. *Earth and Space Science*, *2*(7), 301–319. doi: https://doi.org/10.1002/2014ea000089

ECMWF. (2020). Ifs documentation cy47r1 - part iv: Physical processes. In *Ifs documentation cy47r1.* Author. doi: 10.21957/cpmkqvhja

Forbes, J. M. (2009). Vertical coupling by the semidiurnal tide in earth's atmosphere. *In T. Tsuda, R. Fujii, K. Shibata, & M. A. Geller (Eds.), Climate and Weather of the Sun-Earth System(CAWSES): Selected Papers from the 2007 Kyoto Symposium(pp. 337–348). Tokyo: TERRAPUB.*

Forbes, J. M., & Zhang, X. (2012). Lunar tide amplification during the january 2009 stratosphere warming event: Observations and theory. *Journal of Geophysical Research: Space Physics*, *117*(A12). doi: https://doi.org/10.1029/2012JA017963

Goncharenko, L. P., Coster, A. J., Plumb, R. A., & Domeisen, D. I. V. (2012). The potential role of stratospheric ozone in the stratosphere-ionosphere coupling during stratospheric warmings. *Geophysical Research Letters*, *39*(8). doi: https://doi.org/10.1029/2012GL051261

Goncharenko, L. P., Harvey, V. L., Liu, H., & Pedatella, N. M. (2021). Sudden stratospheric warming impacts on the ionosphere–thermosphere system. In *Ionosphere dynamics and applications* (p. 369-400). American Geophysical Union (AGU). doi: https://doi.org/10.1002/9781119815617.ch16

Goncharenko, L. P., Harvey, V. L., Randall, C. E., Coster, A. J., Zhang, S.-R., Zalizovski, A., … Spraggs, M. (2022). Observations of pole-to-pole, stratosphere-to-ionosphere connection. *Frontiers in Astronomy and Space Sciences*, *8*. doi: 10.3389/fspas.2021.768629

Hagan, M. E. (1996, sep). Comparative effects of migrating solar sources on tidal signatures in the middle and upper atmosphere. *Journal of Geophysical Research: Atmospheres*, *101*(D16), 21213–21222. doi: https://doi.org/10.1029/96jd01374

Hersbach, H., Bell, B., Berrisford, P., Hirahara, S., Horányi, A., Muñoz-Sabater, J., … others (2020). The era5 global reanalysis. *Quarterly Journal of the Royal Meteorological Society*, *146*(730), 1999–2049. doi: https://doi.org/10.1002/qj.3803

Hibbins, R. E., Espy, P. J., Orsolini, Y. J., Limpasuvan, V., & Barnes, R. J. (2019). Superdarn observations of semidiurnal tidal variability in the mlt and the response to sudden stratospheric warming events. *Journal of Geophysical Research: Atmospheres*, *124*(9), 4862-4872. doi: https://doi.org/10.1029/2018JD030157

Hocking, W., Fuller, B., & Vandepeer, B. (2001). Real-time determination of meteor-related parameters utilizing modern digital technology. *Journal of Atmospheric and Solar-Terrestrial Physics*, *63*(2), 155-169. doi: https://doi.org/10.1016/S1364-6826(00)00138-3

Hollingsworth, A. (1971). The effect of ocean and earth tides on the semi-diurnal lunar air tide. *Journal of Atmospheric Sciences*, *28*(6), 1021 - 1044. doi: https://doi.org/10.1175/1520-0469(1971)028⟨1021:TEOOAE⟩2.0.CO;2

Jin, H., Miyoshi, Y., Pancheva, D., Mukhtarov, P., Fujiwara, H., & Shinagawa, H. (2012). Response of migrating tides to the stratospheric sudden warming in 2009 and their effects on the ionosphere studied by a whole atmosphere-ionosphere model gaia with cosmic and timed/saber observations. *Journal of Geophysical Research: Space Physics*, *117*(A10). doi: https://doi.org/10.1029/2012JA017650

Limpasuvan, V., Orsolini, Y. J., Chandran, A., Garcia, R. R., & Smith, A. K. (2016). On the composite response of the mlt to major sudden stratospheric warming events with elevated stratopause. *Journal of Geophysical Research: Atmospheres*, *121*(9), 4518-4537. doi: https://doi.org/10.1002/2015JD024401

Lin, J. T., Lin, C. H., Lin, C. Y., Pedatella, N. M., Rajesh, P. K., Matsuo, T., & Liu, J. Y. (2019). Revisiting the modulations of ionospheric solar and lunar migrating tides during the 2009 stratospheric sudden warming by using global ionosphere specification. *Space Weather*, *17*(5), 767-777. doi: https://doi.org/10.1029/2019SW002184

Liu, G., Lieberman, R. S., Harvey, V. L., Pedatella, N. M., Oberheide, J., Hibbins, R. E., … Janches, D. (2021). Tidal variations in the mesosphere and lower thermosphere before, during, and after the 2009 sudden stratospheric warming. *Journal of Geophysical Research: Space Physics*, *126*(3), e2020JA028827. doi: https://doi.org/10.1029/2020JA028827

Liu, H.-L., Bardeen, C. G., Foster, B. T., Lauritzen, P., Liu, J., Lu, G., … Wang, W. (2018). Development and validation of the whole atmosphere community climate model with thermosphere and ionosphere extension (WACCM-x 2.0). *Journal of Advances in Modeling Earth Systems*, *10*(2), 381–402. doi: https://doi.org/10.1002/2017ms001232

Liu, H.-L., Wang, W., Richmond, A. D., & Roble, R. G. (2010). Ionospheric variability due to planetary waves and tides for solar minimum conditions. *Journal of Geophysical Research: Space Physics*, *115*(A6). doi: https://doi.org/10.1029/2009JA015188

Liu, J., Zhang, D., Goncharenko, L. P., Zhang, S.-R., He, M., Hao, Y., & Xiao, Z. (2021). The latitudinal variation and hemispheric asymmetry of the ionospheric lunitidal signatures in the american sector during major sudden stratospheric warming events. *Journal of Geophysical Research: Space Physics*, *126*(5), e2020JA028859. doi: https://doi.org/10.1029/2020JA028859

Lyard, F. H., Allain, D. J., Cancet, M., Carrère, L., & Picot, N. (2021). Fes2014 global ocean tide atlas: design and performance. *Ocean Science*, *17*(3), 615–649. doi: 10.5194/os-17-615-2021

Maute, A., Fejer, B. G., Forbes, J. M., Zhang, X., & Yudin, V. (2016). Equatorial vertical drift modulation by the lunar and solar semidiurnal tides during the 2013 sudden stratospheric warming. *Journal of Geophysical Research: Space Physics*, *121*(2), 1658-1668. doi: https://doi.org/10.1002/2015JA022056

McCormack, J. P., Hoppel, K., Kuhl, D., de Wit, R., Stober, G., Espy, P., … Hibbins, R. (2017). Comparison of mesospheric winds from a high-altitude meteorological analysis system and meteor radar observations during the boreal winters of 2009–2010 and 2012–2013. *Journal of Atmospheric and Solar-Terrestrial Physics*, *154*, 132–166. doi: https://doi.org/10.1016/j.jastp.2016.12.007

Pedatella, N. M., & Forbes, J. M. (2010). Evidence for stratosphere sudden warming-ionosphere coupling due to vertically propagating tides. *Geophysical Research Letters*, *37*(11). doi: https://doi.org/10.1029/2010GL043560

Pedatella, N. M., & Liu, H. (2013). The influence of atmospheric tide and planetary wave variability during sudden stratosphere warmings on the low latitude ionosphere. *Journal of Geophysical Research: Space Physics*, *118*(8), 5333-5347. doi: 10.1002/jgra.50492

Pedatella, N. M., Liu, H.-L., & Richmond, A. D. (2012). Atmospheric semidiurnal lunar tide climatology simulated by the whole atmosphere community climate model. *Journal of Geophysical Research: Space Physics*, *117*(A6). doi: https://doi.org/10.1029/2012JA017792

Pedatella, N. M., Liu, H.-L., Sassi, F., Lei, J., Chau, J., & Zhang, X. (2014). Ionosphere variability during the 2009 ssw: Influence of the lunar semidiurnal tide and mechanisms producing electron density variability. *Journal of Geophysical Research: Space Physics*, *119*(5), 3828-3843. doi: https://doi.org/10.1002/2014JA019849

Picone, J. M., Hedin, A. E., Drob, D. P., & Aikin, A. C. (2002). NRLMSISE-00 empirical model of the atmosphere: Statistical comparisons and scientific issues. *Journal of Geophysical Research: Space Physics*, *107*(A12), SIA 15–1–SIA 15–16. doi: https://doi.org/10.1029/2002ja009430

Siskind, D. E., Harvey, V. L., Sassi, F., McCormack, J. P., Randall, C. E., Hervig, M. E., & Bailey, S. M. (2021). Two- and three-dimensional structures of the descent of mesospheric trace constituents after the 2013 sudden stratospheric warming elevated stratopause event. *Atmospheric Chemistry and Physics*, *21*(18), 14059–14077. doi: 10.5194/acp-21-14059-2021

Stober, G., Baumgarten, K., McCormack, J. P., Brown, P., & Czarnecki, J. (2020). Comparative study between ground-based observations and navgem-ha analysis data in the mesosphere and lower thermosphere region. *Atmospheric Chemistry and Physics*, *20*(20), 11979–12010. doi: 10.5194/acp-20-11979-2020

Stober, G., Kuchar, A., Pokhotelov, D., Liu, H., Liu, H.-L., Schmidt, H., ... Mitchell, N. (2021). Interhemispheric differences of mesosphere–lower thermosphere winds and tides investigated from three whole-atmosphere models and meteor radar observations. *Atmospheric Chemistry and Physics*, *21*(18), 13855–13902. doi: 10.5194/acp-21-13855-2021

Swinbank, R., & Ortland, D. A. (2003). Compilation of wind data for the upper atmosphere research satellite (uars) reference atmosphere project. *Journal of Geophysical Research: Atmospheres*, *108*(D19). doi: https://doi.org/10.1029/2002JD003135

van Caspel, W. E., Espy, P. J., Hibbins, R. E., & McCormack, J. P. (2020). Migrating tide climatologies measured by a high-latitude array of SuperDARN HF radars. *Annales Geophysicae*, *38*(6), 1257–1265. doi: https://doi.org/10.5194/angeo-38-1257-2020

van Caspel, W. E., Espy, P. J., Ortland, D. A., & Hibbins, R. E. (2022). The mid- to high-latitude migrating semidiurnal tide: Results from a mechanistic tide model and superdarn observations. *Journal of Geophysical Research: Atmospheres*, *127*(1), e2021JD036007. doi: https://doi.org/10.1029/2021JD036007

Vial, F., & Forbes, J. (1994, oct). Monthly simulations of the lunar semi-diurnal tide. *Journal of Atmospheric and Terrestrial Physics*, *56*(12), 1591–1607. doi: https://doi.org/10.1016/0021-9169(94)90089-2

Wu, Q., Ward, W., Kristoffersen, S., Maute, A., & Liu, J. (2019). Simulation and observation of lunar tide effect on high-latitude, mesospheric and lower thermospheric winds during the 2013 sudden stratospheric warming event. *Journal of Geophysical Research: Space Physics*, *124*(2), 1283-1291. doi: https://doi.org/10.1029/2018JA025476

Zhang, J., Limpasuvan, V., Orsolini, Y. J., Espy, P. J., & Hibbins, R. E. (2021). Climatological westward-propagating semidiurnal tides and their composite response to sudden stratospheric warmings in superdarn and sd-waccm-x. *Journal of Geophysical Research: Atmospheres*, *126*(3), e2020JD032895. doi: https://doi.org/10.1029/2020JD032895

Zhang, X., & Forbes, J. M. (2014a). Lunar tide in the thermosphere and weakening of the northern polar vortex. *Geophysical Research Letters*, *41*(23), 8201-8207. doi: 10.1002/2014GL062103

Zhang, X., & Forbes, J. M. (2014b). Lunar tide in the thermosphere and weakening of the northern polar vortex. *Geophysical Research Letters*, *41*(23), 8201-8207. doi: https://doi.org/10.1002/2014GL062103

Paper IV

Harvey, V. L., Datta-Barua, S., Pedatella, N. M., Wang, N., Randall, C. E., Siskind, D. E., & van Caspel, W. E. (2021). Transport of nitric oxide via Lagrangian coherent structures into the top of the polar vortex. *Journal of Geophysical Research: Atmospheres*, 126, e2020JD034523. https://doi.org/10.1029/2020JD034523

JGR Atmospheres

RESEARCH ARTICLE
10.1029/2020JD034523

Key Points:

- First demonstration of the impact of the split Arctic vortex on the geographic distribution of nitric oxide at the winter mesopause
- First evidence that a Lagrangian coherent structure inhibits horizontal transport of nitric oxide at the polar winter mesopause
- Descent of nitric oxide is five times stronger between 80 and 90 km in a westward traveling planetary wave trough compared to the ridge

Correspondence to:
V. L. Harvey,
lynn.harvey@lasp.colorado.edu

Citation:
Harvey, V. L., Datta-Barua, S., Pedatella, N. M., Wang, N., Randall, C. E., Siskind, D. E., & van Caspel, W. E. (2021). Transport of nitric oxide via Lagrangian coherent structures into the top of the polar vortex. *Journal of Geophysical Research: Atmospheres*, *126*, e2020JD034523. https://doi.org/10.1029/2020JD034523

Received 31 DEC 2020
Accepted 5 MAY 2021

Author Contributions:
Conceptualization: V. Lynn Harvey
Data curation: V. Lynn Harvey, Willem E. van Caspel
Formal analysis: V. Lynn Harvey, Seebany Datta-Barua, Nicholas M. Pedatella, Ningchao Wang, Willem E. van Caspel
Funding acquisition: V. Lynn Harvey
Investigation: V. Lynn Harvey, Nicholas M. Pedatella, Ningchao Wang
Methodology: V. Lynn Harvey, Seebany Datta-Barua, Nicholas M. Pedatella
Project Administration: V. Lynn Harvey

Transport of Nitric Oxide Via Lagrangian Coherent Structures Into the Top of the Polar Vortex

V. Lynn Harvey[1,2], Seebany Datta-Barua[3], Nicholas M. Pedatella[4], Ningchao Wang[5], Cora E. Randall[1,2], David E. Siskind[6], and Willem E. van Caspel[7,8]

[1]Laboratory for Atmospheric and Space Physics, University of Colorado, Boulder, CO, USA, [2]Department of Atmospheric and Oceanic Sciences, University of Colorado, Boulder, CO, USA, [3]Department of Mechanical, Materials, and Aerospace Engineering, Illinois Institute of Technology, Chicago, IL, USA, [4]High Altitude Observatory, National Center for Atmospheric Research, Boulder, CO, USA, [5]Department of Atmospheric Sciences, Hampton University, Hampton, VA, USA, [6]Space Science Division, Naval Research Laboratory, Washington, DC, USA, [7]Department of Physics, Norwegian University of Science and Technology, Norway, [8]Birkeland Centre for Space Science, University of Bergen, Bergen, Norway

Abstract The energetic particle precipitation (EPP) indirect effect (IE) refers to the downward transport of reactive odd nitrogen ($NO_x = NO + NO_2$) produced by EPP (EPP-NO_x) from the polar winter mesosphere and lower thermosphere to the stratosphere where it can destroy ozone. Previous studies of the EPP IE examined NO_x descent averaged over the polar region, but the work presented here considers longitudinal variations. We report that the January 2009 split Arctic vortex in the stratosphere left an imprint on the distribution of NO near the mesopause, and that the magnitude of EPP-NO_x descent in the upper mesosphere depends strongly on the planetary wave (PW) phase. We focus on an 11-day case study in late January immediately following the 2009 sudden stratospheric warming during which regional-scale Lagrangian coherent structures (LCSs) formed atop the strengthening mesospheric vortex. The LCSs emerged over the north Atlantic in the vicinity of the trough of a 10-day westward traveling planetary wave. Over the next week, the LCSs acted to confine NO-rich air to polar latitudes, effectively prolonging its lifetime as it descended into the top of the polar vortex. Both a whole atmosphere data assimilation model and satellite observations show that the PW trough remained coincident in space and time with the NO-rich air as both migrated westward over the Canadian Arctic. Estimates of descent rates indicate five times stronger descent inside the PW trough compared to other longitudes. This case serves to set the stage for future climatological analysis of NO transport via LCSs.

Plain Language Summary Energetic particles from the sun and the magnetosphere impinge upon Earth's upper atmosphere and create reactive odd nitrogen (NOx) in the mesosphere and lower thermosphere. Descent in the winter polar vortex effectively transports this NOx down to the stratosphere where it can destroy ozone. State-of-the-art models currently underestimate this vertical transport by a factor of 4. Previous studies have examined the NOx descent averaged over the entire polar region, but this study considers longitudinal variations. We examine a case study during late January 2009 and find a closed circulation coincident with the trough of a planetary wave over the north Atlantic at 90 km with shear zones inhibiting horizontal mixing to the north, east, and south. This circulation (1) contains elevated NOx, (2) is associated with five times stronger descent compared to other longitudes, and (3) is the natural upward continuation of the westward tilting polar vortex in the stratosphere and mesosphere. Thus, this meteorological feature near the mesopause provides a transport pathway for air to enter the top of the polar vortex. This is the first work to illustrate the zonally asymmetric nature of NOx descent in the polar winter upper mesosphere and couple it to the vortex below.

1. Introduction

The winter polar vortex plays a key role in controlling the atmospheric response to energetic particle precipitation (EPP). In particular, the polar vortex modulates the EPP Indirect Effect (EPP IE), defined as descent to the stratosphere of reactive odd nitrogen ($NO_x = NO + NO_2$) produced by EPP (EPP-NO_x) (Randall et al., 2006, 2007). Downward transport of EPP-NO_x from the thermosphere into the mesosphere occurs mainly via rapid eddy and molecular diffusion (Garcia et al., 2007; Meraner & Schmidt, 2016; Smith

Resources: V. Lynn Harvey, Nicholas M. Pedatella
Software: V. Lynn Harvey, Seebany Datta-Barua, Ningchao Wang
Supervision: V. Lynn Harvey
Validation: V. Lynn Harvey
Visualization: V. Lynn Harvey, Seebany Datta-Barua, Ningchao Wang, Willem E. van Caspel
Writing – original draft: V. Lynn Harvey
Writing – review & editing: V. Lynn Harvey, Seebany Datta-Barua, Nicholas M. Pedatella, Ningchao Wang, Cora E. Randall, David E. Siskind, Willem E. van Caspel

et al., 2011; Smith, 2012). Below the mesopause, air gets swept into the global wave-driven residual circulation (Andrews et al., 1987), which is characterized by rising motion over the summer pole, strong cross-equatorial flow from the summer hemisphere to the winter hemisphere, and descent in the winter polar vortices (Fisher et al., 1993; Kvissel et al., 2012; Manney et al., 1994; Rosenfield et al., 1994; Schoeberl et al., 1992). In the lower mesosphere and stratosphere, NO reacts with ozone, maintaining an equilibrium with NO_2 via the NO_x catalytic cycle (e.g., Garcia & Solomon, 1994). Thus, any excess stratospheric NO_x from the EPP IE has the potential to impact ozone distributions and thus net radiative heating rates, temperatures, winds, and wave filtering (e.g., Baumgaertner et al., 2011; Sinnhuber et al., 2018).

The EPP IE is especially pronounced following prolonged sudden stratospheric warmings (SSWs) (e.g., Limpasuvan et al., 2016; McLandress et al., 2013; Siskind et al., 2010) when strong mesospheric descent transports unusually large amounts of EPP-NO_x down to the polar stratosphere. SSWs are dramatic wintertime dynamical events, driven by upward propagating planetary waves, that result in a warming of the polar stratosphere, a reversal of the westerly polar night jet stream, and a displaced or split polar vortex (Baldwin et al., 2020; Butler et al., 2017; Scherhag, 1952). While many studies have used zonal averages to show the descent of EPP-NO_x (e.g., Bailey et al., 2014; Hauchecorne et al., 2007; Natarajan et al., 2004; Paivarinta et al., 2016; Pérot et al., 2014; Pérot & Orsolini, 2021; Randall et al., 1998, 2006, 2007, 2009; Reddmann et al., 2010; Rinsland et al., 2005; Siskind et al., 1997, 2000), only a few have shown how the NO_x distribution depends on latitude and longitude (Randall et al., 2005; Salmi et al., 2011; Siskind et al., 2021); and none have shown how NO_x descent varies in space and time. This work fills this gap by analyzing zonal asymmetries in nitric oxide (NO, the primary constituent of NO_x at mesosphere and lower thermosphere (MLT) altitudes), and by quantifying the dependence of NO descent on both latitude and longitude.

Salmi et al. (2011) showed polar maps of enhanced NO_x near 50, 60, and 70 km in February and March following the 2009 SSW, which suggested that zonal averaging could be appropriate to delineate the region of elevated NO_x at those altitudes. However, Newnham et al. (2020) compared zonal asymmetries in Solar Occultation For Ice Experiment (SOFIE) NO from 70-90 km during 17 geomagnetic storms from 2008–2014 to the climatologically preferred longitude sector of the mesospheric polar vortex (Harvey et al., 2018) and hypothesized enhanced vertical coupling when the two are in-phase. Indeed, climatologically, maximum observed electron fluxes occur over the Scandinavian longitude sector (Newnham et al., 2020) and the mesospheric polar vortex is present most often in the longitude sector over nearby Greenland (Harvey et al., 2018), suggesting an in-phase relationship between the two is common. This is consistent with maximum mesospheric descent rates being displaced toward northern Greenland following the 2004 SSW (Winick et al., 2009). Recent analysis of three-dimensional descent also confirms the highest NO concentrations near 300°E longitude following the 2013 SSW (Siskind et al., 2021). In contrast to Salmi et al. (2011), results presented here confirm that zonally asymmetric vertical coupling occurred at an altitude higher than their analysis, near the mesopause, following the 2009 SSW. This work identifies a region of enhanced NO and strong descent at the mesopause over the north Atlantic and Canadian Arctic in the wake of the SSW and shows that this region is located directly above the reforming mesospheric polar vortex.

At MLT altitudes (60–110 km) EPP-NO_x consists primarily of NO, which is initially distributed over a range of geomagnetic latitudes that span auroral and subauroral regions. A notable distinction exists between NO created inside versus outside the polar night. In sunlight at MLT altitudes, NO has a chemical lifetime of several days, whereas in the polar night NO may persist for weeks or months (Bender et al., 2019; Brasseur & Solomon, 2005; Minschwaner & Siskind, 1993). In theory, NO that remains confined to polar darkness, where its lifetime is long, may descend to the stratosphere while NO that is transported to sunlit latitudes will be destroyed. It is therefore of primary interest to identify mechanisms that act to confine NO to high latitudes in winter. Motivated by Sun-Earth coupling via the EPP IE, and by the fact that models underestimate the EPP IE (Funke et al., 2017; Meraner et al., 2016; Orsolini et al., 2017; Pettit et al., 2019; Randall et al., 2015; Sheese et al., 2013; Sinnhuber et al., 2018; Smith-Johnsen et al., 2018), this work examines the effect of Lagrangian coherent structures (LCSs) on the transport of NO in the polar winter MLT. We hypothesize that confinement of NO to high latitudes by LCSs effectively increases the NO lifetime and facilitates NO transport into the top of the polar vortex. Since descent occurs in three dimensions (Callaghan & Salby, 2002; Demirhan Bari et al., 2013; Kinoshita et al., 2010), longitudinal variability can be highly relevant, and this is assessed in our analysis.

LCSs are transport barriers that define different characteristic regions of a flow; they are objective and quantifiable as surfaces of maximum finite-time Lyapunov exponent (FTLE) (Haller, 2015). The FTLE is a scalar field that measures the degree of stretching after a given interval of time of a fluid particle at a certain point, relative to its initial extent. The basic equations may be found in numerous resources (e.g., Shadden, 2005), and are summarized here. A flow map, F, is defined as a mapping of particles at initial locations x_0 in a fluid to final positions over an interval of time, $t_f - t_0$, using velocity v. The mapping equation is:

$$F_{t_0}^{t_f}\left(x_0\right) = x\left(t_f; x_0, t_0\right) = x_0 + \int_{t_0}^{t_f} v\left(x, t\right) dt \tag{1}$$

The flow map traces each fluid particle from an initial position x_0 at a chosen start time t_0 to a final position x_f at a chosen final time t_f. The flow map can be Taylor expanded about a point x_0 as

$$F_{t_0}^{t_f}\left(x\right) \approx F_{t_0}^{t_f}\left(x_0\right) + \mathbf{J}\left(x - x_0\right) + \ldots \tag{2}$$

where the three dots represent higher-order terms in the Taylor expansion. The Jacobian, $\mathbf{J}$, of the flow map is a linearization about x_0, consisting of the matrix of partial derivatives of the final position coordinates with respect to the initial position coordinates. The Jacobian consists of ratios of the final position separation to initial separation of particles infinitesimally near x_0 at time t_0 and thus quantifies the amount of stretching that occurred between t_0 and t_f. In this work, we calculate LCSs in two dimensions (longitude vs. latitude). Future work will calculate LCSs in three dimensions, a more ideal framework for studying the effect of LCSs on vertical transport.

FTLEs are defined as the normalized maximum singular value of the Jacobian matrix of a flow map. An FTLE is computed for every initial particle x_0 in the domain. LCSs are then identified as ridges in FTLE maps. FTLEs have long been used to study mixing at the edge of the polar vortex (Bowman, 1993; Pierce & Fairlie, 1993). LCSs are similar to the popular Lagrangian descriptor "Function M" to define the stratospheric polar vortex edge (e.g., Curbelo et al., 2017; de la Camara et al., 2012; Madrid & Mancho, 2009; Smith & McDonald, 2014). The salient difference between those studies and this work is that they were at stratospheric altitudes, and the focus here is near the mesopause. LCSs have also been identified recently in the thermosphere at midlatitudes, where they act to channel the transport of water vapor plumes associated with space traffic (Wang et al., 2017). Using the same methodologies as Wang et al. (2017), we address whether LCSs reside near the polar winter mesopause and if so, whether they focus the descent of EPP-NO_x into the top of the polar vortex. To accomplish this, we present a case study as a demonstration of the approach and to underpin climatological studies that will be the subject of future work.

This study is structured as follows. Section 2 briefly describes the whole atmosphere model, the trajectory model, and the observations used in this work. Section 3 presents an overview of the meteorology during and after the January 2009 SSW that serves as our case study. Section 4 demonstrates the impact of the split Arctic vortex on the spatial distribution of NO near the mesopause. Section 5 then presents the case study of regionally enhanced NO, bounded horizontally by multiple LCSs, situated above the mesospheric polar vortex. The LCSs are in the vicinity of the trough of a westward traveling 10-day planetary wave (PW). An analysis of vertical transport suggests that descent in the PW trough is five times stronger than at other longitudes. Throughout the study, we make every effort to evaluate the model with observations. Section 6 summarizes the conclusions and gives future directions.

2. Models and Observations

The Whole Atmosphere Community Climate Model with thermosphere-ionosphere eXtension (WACCMX) spans the Earth's surface to ~500 km and simulates relevant processes from the troposphere to the thermosphere and ionosphere (Liu et al., 2010). These include major-species diffusive transport, ion drag, Joule heating, nonlocal thermodynamic equilibrium, and ionospheric physics and chemistry. The WACCMX + DART configuration used here (see Pedatella et al., 2013; Pedatella, Raeder, et al., 2014) employs the Data Assimilation Research Testbed (DART) ensemble adjustment Kalman filter to constrain model meteorology up to ~100 km via data assimilation (Anderson, 2001). For the present study, WACCMX + DART assimilated conventional meteorological observations (i.e., radiosonde temperature and winds, satellite drift winds, etc.), refractivity from GPS radio occultation in the troposphere and stratosphere, and Sounding of the Atmosphere using Broadband Emission Radiometry (SABER) and Microwave Limb Sounder (MLS) temperature observations from ∼20 to ∼100 km.

The model spatial resolution is 1.9° × 2.5° horizontally and 1–3.5 km in the vertical. Horizontal winds are output hourly and NO volume mixing ratio (VMR) is output every 6 h. The model incorporates a state-of-the-art gravity wave scheme (Richter et al., 2010) and this is important for MLT dynamics since those altitudes are only constrained by sparse observations. The turbulent Prandtl number that governs thermal diffusion is set to $Pr = 2$ as suggested by Garcia et al. (2014). The Heelis empirical convection pattern (Heelis et al., 1982) is used to account for geomagnetic activity, though geomagnetic activity levels were low during the case study presented here. In the polar MLT, auroral ionization is calculated using the empirical oval of Roble and Ridley (1987), which depends on a specified hemispheric power or geomagnetic K_p index. The model is forced with observed, time-varying values of the solar F10.7 cm radio flux and the K_p index. Neither medium-energy electrons (Pettit et al., 2019) nor D-region ion chemistry (Andersson et al., 2016) is included.

To identify LCSs in WACCMX + DART, hourly model horizontal flow fields at the 0.001 hPa pressure level (near 90 km) are input to the Ionosphere-Thermosphere Algorithm for LCS (ITALCS) trajectory calculation (Wang et al., 2018). An FTLE value is computed at every model longitude and latitude based on 24 h of integration, and these FTLE values are output every 6 h during the month of January 2009. Hourly trajectory positions originating from each model grid point are also archived. Analyses shown here will be limited to the Northern Hemisphere (NH).

A fundamental advantage of using WACCMX + DART flow fields to drive the ITALCS trajectory model is the direct constraint of the MLT region by assimilating SABER and MLS observations. As demonstrated by Pedatella, Raeder, et al. (2014), the assimilation of middle atmosphere temperature observations improves the specification of MLT dynamics even when stratospheric PWs are large. Data assimilation alleviates the climatological mesospheric temperature bias in the model and leads to an improved representation of short-term tidal variability (Pedatella et al., 2016). Also, Siskind et al. (2015) and Pedatella et al. (2018) show that running WACCM and WACCMX with data assimilation in the mesosphere results in more NO descent during February 2009 than running these models without data assimilation, partly correcting the well-known model underestimate noted above.

In this study, we compare model dynamics and chemistry to observations to ensure model fidelity. SABER observations (Russell et al., 1999) are used to evaluate the model geopotential height (GPH) fields. SABER GPH is derived from retrieved temperature and pressure assuming hydrostatic balance (Remsberg et al., 2008). Here, we use version 2.0 temperature data, which have 2 km vertical resolution and precision estimates of less than 4K throughout the mesosphere (García-Comas et al., 2008; Remsberg et al., 2003). Recent comparison of SABER and lidar temperatures shows best agreement between 85 and 95 km (Dawkins et al., 2018), the altitude range of interest here.

We also utilize Atmospheric Chemistry Experiment Fourier Transform Spectrometer (ACE-FTS) (Bernath et al., 2005) and SOFIE (Gordley et al., 2009; Russell et al., 2009) NO VMR measurements to evaluate the model representation of NO. ACE-FTS version 3.5 and SOFIE version 1.3 data have vertical resolutions in the mesosphere of 3–4 km (Boone et al., 2013) and 2 km (Marshall et al., 2011), respectively. ACE-FTS and SOFIE NO data have reported uncertainty estimates of ∼80% at 60 km (the highest altitude reported) (Sheese et al., 2016) and 27%–37% at 90 km (Hervig et al., 2019), respectively. Both ACE-FTS and SOFIE sample high northern latitudes (63–71°N) during the case study presented here. Both are solar occultation instruments; and while spatial coverage is sparse, they are well suited to observe zonal asymmetries since they take measurements around a circle of latitude each day.

Since our focus is near 60°N, we leverage hourly Super Dual Auroral Radar Network (SuperDARN, hereafter SD) high-frequency radar measurements of the zonal wind (Hall et al., 1997) to evaluate the model zonal winds near 100 km. During the 2009 case study, there were six operational SD radars spanning approximately 180° of longitude. SD measures the phase shift of meteor echoes to derive the neutral wind velocity carrying the meteor ablation trails. The vertical SD meteor echo distribution extends between 75 and

125 km altitude and is approximately Gaussian, with a mean height of ∼100 km altitude and a full width at half maximum of 25–35 km (Chisham & Freeman, 2013; Chisham, 2018). Hourly wind measurements are constructed by least-squares fitting a single horizontal wind vector to hourly binned meteor echo line-of-sight velocities.

To compare SD measurements to the modeled winds, WACCMX-DART winds are first interpolated to an equidistant vertical grid between 75 and 125 km altitude with 2.5 km spacing. The model winds are then vertically averaged with a weighting function representing the SD meteor echo distribution. The vertically averaged winds are sampled at the model gridpoints closest to the locations of operational SD stations. To calculate the temporal evolution of the mean zonal winds at each station, for both the SD observations and model winds, a function representing a mean wind and 24, 12, and 8 h waves are least-squares fitted to the hourly data using a 4-day sliding window following Hibbins and Jarvis (2008) and Hibbins et al. (2011).

Finally, MERRA version 2 reanalysis data (Bosilovich et al., 2015; Molod et al., 2015) are used to define the polar vortex in the stratosphere and mesosphere using the definition described by Harvey et al. (2002). The 6-h instantaneous three-dimensional analyzed meteorological fields in the M2I6NVANA collection are used here (Global Modeling and Assimilation Office, 2015). The data are provided four times daily with a horizontal resolution of 0.5° latitude by 0.625° on 72 model levels that extend from the Earth's surface to 0.015 hPa (∼75 km). This reanalysis assimilates MLS temperature and ozone observations above 5 hPa beginning in August 2004 (Gelaro et al., 2017), which constrains the dynamics in the upper stratosphere and lower mesosphere.

3. The 2009 SSW

The January 2009 vortex split SSW has been extensively studied as it remains the strongest and most prolonged SSW in the satellite era (e.g., Coy et al., 2011; Harada et al., 2010; Manney et al., 2009; Schneidereit et al., 2017), and vertical coupling to the thermosphere (e.g., Sassi et al., 2013, 2016) and ionosphere (e.g., Goncharenko, Chau, et al., 2010; Goncharenko, Coster, et al., 2010; Jin et al., 2012; Liu et al., 2011; Pancheva & Mukhtarov, 2012; Pedatella et al., 2016) is apparent during solar minimum. An overview of this event is given in Figure 1 with an emphasis on the MLT. The altitude-time perspective of spatially averaged quantities given in Figures 1a and 1b is often used to visualize the time evolution of SSWs and mesospheric coolings (Labitzke, 1972) as well as the vertical transport of NO. Figures 1a and 1b show that WACCMX + DART reproduces the observed SSW (which began on January 24), in agreement with Pedatella et al. (2018). The model qualitatively reproduces observed features, despite differences in absolute values, for example, in the amplitude of the mesospheric cooling and the temperature of the elevated stratopause. The elevated stratopause is indicative of strong planetary and gravity wave-driven descent in February that resulted in large amounts of NO transported to the stratosphere despite low solar and geomagnetic activity levels (e.g., Randall et al., 2009).

Previous studies of the EPP IE have generally included analyses of NO descent using zonal averages, without regard for spatial inhomogeneities in dynamic or chemical quantities. However, day-to-day wind and NO spatial patterns in the upper mesosphere have not yet been shown. This work fills this gap at the 90 km altitude level and the January 20–30 time period, indicated by the white horizontal lines in Figures 1a and 1b. Since this case study focuses on an altitude and time period following the mesospheric cooling event and preceding the elevated stratopause, there is an intensification in polar descent during the time period analyzed.

Figures 1c and 1d give NH polar maps of GPH at 0.001 hPa (∼90 km) on January 23, immediately following the peak stratospheric warming and mesospheric cooling. These maps demonstrate large zonal variability and that SABER (panel c) and the model (panel d) are in agreement with respect to the location of high-pressure and low-pressure systems near the mesopause; both the observations and the model indicate a region of low pressure over the northeast Atlantic and Arctic ocean basins and relatively high pressure over east Asia and the southeast United States. This level of agreement between the model and the observations holds for the duration of this case study. Note, however, since the model assimilates SABER this is not an independent validation. Both the observations and the model indicate maximum zonal GPH variations

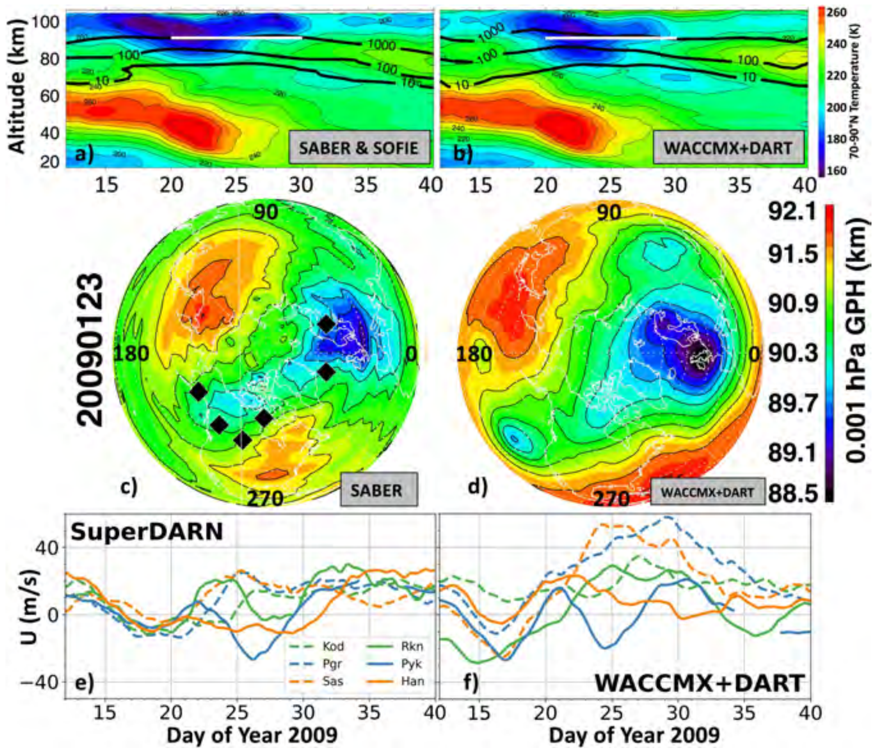

Figure 1. (Top panels) Altitude-time plots of 70°N–90°N average temperature (in color) and zonal mean NO VMR (thick black contours, in ppbv) based on (a) SABER and SOFIE observations and (b) WACCMX + DART from January 12 to February 10, 2009. Major SSW conditions were met on January 24. The NO VMR in panel (b) is the WACCMX + DART values at the SOFIE measurement latitudes. The white horizontal lines at 90 km from January 20 to 30 denote the altitude and time that is the focus of this work. (Middle panels) NH polar plots of daily average GPH in (c) SABER and (d) WACCMX + DART on January 23, 2009 at 0.001 hPa (~90 km). The locations of the six SuperDARN radars operating during this time are indicated by the black diamonds in panel (c). These six radars are, from west to east, in Kodiac Alaska USA (Kod; 57.6°N, 152.2°W), Prince George British Columbia Canada (Pgr; 54°N, 122.6°W), Saskatoon Saskatchewan Canada (Sas; 52.2°N, 106.5°W), Rankin Inlet Nunavut Canada (Rkn; 62.8°N, 92.1°W), Pykkvibaer Iceland (Pyk; 63.8°N, 20.6°W), and Hankasalmi Finland (Han; 62.3°N, 26.6°E). (Bottom panels) time-series of 4-day average zonal winds near 100 km based on (e) SuperDARN and (f) WACCMX + DART. GPH, geopotential height; NH, Northern Hemisphere; SSW, sudden stratospheric warming; VMR, volume mixing ratio.

of 2–3 km in the 50°N–70°N latitude band. This is generally consistent with previously reported large PW amplitudes at this latitude, altitude, and time (Yuan et al., 2012, see their Figure 4).

Comparison of model output to coincident observations with no spatial or temporal averaging is a stringent test of the model. Figures 1e and 1f show SuperDARN radar (panel e) and model (panel f) zonal winds centered on 100 km. This analysis further evaluates the model by comparing with an independent observational source (that was not assimilated). While there are differences between the evolution of the radar versus the model zonal winds at the six radar locations and the amplitudes of the zonal winds are up to a factor of two larger in WACCMX + DART than in observations, the model does simulate a shift from westerly (positive values) to easterly (negative values) zonal winds before the vortex split on January 20 and then a shift back to westerly after the SSW. Further, the model is in excellent agreement with the Pyk radar (solid blue line) over Iceland, which sampled the flow along the poleward flank of the PW trough that we will present in Figure 3. At that location, both the model and the radar indicate a shift from ~10 m s^{-1} westerlies around January 22 to ~20 m s^{-1} easterlies around January 25 and then back to westerlies by the end

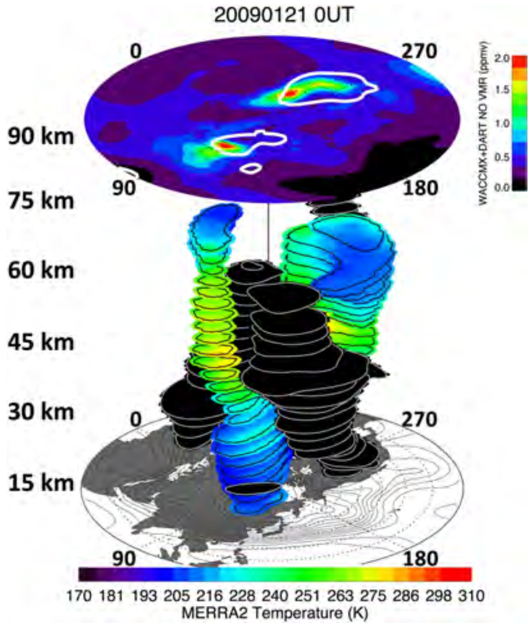

Figure 2. 3-D representation of the Arctic polar vortex (colored by temperature) and stratospheric anticyclones (colored black) on January 21, 2009, at 00 UT based on MERRA-2. An NH polar map of 90 km NO VMR from WACCMX + DART hovers above the split vortex. White contours in the NO map indicate where model GPH deviates by more than 1 km below the zonal mean, indicative of PW troughs. GPH, geopotential height; NH, Northern Hemisphere; PW, planetary wave; VMR, volume mixing ratio.

of the month (note that no Pyk observations are available from 5 UT on Day 34 to 18 UT on Day 37). Overall, Figure 1 is intended to demonstrate that while there are quantitative differences between the model and the observations, there is qualitative agreement in terms of both the zonal mean evolution and the synoptic-scale meteorology in the MLT during this dynamically active time.

4. Imprint of the Split Vortex on NO at the Mesopause

Since WACCMX + DART captures certain key aspects in the MLT for this case, we next show how the split vortex in the stratosphere and mesosphere impacts the NO distribution near the mesopause. Figure 2 illustrates enormous zonal asymmetries that occur throughout the stratosphere and mesosphere on January 21 at 0 UT. At this time the polar vortex (stacked circular regions colored by temperature) is split from 34 to 73 km and there are two vertically deep anticyclones (black circular regions) located over the oceans. SSWs are known to exhibit significant zonal asymmetries due to the large PW structures that drive them (Matsuno, 1970) and zonal averaging obscures these spatial inhomogeneities.

The Arctic polar vortex and anticyclones in Figure 2 are based on MERRA-2 data and are independent of the NO and GPH polar map at 90 km, which is from WACCMX + DART. White contours at 90 km delineate two regions of negative eddy (deviations from the zonal mean) GPH associated with cyclonic flow in the model. These low GPH regions are coincident with the two areas of elevated NO VMR. That the split vortex extends to this altitude was alluded to by Iida et al. (2014), who showed two low MLS GPH regions in polar maps at 90 km on January 19 (2 days earlier). The new result here is that this split circulation resulted in a split distribution of NO. Unfortunately, ACE-FTS and SOFIE measurements (which occurred between 64°N and 69°N on this day) did not intersect the regions of high NO VMR (located between 45°N and 50°N) in the model thus the simulated split NO pattern cannot be confirmed using chemical observations. In the weeks leading up to this split, the modeled NO in the upper mesosphere generally maximized over the pole (not shown). Then, on January 19 at 18 UT both the stratospheric vortex and the GPH and NO fields at 90 km split simultaneously and in similar orientations, with high NO VMR regions in the same longitude sectors as the two polar vortex lobes below. The 90 km NO and eddy GPH fields remained split for 3.5 days (not shown), thus outlasting variability that occurs on diurnal time scales. This result suggests that PW-driven zonal asymmetries in the stratosphere and mesosphere can leave an "imprint" on the NO distribution at the mesopause.

5. Case Study: NO Transport as Evidenced by Lagrangian Coherent Structures

Next, we show the effect of LCSs on the spatial distribution of NO near 90 km on 1 day in WACCMX + DART. Figure 3 gives polar maps on January 26 at 0.001 hPa (near 90 km) to illustrate the horizontal circulation and the spatial patterns in temperature and NO in the wake of the vortex split. Figure 3a shows the GPH near 90 km, similar to Figure 1d but three days later. Also shown here are bold light gray, dark gray, and black contours illustrating the vortex edge location at 30, 50, and 70 km, respectively, which progressively shifts west with increasing altitude. The region of low pressure that resides over the north Atlantic near 90 km is thus seen to be a natural continuation of this westward tilting mesospheric vortex as indicated by the three contour rings (in light gray, dark gray, and black). Horizontal winds flow roughly parallel to both the vortex edge and GPH contours. Vertical continuity in the vortex wind system is consistent with

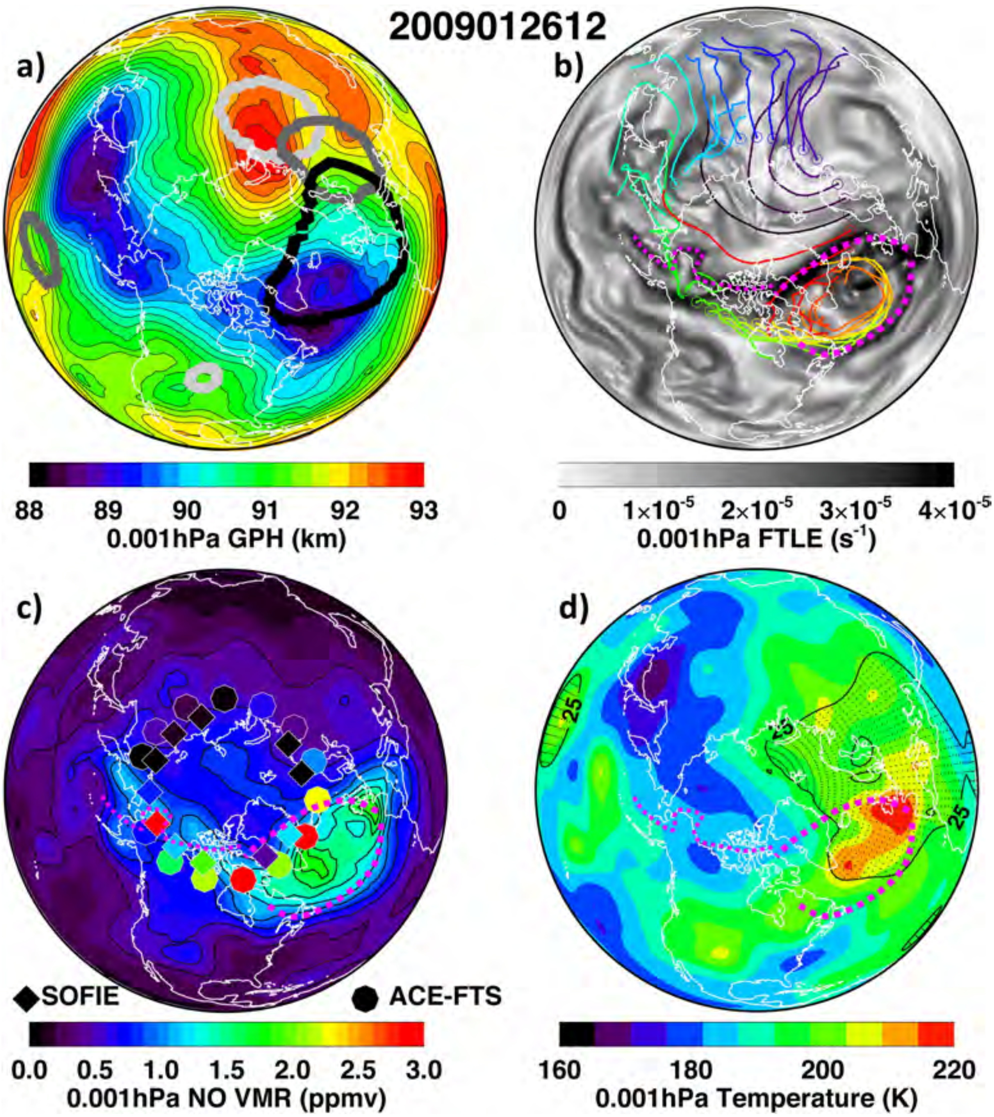

Figure 3. NH polar maps at 0.001 hPa (~90 km) on January 26, 2009 at 12 UT of (a) WACCMX + DART GPH (in color) and MERRA-2 polar vortex edges at 30 km (light gray), 50 km (dark gray), and 70 km (black), (b) simulated FTLE (light and dark gray shading) and 24-h forward trajectory paths (colored lines) for air that originated at the locations given by the open colored circles at 65°N, spaced every 10° in longitude; the pink dotted lines highlight FTLE ridges of interest and these are repeated in panels (c) and (d), (c) NO VMR in WACCMX + DART (color contoured), and NO VMR observed by SOFIE (diamonds) and ACE-FTS (octagons) (note, the ACE-FTS measurement north of Hudson Bay corresponds to a NO VMR of 4.6 ppmv which is outside the color bar range), and (d) WACCMX + DART temperature (in color) with black stippling and boundary lines indicating where the deviation of WACCMX + DART atomic oxygen is at least 25% larger than the zonal mean at each latitude. Both warm temperatures and high atomic oxygen are proxies for descent. FTLE, finite-time Lyapunov exponent; NH, Northern Hemisphere; PW, planetary wave; VMR, volume mixing ratio.

Bhattacharya and Gerrard (2010) who showed mesopause winds to be correlated with stratopause winds when the vortex is displaced from the pole, as it is on this day.

Figure 3b shows the FTLE field (light to dark gray shaded) and 24-h forward trajectories (colored lines) that originated at 65°N, also near 90 km. High FTLE values, or FTLE ridges (dark gray shading), indicate barriers to horizontal transport due to large shear sustained over time. These FTLE ridges are hereafter referred to as LCSs and their spatial distribution reveals the complex nature of the flow field at this altitude and time. The LCSs that are of interest in this work are indicated by the pink dotted lines that trace FTLE ridges located along the poleward, eastern, and equatorward flanks of the north Atlantic low-pressure center shown in Figure 3a. Another LCS of interest extends from western Greenland to Alaska. The concentric trajectory paths inside the low-pressure center over the north Atlantic indicate easterly flow over Iceland, in agreement with observed (SuperDARN radar at Pyk) and modeled zonal winds near 100 km, shown in Figures 1e and 1f. The trajectories illustrate that air inside the north Atlantic low-pressure center remains confined to the 50°N–70°N latitude band (yellow and orange lines), whereas air outside the low (green, blue, and purple lines) is rapidly transported to low latitudes. A well-known property of LCSs is that air parcels on the same side of an LCS experience slow separation for a given amount of time compared to air parcels on opposite sides of an LCS (du Toit & Marsden, 2010). This property has implications for the distribution of NO, in that high latitude air bounded by LCSs is not subject to transport to tropical latitudes. In this case, this sequestration acts to increase the NO chemical lifetime since photolysis rates will tend to be lower between 50°N and 70°N than at low to mid-latitudes. On this day, the latitude distribution of NO lifetime at 0.001 hPa (~90 km) is: 5 days at 20°N, 6 days at 50°N, 10 days at 61°N, 20 days at 67°N, 30 days at 68°N, 40 days at 69°N, and >50 days at 70°N (Brasseur & Solomon, 2005; Minschwaner & Siskind, 1993). Thus, NO contained within a circulation spanning 50°N–70°N will experience more photolysis along the Equatorward flank and negligible photolysis along the poleward flank. If we assume that air spends as much time at 50°N as it does at 70°N, then to first order NO that circulates between 50°N and 70°N will live five times longer ($(55 + 6)/2 = \sim30$ days) than NO that is transported equatorward of 50°N (6 days). These LCSs persist for a week as the low-pressure center migrates to the west, remaining in the 50°N–70°N latitude band; the region occupied by the closed circulation maintains a fairly constant area of ~2 million km^2. The closed circulation persists despite enhancements in the migrating semi-diurnal solar (He et al., 2017) and lunar tides (Chau et al., 2015; Pedatella, Liu, et al., 2014). Even with SSW-induced tidal enhancements, the migrating diurnal and semi-diurnal tidal amplitudes are small (<0.5K) poleward of 40°N at 90 km (Sassi et al., 2013).

Next, we show that the FTLE ridges of interest in Figure 3b are spatially coincident with large horizontal NO gradients in the model, and to a lesser extent in the observations. Figure 3c reveals regionally enhanced model NO over the north Atlantic with maximum mixing ratios located inside the low-pressure center and sharp horizontal gradients coincident with large horizontal gradients in GPH in Figure 3a and the pink dotted lines in Figure 3b. ACE-FTS and SOFIE NO observations are superimposed using filled octagons and diamonds, respectively. Between 50°N and 70°N in the western hemisphere where WACCMX + DART NO VMR values are generally enhanced, the model underestimates observed NO VMR by about a factor of 2, a common trait among models. However, daily average WACCMX + DART NO at the ACE-FTS and SOFIE measurement latitudes is within measurement uncertainties. The observations confirm a distinct PW-1 pattern in NO with high values over the north Atlantic and the Canadian Arctic and generally lower values over Asia. The observations indicate elevated NO VMR values along the extreme poleward flank of the region of enhanced model NO over the north Atlantic. Both the model and the observations also show a tongue of high NO VMR values (>1 ppmv) that extends westward over the Canadian Arctic. These elevated NO values lie along the poleward side of the FTLE ridge that extends to the west from Greenland to Alaska. This westward extension of elevated NO VMR values is likely related to the ongoing westward migration of the entire pattern that will be shown next.

Finally, coincident with the region of high model NO VMR (Figure 3c) are warm model temperatures (Figure 3d) suggestive of adiabatic heating. Temperatures at 60°N, 0.001 hPa over the north Atlantic are 20–40K warmer than at other longitudes around this latitude circle. The black stippled region in Figure 3d is where model atomic oxygen is 25% higher than the zonal mean at each latitude. Atomic oxygen (O) is a dynamical tracer at these altitudes; it has a steep vertical gradient (increasing VMR with increasing altitude) such that high O is a proxy for descent from the lower thermosphere (Smith et al., 2010; Winick et al., 2009). The model is self-consistent in that regions of high O correspond to regions of warm temperatures, and both suggest descending motion over the north Atlantic. These regional enhancements in the NO and descent would be obscured in zonal averages. Indeed, standard transformed Eulerian mean (TEM) estimates of vertical transport are unable to distinguish variations around a latitude circle.

To summarize, all of the combined aspects presented here paint the following picture: There is a closed circulation coincident with low GPH over the north Atlantic at 90 km with LCSs inhibiting horizontal mixing to the north, east, and south. This circulation (1) contains elevated NO, (2) is associated with enhanced descent, and (3) is the natural upward continuation of the westward tilting polar vortex in the stratosphere and mesosphere. Thus, this meteorological feature provides a transport pathway for air to enter the top of the polar vortex. This is the first work to illustrate the zonally asymmetric nature of NO descent in the polar winter upper mesosphere and couple it to the vortex below.

Next, we examine how the PW patterns in NO and GPH evolve in longitude and time at the ACE-FTS and SOFIE measurement latitudes. Figure 4 gives longitude-time Hovmöller diagrams of NO (color) and eddy GPH (deviation from the zonal mean, contours) at 90 km to illustrate east-west movement of the PW in NO and GPH between 63°N and 71°N latitude during late January 2009. WACCMX + DART NO and eddy GPH are shown in the top row, interpolated to the ACE-FTS (Figure 4a) and SOFIE (Figure 4b) measurement latitudes. ACE-FTS and SOFIE NO observations are shown in panels (c) and (d), respectively, along with eddy GPH from SABER. The latitudes of ACE-FTS and SOFIE measurements are indicated along the right-hand side of each panel and reflect a gradual poleward migration in time of the solar occultations observed by the two satellite instruments. SOFIE maintains about a 5° latitude poleward offset from ACE-FTS, so including both instruments in this analysis provides some indication of the latitude structure. The white and black dashed contours in these plots are positive and negative eddy GPH values, respectively. Hereafter, positive (negative) eddy GPH is referred to as the PW ridge (trough). This figure gives an evaluation of both the model chemistry and dynamics.

During this time period, WACCMX + DART NO VMR is biased 18% lower than measured by ACE-FTS but only 3% lower than measured by SOFIE. However, here the focus is on the longitudinal variability rather than absolute magnitudes, and both the model and the observations show a westward traveling PW-1 pattern in NO and eddy GPH. The PW in SABER eddy GPH peaks on January 24 with amplitudes of 3,096 and 2,723 m at the ACE-FTS and SOFIE measurement latitudes, respectively. This traveling PW is also present at 62.5°N at 80 and 50 km (Iida et al., 2014; see their Figure 6), with maximum amplitudes of 2,200 and 1,400 m, respectively. On January 26, the day shown in Figure 3, highest model NO is in the 270°–360° longitude sector located over the Atlantic. This figure illustrates that this PW-1 pattern then travels westward in time. The westward migration is most evident from January 24 to 29, during which the PW travels ~180° of longitude; thus, it has a period of ~10 days, in agreement with the analysis of MF radar meridional wind data at 69°N and 85 km (Matthias et al., 2012). Such a westward-propagating PW-1 with a period of about 10 days has also been found in WACCM composites (Limpasuvan et al., 2016) and case studies (Orsolini et al., 2017) of other SSW events with elevated stratopauses. In both the model and in the observations, there is coordinated westward movement of high NO in the PW trough (green colors follow the black dashed contours) and extremely low NO remains coincident with the PW ridge (black and purple colors follow the white contours). There are subtle differences between the model and the observations, such as the larger amplitude PW in model GPH (contours, top panels) compared to SABER (contours, bottom panels), and the highest ACE-FTS and SOFIE NO VMRs are not always coincident with the lowest GPH values, as they are in the model. Over this 5-day period, LCS calculations (not shown) indicate that air parcel trajectories that originate inside the PW trough remain confined to the PW trough. These results demonstrate that PWs drive large zonal asymmetries in the distribution of NO near the polar winter mesopause.

6. Descent of NO Enhanced in the PW Trough

Next, we examine model NO VMR within two populations: the PW ridge and the PW trough. This analysis is similar to previous studies that separated trace gas measurements based on whether they were located inside or outside the polar vortex (e.g., Abrams et al., 1996; Lossow et al., 2009; Nassar et al., 2005; Siskind et al., 2000). These studies found distinctly different tracer-tracer relationships and different rates of descent

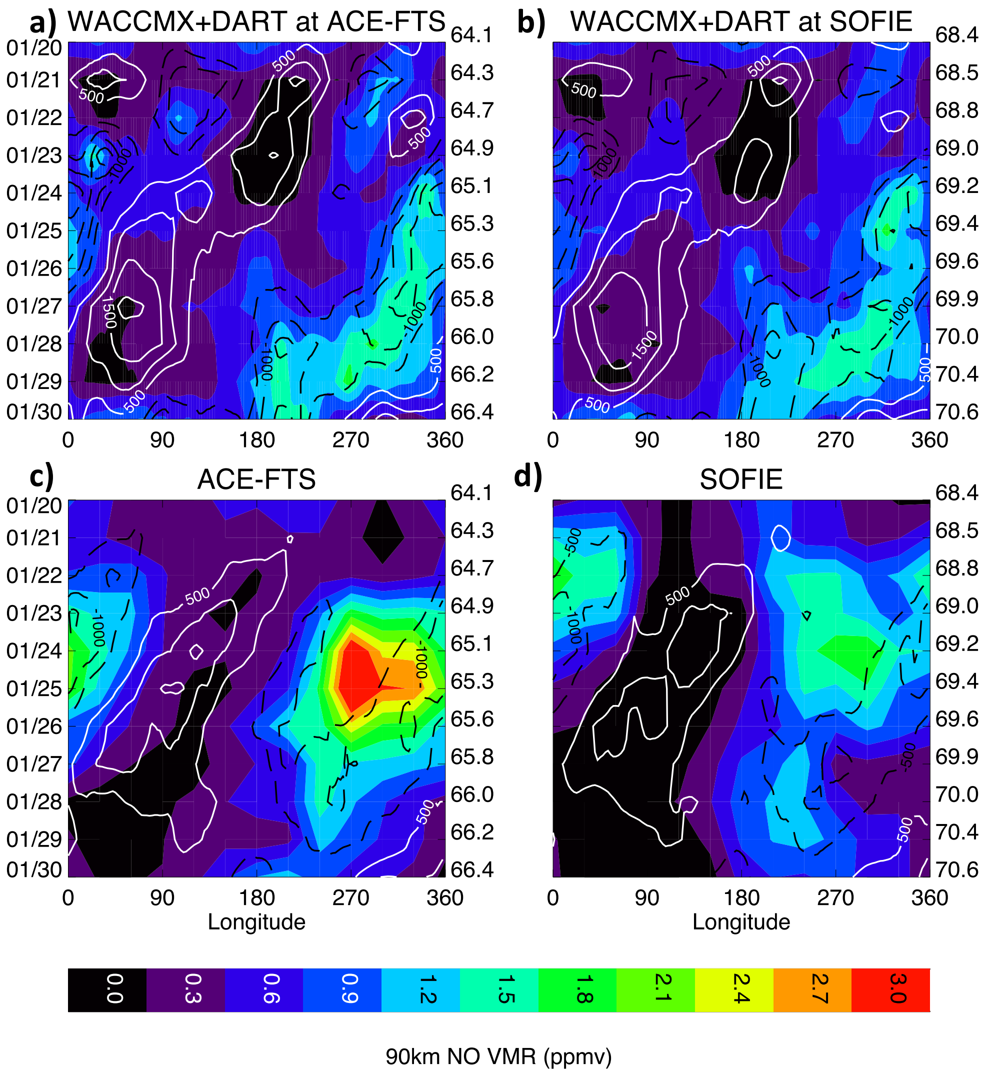

Figure 4. Longitude-time Hovmöller diagrams from January 20 to 30, 2009 of 0.001 hPa NO VMR (in color) and the deviation of GPH from the zonal mean where positive values in white indicate PW ridges and negative values in black dashed indicate PW troughs. GPH data is from WACCMX + DART (top) and SABER (bottom). The top panels show NO VMR in WACCMX + DART at the (a) ACE-FTS and (b) SOFIE measurement latitudes. The bottom panels are NO VMR measured by (c) ACE-FTS and (d) SOFIE. The ACE-FTS and SOFIE measurement latitudes are given along the right side of panels in the left and right columns, respectively. GPH, geopotential height; NH, Northern Hemisphere; PW, planetary wave; VMR, volume mixing ratio.

in different air mass types. The goal here is to determine whether descent rates in the upper mesosphere depend on longitude as defined by PW phase. Thus, on each day from January 24 to 29, we categorize the model grid points (at the SOFIE latitudes shown in Figure 4) by PW phase. One category consists of grid points located in the PW ridge (with positive eddy GPH values) and the other category consists of grid points located in the PW trough (with negative eddy GPH values). On each day we calculate daily mean NO profiles from WACCMX + DART in both air mass types.

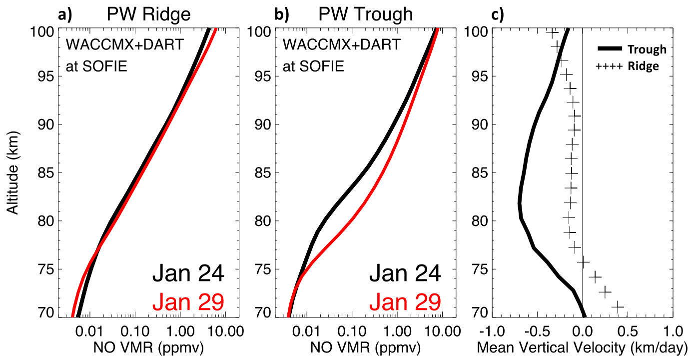

Figure 5. Daily average WACCMX + DART NO VMR profiles on January 24 (black) and January 29 (red) at the SOFIE measurement latitudes and located in the PW (a) ridge and (b) trough. Panel (c) gives vertical profiles of derived vertical velocities in the PW ridge (plus signs) and trough (solid line) of the planetary wave. Negative values indicate descent. PW, planetary wave.

Figure 5a (left panel) shows daily average WACCMX + DART NO profiles on January 24 (black) and January 29 (red) in the PW ridge. Figure 5b shows daily average NO profiles on the same days but in the PW trough. It is clear that there are much larger temporal differences in the NO profiles in the trough than in the ridge. Descent rates are inferred based on the vertical displacement of the NO profiles. This method to infer descent rates has been widely used in previous study (Bailey et al., 2014; Hendrickx et al., 2015; Kvissel et al., 2012; Lee et al., 2011; Siskind et al., 2015; Straub et al., 2012). This technique is valid here since (1) geomagnetic indices are low and we can assume negligible NO production due to particle precipitation; (2) chemical loss of NO is insignificant at latitudes near-polar night, that is, polar NO is mainly controlled by dynamics (Salmi et al., 2011); (3) tidally driven vertical motions are likely negligible given diurnal and semidiurnal migrating tidal amplitudes that are less than 0.5K at 90 km poleward of 40°N (Sassi et al., 2013). Further, Orsolini et al. (2017) demonstrated that the tidal contribution from migrating tides to the vertical component of the residual circulation is small compared to the dominant PW-1 contribution after SSW onset (see their Figure 9).

Figure 5c shows daily average profiles of derived descent rates in the PW ridge and trough. These results indicate that, between 80 and 90 km, the 5-day average descent rate in the PW trough is a factor of 5 stronger than in the PW ridge (−0.64 compared to −0.13 km/day). The same procedure applied to profiles of atomic oxygen (not shown) yields similar results (−0.65 km/day in the trough vs. −0.15 km/day in the ridge). That the derived descent rates based on NO and O profiles are similar lends confidence that they represent the "true" rates of descent (Ryan et al., 2018). These results are consistent with Shepherd et al. (2010) who reported "a dramatic influx of atomic oxygen from the thermosphere" over this same 5-day period at Eureka (80°N, 86°W), which is also located in the PW trough.

In terms of the processes responsible for the descent, Meraner and Schmidt (2016) used HAMMONIA to quantify the role of advective and diffusive processes in the downward transport of NO_x during 2009. They found that large-scale advection is responsible for most of the NO transport from the thermosphere to the mesosphere during this SSW. This is consistent with the results of Smith et al. (2010), who showed that high temperatures coincident with elevated atomic oxygen abundances are indicators of descent driven by large-scale advection. They add that there is also likely a component of the descent driven by molecular diffusion, which is enhanced where it is warmer. Regardless of the driving mechanism(s), we conclude that 83% ($100 \times 0.64/(0.64 + 0.13)$) of all NO descent from 80 to 90 km in late January of 2009 occurred in the longitude sector of the PW trough (assuming from Figure 4 that the ridge and trough occupy comparable areas). This is the case in the model and is confirmed when the ACE-FTS and SOFIE observations are separated in the same way (not shown). Thus, we conclude that zonal asymmetries should be considered when comparing models of NO descent with observations.

7. Conclusions

This work used WACCMX + DART to show that the January 2009 split Arctic vortex in the stratosphere left an imprint on the horizontal distribution of NO at the mesopause. We then presented an 11-day case study in late January during the recovery phase of the 2009 SSW. During the short period of time between the onset of the warming in the stratosphere and the formation of the elevated stratopause around 80–90 km altitude about 10 days later, the reforming mesospheric vortex extends up into the MLT region. The vortex edge in this region is defined not by potential vorticity but by FTLE ridges. We showed for the first time the effects of LCSs on the horizontal transport of NO. We then demonstrate that, near 90 km, LCSs appear in the flow over the north Atlantic in the vicinity of a trough of a westward traveling 10-day PW. This trough is coincident with a region of elevated NO at 90 km, and both the PW trough and elevated NO are located directly above the westward tilting polar vortex in the stratosphere and mesosphere. Because the vortex extends all the way up into the MLT, downward transport from the thermosphere to the upper mesosphere is possible and takes place in this region. Enhanced descent in the PW trough and inhibited horizontal transport of NO by the LCS comprise an efficient transport pathway for air to enter the top of the polar vortex. That is, following the 2009 SSW, air descended over the north Atlantic and Canadian longitude sectors rather than, as is often assumed, descending uniformly in longitude.

New science results are as follows:

1) The split stratospheric polar vortex "imprints" on the spatial distribution of model NO VMR at the mesopause.
2) Elevated NO VMR values in the upper mesosphere remain horizontally confined to high latitudes by LCSs for 11 days.
3) The LCSs occur in the vicinity of the trough of a 10-day westward traveling PW-1.
4) From January 24 to 29, 2009 descent in the upper mesosphere (from ~75 to 95 km) is five times stronger in the longitude sector of the PW trough than in the PW ridge.
5) The descent is likely driven by large-scale vertical advection; that is, most of the residual circulation vertical velocity, a zonally averaged quantity by definition, is focused in the longitude sector of the PW trough.

Future work will quantify how often LCSs coincide with traveling PW troughs at the polar winter mesopause and how often descent depends on PW phase. In particular, this work sets the stage for broader studies that seek to determine whether mesospheric dynamics drive zonal asymmetries in NO descent during more typical polar vortex conditions and in the Southern Hemisphere.

Data Availability Statement

High-end computing resources were provided by NASA to run WACCMX + DART on the Pleiades supercomputer at the NASA Ames research center. Model output for January 20–30, 2009 at 0.001 hPa are provided at https://zenodo.org/record/4563306#.YDhpgeBlDxs. SABER data are available at saber.gats-inc.com. SOFIE data are available at https://spdf.gsfc.nasa.gov/pub/data/aim/sofie/. ACE-FTS data are available at https://databace.scisat.ca/level2/. MERRA-2 data are available at the Data and Information Services Center, managed by the NASA Goddard Earth Sciences (GES) at https://gmao.gsfc.nasa.gov/reanalysis/. The authors acknowledge the use of SuperDARN data. The SuperDARN data are available from Virginia Tech at vt.superdarn.org.

Acknowledgments
V. Lynn Harvey, Seebany Datta-Barua, Nicholas M. Pedatella, and Ningchao Wang acknowledge support from NASA Heliophysics Supporting Research Grant 80NSSC18K1046. V. Lynn Harvey acknowledges partial support from NASA Heliophysics Guest Investigator Grants NNX17AB80G and 80NSSC19K0262. Cora E. Randall acknowledges NSF Grant AGS 1651428. David E. Siskind acknowledges support as a co-investigator of the NASA TIMED/SABER project. Willem E. van Caspel is partly supported by the Research Council of Norway/CoE under contract 22352/F50. These results are partly based upon work supported by the National Center for Atmospheric Research, which is a major facility sponsored by the National Science Foundation under Cooperative Agreement no. 1852977.

References

Abrams, M. C., Manney, G. L., Gunson, M. R., Abbas, M. M., Chang, A. Y., Goldman, A., et al. (1996). Trace gas transport in the Arctic Vortex inferred from ATMOS ATLAS-2 observations during April 1993. *Geophysical Research Letters*, *23*(17), 2345–2348. https://doi.org/10.1029/96GL00704

Anderson, J. L. (2001). An ensemble adjustment Kalman filter for data assimilation. *Monthly Weather Review*, *129*, 2884–2903. https://doi.org/10.1175/1520-0493(2001)129<2884:AEAKFF>2.0.CO;2

Andersson, M. E., Verronen, P. T., Marsh, D. R., Päivärinta, S.-M., & Plane, J. M. C. (2016). WACCM-D-Improved modeling of nitric acid and active chlorine during energetic particle precipitation. *Journal of Geophysical Research - D: Atmospheres*, *121*, 328–410. https://doi.org/10.1002/2015jd024173

Andrews, D. G., Holton, J. R., & Leovy, C. B. (1987). *Middle atmosphere dynamics*. Academic Press.

Bailey, S. M., Thurairajah, B., Randall, C. E., Holt, L., Siskind, D. E., Harvey, V. L., et al. (2014). A multi tracer analysis of thermosphere to stratosphere descent triggered by the 2013 Stratospheric Sudden Warming. *Geophysical Research Letters*, *41*, 5216–5222. https://doi.org/10.1002/2014GL059860

Baldwin, M. P., Ayarzagüena, B., Birner, T., Butchart, N., Butler, A. H., Charlton-Perez, A. J., et al. (2021). Sudden stratospheric warmings. *Reviews of Geophysics*, *59*, e2020RG000708. https://doi.org/10.1029/2020RG000708

Baumgaertner, A. J. G., Seppälä, A., Jöckel, P., & Clilverd, M. A. (2011). Geomagnetic activity related NOx enhancements and polar surface air temperature variability in a chemistry climate model: Modulation of the NAM index. *Atmospheric Chemistry and Physics*, *11*, 4521–4531. https://doi.org/10.5194/acp-11-4521-2011

Bender, S., Sinnhuber, M., Espy, P. J., & Burrows, J. P. (2019). Mesospheric nitric oxide model from SCIAMACHY data. *Atmospheric Chemistry and Physics*, *19*, 2135–2147. https://doi.org/10.5194/acp-19-2135-2019

Bernath, P. F., McElroy, C. T., Abrams, M. C., Boone, C. D., Butler, M., Camy-Peyret, C., & Zou, J. (2005). Atmospheric chemistry experiment (ACE): Mission overview. *Geophysical Research Letters*, *32*, L15S01. https://doi.org/10.1029/2005GL022386

Bhattacharya, Y., & Gerrard, A. J. (2010). Correlations of mesospheric winds with subtle motion of the Arctic polar vortex. *Atmospheric Chemistry and Physics*, *10*, 431–436. https://doi.org/10.5194/acp-10-431-2010

Boone, C. D., Walker, K. A., & Bernath, P. F. (2013). Version 3 retrievals for the Atmospheric Chemistry Experiment Fourier Transform Spectrometer (ACE–FTS). In P. F. Bernath (Ed.), *The atmospheric chemistry experiment ACE at 10: A solar occultation anthology* (pp. 103–127). A. Deepak Publishing.

Bosilovich, M., Akella, S., Coy, L., Cullather, R., Draper, C., Gelaro, R., & Suarez, M. (2015). MERRA-2: Initial Evaluation of the Climate, NASA Tech. Rep. Series on Global Modeling and Data Assimilation. NASA/TM–2015-104606, *43*.

Bowman, K. P. (1993). Large-scale isentropic mixing properties of the Antarctic polar vortex from analyzed winds, *Journal of Geophysical Research*, *98*(D12), 23013–23027, https://doi.org/10.1029/93JD02599

Brasseur, G. P., & Solomon, S. C. (2005). Aeronomy of the middle atmosphere: Chemistry and physics of the stratosphere, in Atmospheric and Oceanographic Sciences Library. Dynamics and transport (3rd ed., Vol. 32, pp. 51–149). Springer.

Butler, A. H., Sjoberg, J. P., Seidel, D. J., & Rosenlof, K. H. (2017). A sudden stratospheric warming compendium. *Earth System Science Data*, *9*, 63–76. https://doi.org/10.5194/essd-9-63-2017

Callaghan, P. F., & Salby, M. L. (2002). Three-dimensionality and forcing of the Brewer-Dobson circulation. *Journal of the Atmospheric Sciences*, *59*, 976–991. https://doi.org/10.1175/1520-0469(2002)059<0976:TDAFOT>2.0.CO;2

Chau, J. L., Hoffmann, P., Pedatella, N. M., Matthias, V., & Stober, G. (2015). Upper mesospheric lunar tides over middle and high latitudes during sudden stratospheric warming events. *Journal of Geophysical Research: Space Physics*, *120*, 3084–3096. https://doi.org/10.1002/2015JA020998

Chisham, G. (2018). Calibrating SuperDARN interferometers using meteor backscatter. *Radio Science*, *53*(6), 761–774. https://doi.org/10.1029/2017rs006492

Chisham, G., & Freeman, M. P. (2013). A reassessment of SuperDARN meteor echoes from the upper mesosphere and lower thermosphere. *Journal of Atmospheric and Solar-Terrestrial Physics*, *102*, 207–221. https://doi.org/10.1016/j.jastp.2013.05.018

Coy, L., Eckermann, S. D., Hoppel, K. W., & Sassi, F. (2011). Mesospheric precursors to the major stratospheric sudden warming of 2009: Validation and dynamical attribution using a ground-to-edge-of-space data assimilation system. *Journal of Advances in Modeling Earth Systems*, *3*, M10002. https://doi.org/10.1029/2011MS000067

Curbelo, J., García-Garrido, V. J., Mechoso, C. R., Mancho, A. M., Wiggins, S., & Niang, C. (2017). Insights into the three-dimensional Lagrangian geometry of the Antarctic polar vortex. *Nonlinear Processes in Geophysics*, *24*, 379–392. https://doi.org/10.5194/npg-24-379-2017

Dawkins, E. C. M., Feofilov, A., Rezac, L., Kutepov, A. A., Janches, D., Höffner, J., et al. (2018). Validation of SABER v2.0 operational temperature data with ground-based lidars in the mesosphere-lower thermosphere region (75-105 km). *Journal of Geophysical Research - D: Atmospheres*, *123*, 9916–9934. https://doi.org/10.1029/2018JD028742

de la Cámara, A., Mancho, A. M., Ide, K., Serrano, E., & Mechoso, C. R. (2012). Routes of transport across the Antarctic polar vortex in the southern spring. *Journal of the Atmospheric Sciences*, *69*(2), 741–752. https://doi.org/10.1175/JAS-D-11-0142.1

Demirhan Bari, D., Gabriel, A., Körnich, H., & Peters, D. W. H. (2013). The effect of zonal asymmetries in the Brewer-Dobson circulation on ozone and water vapor distributions in the northern middle atmosphere. *Journal of Geophysical Research - D: Atmospheres*, *118*, 3447–3466. https://doi.org/10.1029/2012JD017709

du Toit, P. C., & Marsden, J. E. (2010). Horseshoes in hurricanes. *Journal of Fixed Point Theory and Applications*, *7*(2), 351–384. https://doi.org/10.1007/s11784-010-0028-6

Fisher, M., O'Neill, A., & Sutton, R. (1993). Rapid descent of mesospheric air into the stratospheric polar vortex. *Geophysical Research Letters*, *20*(12), 1267–1270. https://doi.org/10.1029/93GL01104

Funke, B., Ball, W., Bender, S., Gardini, A., Harvey, V. L., Lambert, A., et al. (2017). HEPPA-II model-measurement intercomparison project: EPP indirect effects during the dynamically perturbed NH winter 2008-2009. *Atmospheric Chemistry and Physics*, *17*, 3573–3604. https://doi.org/10.5194/acp-17-3573-2017

Garcia, R. R., López-Puertas, M., Funke, B., Marsh, D. R., Kinnison, D. E., Smith, A. K., & González-Galindo, F. (2014). On the distribution of CO_2 and CO in the mesosphere and lower thermosphere. *Journal of Geophysical Research - D: Atmospheres*, *119*, 5700–5718. https://doi.org/10.1002/2013JD021208

Garcia, R. R., Marsh, D. R., Kinnison, D. E., Boville, B. A., & Sassi, F. (2007). Simulation of secular trends in the middle atmosphere, 1950-2003. *Journal of Geophysical Research*, *112*, D09301. https://doi.org/10.1029/2006JD007485

Garcia, R. R. & Solomon, S. (1994). A new numerical model of the middle atmosphere: 2. Ozone and related species. *Journal of Geophysical Research*, *99*, 12937–12951. https://doi.org/10.1029/94JD00725

García-Comas, M., López-Puertas, M., Marshall, B. T., Wintersteiner, P. P., Funke, B., Bermejo-Pantaleón, D., et al. (2008). Errors in Sounding of the Atmosphere using Broadband Emission Radiometry (SABER) kinetic temperature caused by non-local-thermodynamic-equilibrium model parameters. *Journal of Geophysical Research*, *113*, D24106. https://doi.org/10.1029/2008JD010105

Gelaro, R., McCarty, W., Suárez, M. J., Todling, R., Molod, A., Takacs, L., et al. (2017). The modern-era retrospective analysis for research and applications, version 2 (MERRA-2). *Journal of Climate*, *30*, 5419–5454. https://doi.org/10.1175/JCLI-D-16-0758.1

Global Modeling and Assimilation Office. (2015). MERRA-2 inst6_3d_ana_Nv: 3d, 6-hourly, instantaneous, model-level, analysis, analyzed meteorological fields V5.12.4. Goddard Earth Sciences Data and Information Services Center (GES DISC). https://doi.org/10.5067/IUUF4WB9FT4W Accessed 2017.

Goncharenko, L. P., Chau, J. L., Liu, H.-L., & Coster, A. J. (2010). Unexpected connections between the stratosphere and ionosphere. *Geophysical Research Letters*, *37*, L10101. https://doi.org/10.1029/2010GL043125

Goncharenko, L. P., Coster, A. J., Chau, J. L., & Valladares, C. E. (2010). Impact of sudden stratospheric warmings on equatorial ionization anomaly. *Journal of Geophysical Research*, *115*, A00G07. https://doi.org/10.1029/2010JA015400

Gordley, L. L., Hervig, M. E., Fish, C., Russell, J. M. S., III, Cook, J., et al. (2009). The solar occultation for ice experiment. *Journal of Atmospheric and Solar-Terrestrial Physics*, *71*, 300–315. https://doi.org/10.1016/j.jastp.2008.07.012

Hall, G. E., MacDougall, J. W., Moorcroft, D. R., St-Maurice, J. P., Manson, A. H., & Meek, C. E. (1997). Super dual auroral radar network observations of meteor echoes. *Journal of Geophysical Research*, *102*, 14603–14614. https://doi.org/10.1029/97JA00517

Haller, G. (2015). Lagrangian coherent structures. *Annual Review of Fluid Mechanics*, *47*, 137–162. https://doi.org/10.1146/annurev-fluid-010313-141322

Harada, Y., Goto, A., Hasegawa, H., Fujikawa, N., Naoe, H., & Hirooka, T. (2010). A major stratospheric sudden warming event in January 2009. *Journal of the Atmospheric Sciences*, *67*, 2052–2069. https://doi.org/10.1175/2009JAS3320.1

Harvey, V. L., Pierce, R. B., Fairlie, T. D., & Hitchman, M. H. (2002). A climatology of stratospheric polar vortices and anticyclones. *Journal of Geophysical Research*, *107*. https://doi.org/10.1029/2001JD001471

Harvey, V. L., Randall, C. E., Goncharenko, L. P., Becker, E., & France, J. A. (2018). On the upward extension of the polar vortices into the mesosphere. *Journal of Geophysical Research - D: Atmospheres*. 123(17), 9171–9191. https://doi.org/10.1020/2018JD028815

Hauchecorne, A., Bertaux, J.-L., Dalaudier, F., Russell, J. M., III, Mlynczak, M. G., Kyrölä, E., & Fussen, D. (2007). Large increase of NO_2 in the north polar mesosphere in January-February 2004: Evidence of a dynamical origin from GOMOS/ENVISAT and SABER/TIMED data. *Geophysical Research Letters*, *34*, L03810. https://doi.org/10.1029/2006GL027628

He, M., Chau, J. L., Stober, G., Hall, C. M., Tsutsumi, M., & Hoffmann, P. (2017), Application of Manley-Rowe relation in analyzing nonlinear interactions between planetary waves and the solar semidiurnal tide during 2009 Sudden Stratospheric Warming event. *Journal of Geophysical Research: Space Physics*, *122*, 10783–10795, https://doi.org/10.1002/2017JA024630

Heelis, R. A., Lowell, J. K., & Spiro, R. W. (1982). A model of the high-latitude ionospheric convection pattern. *Journal of Geophysical Research*, *87*, 6339–6345. https://doi.org/10.1029/JA087iA08p06339

Hendrickx, K., Megner, L., Gumbel, J., Siskind, D. E., Orsolini, Y. J., Tyssøy, H. N., & Hervig, M. (2015). Observation of 27 day solar cycles in the production and mesospheric descent of EPP-produced NO. *Journal of Geophysical Research: Space Physics*, *120*, 8978–8988. https://doi.org/10.1002/2015JA021441

Hervig, M. E., Marshall, B. T., Bailey, S. M., Siskind, D. E., Russell, III, J. M., III, Bardeen, C. G., et al. (2019). Validation of Solar Occultation for Ice Experiment (SOFIE) nitric oxide measurements. *Atmospheric Measurement Techniques*, *12*, 3111–3121. https://doi.org/10.5194/amt-12-3111-2019

Hibbins, R. E., Freeman, M. P., Milan, S. E., & Ruohoniemi, J. M. (2011). Winds and tides in the mid-latitude Southern Hemisphere upper mesosphere recorded with the Falkland Islands SuperDARN radar. *Annales Geophysicae*, *29*(11), 1985–1996. https://doi.org/10.5194/angeo-29-1985-2011

Hibbins, R. E., & Jarvis, M. J. (2008). A long-term comparison of wind and tide measurements in the upper mesosphere recorded with an imaging Doppler interferometer and SuperDARN radar at Halley, Antarctica. *Atmospheric Chemistry and Physics*, *8*(5), 1367–1376. https://doi.org/10.5194/acp-8-1367-2008

Iida, C., Hirooka, T., & Eguchi, N. (2014). Circulation changes in the stratosphere and mesosphere during the stratospheric sudden warming event in January 2009. *Journal of Geophysical Research - D: Atmospheres*, *119*(12), 7104–7115. https://doi.org/10.1002/2013JD021252

Jin, H., Miyoshi, Y., Pancheva, D., Mukhtarov, P., Fujiwara, H., & Shinagawa, H. (2012). Response of migrating tides to the stratospheric sudden warming in 2009 and their effects on the ionosphere studied by a whole atmosphere-ionosphere model GAIA with COSMIC and TIMED/SABER observations. *Journal of Geophysical Research*, *117*, A10323. https://doi.org/10.1029/2012JA017650

Kinoshita, T., Tomikawa, Y., & Sato, K. (2010). On the three-dimensional residual mean circulation and wave activity flux of the primitive equations. *Journal of the Meteorological Society of Japan*, *88*, 373–394. https://doi.org/10.2151/jmsj.2010-307

Kvissel, O.-K., Orsolini, Y. J., Stordal, F., Limpasuvan, V., Richter, J., & Marsh, D. R. (2012). Mesospheric intrusion and anomalous chemistry during and after a major stratospheric sudden warming. *Journal of Atmospheric and Solar-Terrestrial Physics*, *78–79*, 116–124. https://doi.org/10.1016/j.jastp.2011.08.015

Labitzke, K. (1972). Temperature changes in the mesosphere and stratosphere connected with circulation changes in winter. *Journal of the Atmospheric Sciences*, *29*, 756–766. https://doi.org/10.1175/1520-0469(1972)029<0756:TCITMA>2.0.CO;2

Lee, J. N., Wu, D. L., Manney, G. L., Schwartz, M. J., Lambert, A., Livesey, N. J., et al. (2011). Aura Microwave Limb Sounder observations of the polar middle atmosphere: Dynamics and transport of CO and H_2O. *Journal of Geophysical Research*, *116*, D05110. https://doi.org/10.1029/2010JD014608

Limpasuvan, V., Orsolini, Y. J., Chandran, A., Garcia, R. R., & Smith, A. K. (2016). On the composite response of the MLT to major sudden stratospheric warming events with elevated stratopause. *Journal of Geophysical Research - D: Atmospheres*, *121*, 4518–4537. https://doi.org/10.1002/2015JD024401

Liu, H.-L., Doornbos, E., Yamamoto, M., & Tulasi Ram, S. (2011). Strong thermospheric cooling during the 2009 major stratosphere warming. *Geophysical Research Letters*, *38*, L12102. https://doi.org/10.1029/2011GL047898

Liu, H.-L., Foster, B. T., Hagan, M. E., McInerney, J. M., Maute, A., Qian, L., et al. (2010). Thermosphere extension of the Whole Atmosphere Community Climate Model. *Journal of Geophysical Research*, *115*, A12302. https://doi.org/10.1029/2010JA015586

Lossow, S., Khaplanov, M., Gumbel, J., Stegman, J., Witt, G., Dalin, P., et al. (2009). Middle atmospheric water vapour and dynamics in the vicinity of the polar vortex during the Hygrosonde-2 campaign. *Atmospheric Chemistry and Physics*, *9*, 4407–4417. https://doi.org/10.5194/acp-9-4407-2009

Madrid, J. A. J., & Mancho, A. M. (2009). Distinguished trajectories in time dependent vector fields. *Chaos*, *19*, 013111. https://doi.org/10.1063/1.3056050

Manney, G. L., Schwartz, M. J., Krüger, K., Santee, M. L., Pawson, S., Lee, J. N., et al. (2009). Aura Microwave Limb Sounder observations of dynamics and transport during the record-breaking 2009 Arctic stratospheric major warming. *Geophysical Research Letters*, *36*, L12815. https://doi.org/10.1029/2009GL038586

Manney, G. L., Zurek, R. W., O'Neill, A., & Swinbank, R. (1994). On the motion of air through the stratospheric polar vortex. *Journal of the Atmospheric Sciences*, *51*, 2973–2994. https://doi.org/10.1175/1520-0469(1994)051<2973:OTMOAT>2.0.CO;2

Marshall, B. T., Deaver, L. E., Thompson, R. E., Gordley, L. L., McHugh, M. J., Hervig, M. E., & Russell, J. M., III (2011). Retrieval of temperature and pressure using broadband solar occultation: SOFIE approach and results. *Atmospheric Measurement Techniques*, *4*, 893–907. https://doi.org/10.5194/amt-4-893-2011

Matsuno, T. (1970). Vertical propagation of stationary planetary waves in the winter Northern Hemisphere. *Journal of the Atmospheric Sciences*, *27*(6), 871–883. https://doi.org/10.1175/1520-0469(1970)027<0871:VPOSPW>2.0.CO;2

Matthias, V., Hoffmann, P., Rapp, M., & Baumgarten, G. (2012). Composite analysis of the temporal development of waves in the polar MLT region during stratospheric warmings. *Journal of Atmospheric and Solar-Terrestrial Physics*, *90–91*, 86–96. https://doi.org/10.1016/j.jastp.2012.04.004

McLandress, C., Scinocca, J. F., Shepherd, T. G., Reader, M. C., & Manney, G. L. (2013). Dynamical control of the mesosphere by orographic and nonorographic gravity wave drag during the extended northern winters of 2006 and 2009. *Journal of the Atmospheric Sciences*, *70*(7), 2152–2169. https://doi.org/10.1175/JAS-D-12-0297.1

Meraner, K., & Schmidt, H. (2016). Transport of nitrogen oxides through the winter mesopause in HAMMONIA. *Journal of Geophysical Research - D: Atmospheres*, *121*, 2556–2570. https://doi.org/10.1002/2015JD024136

Meraner, K., Schmidt, H., Manzini, E., Funke, B., & Gardini, A. (2016). Transport of nitrogen oxides through the winter mesopause in HAMMONIA. *Journal of Geophysical Research - D: Atmospheres*, *121*(20), 2556–2570. https://doi.org/10.1002/2015JD024136

Minschwaner, K., & Siskind, D. E. (1993). A new calculation of nitric oxide photolysis in the stratosphere, mesosphere, and lower thermosphere. *Journal of Geophysical Research*, *98*(D11), 20401–20412. https://doi.org/10.1029/93JD02007

Molod, A., Takacs, L., Suarez, M., & Bacmeister, J. (2015). Development of the GEOS-5 atmospheric general circulation model: Evolution from MERRA to MERRA2. *Geoscientific Model Development*, *8*, 1339–1356. https://doi.org/10.5194/gmd-8-1339-2015

Nassar, R., Bernath, P. F., Boone, C. D., Manney, G. L., McLeod, S. D., Rinsland, C. P., et al. (2005). ACE-FTS measurements across the edge of the winter 2004 Arctic vortex. *Geophysical Research Letters*, *32*, L15S05. https://doi.org/10.1029/2005GL022671

Natarajan, M., Remsberg, E. E., Deaver, L. E., & Russell, J. M., III (2004). Anomalously high levels of NOx in the polar upper stratosphere during April, 2004: Photochemical consistency of HALOE observations. *Geophysical Research Letters*, *31*. https://doi.org/10.1029/2004GL020566

Newnham, D. A., Rodger, C. J., Marsh, D. R., Hervig, M. E., & Clilverd, M. A. (2020). Spatial distributions of nitric oxide in the Antarctic wintertime middle atmosphere during geomagnetic storms, *Journal of Geophysical Research: Space Physics*, *125*, e2020JA027846. https://doi.org/10.1029/2020JA027846

Orsolini, Y. J., Limpasuvan, V., Pérot, K., Espy, P., Hibbins, R., Lossow, S., et al. (2017). Modelling the descent of nitric oxide during the elevated stratopause event of January 2013. *Journal of Atmospheric and Solar-Terrestrial Physics*, *155*(2017), 50–61. https://doi.org/10.1016/j.jastp.2017.01.006

Päivärinta, S.-M., Verronen, P. T., Funke, B., Gardini, A., Seppälä, A., & Andersson, M. E. (2016). Transport versus energetic particle precipitation: Northern polar stratospheric NOx and ozone in January-March 2012. *Journal of Geophysical Research - D: Atmospheres*, *121*, 6085–6100. https://doi.org/10.1002/2015JD024217

Pancheva, D., & Mukhtarov, P. (2012). Planetary wave coupling of the atmosphere-ionosphere system during the Northern winter of 2008/2009. *Advances in Space Research*, *50*(9), 1189–1203. https://doi.org/10.1016/j.asr.2012.06.023

Pedatella, N. M., Fang, T.-W., Jin, H., Sassi, F., Schmidt, H., Chau, J. L., et al. (2016). Multimodel comparison of the ionosphere variability during the 2009 sudden stratosphere warming. *Journal of Geophysical Research: Space Physics*, *121*(7), 7204–7225. https://doi.org/10.1002/2016JA022859

Pedatella, N. M., Liu, H.-L., Marsh, D. R., Raeder, K., Anderson, J. L., Chau, J. L., et al. (2018). Analysis and Hindcast experiments of the 2009 Sudden Stratospheric Warming in WACCMX+DART. *Journal of Geophysical Research: Space Physics*, *123*(4), 3131–3153. https://doi.org/10.1002/2017JA025107

Pedatella, N. M., Liu, H.-L., Sassi, F., Lei, J., Chau, J. L., & Zhang, X. (2014). Ionosphere variability during the 2009 SSW: Influence of the lunar semidiurnal tide and mechanisms producing electron density variability. *Journal of Geophysical Research: Space Physics*, *119*, 3828–3843. https://doi.org/10.1002/2014JA019849

Pedatella, N. M., Raeder, K., Anderson, J. L., & Liu, H.-L. (2013). Application of data assimilation in the Whole Atmosphere Community Climate Model to the study of day-to-day variability in the middle and upper atmosphere. *Geophysical Research Letters*, *40*, 4469–4474. https://doi.org/10.1002/grl.50884

Pedatella, N. M., Raeder, K., Anderson, J. L., & Liu, H.-L. (2014). Ensemble data assimilation in the Whole Atmosphere Community Climate Model. *Journal of Geophysical Research - D: Atmospheres*, *119*, 9793–9809. https://doi.org/10.1002/2014JD021776

Pérot, K., & Orsolini, Y. J. (2021). Impact of the major SSWs of February 2018 and January 2019 on the middle atmospheric nitric oxide abundance. *Journal of Atmospheric and Solar-Terrestrial Physics*, *218*, 105586. https://doi.org/10.1016/j.jastp.2021.105586

Pérot, K., Urban, J., & Murtagh, D. P. (2014). Unusually strong nitric oxide descent in the Arctic middle atmosphere in early 2013 as observed by Odin/SMR. *Atmospheric Chemistry and Physics*, *14*(15), 8009–8015. https://doi.org/10.5194/acp-14-8009-2014

Pettit, J. M., Randall, C. E., Peck, E. D., Marsh, D. R., Kamp, M., Fang, X., et al. (2019). Atmospheric effects of >30-kev energetic electron precipitation in the Southern Hemisphere winter during 2003. *Journal of Geophysical Research: Space Physics*, *124*, 8138–8153. https://doi.org/10.1029/2019JA026868

Pierce, R. B., & Fairlie, T. D. A. (1993). Chaotic advection in the stratosphere: Implications for the dispersal of chemically perturbed air from the polar vortex. *Journal of Geophysical Research*, *98*, 18589–18595. https://doi.org/10.1029/93JD01619

Randall, C. E., Harvey, V. L., Holt, L. A., Marsh, D. R., Kinnison, D., Funke, B., & Bernath, P. F. (2015). Simulation of energetic particle precipitation effects during the 2003-2004 Arctic winter. *Journal of Geophysical Research: Space Physics*, *120*, 5035–5048. https://doi.org/10.1002/2015JA021196

Randall, C. E., Harvey, V. L., Manney, G. L., Orsolini, Y., Codrescu, M., Sioris, C., et al. (2005). Stratospheric effects of energetic particle precipitation in 2003-2004. *Geophysical Research Letters*, *32*, L05802. https://doi.org/10.1029/2004GL022003

Randall, C. E., Harvey, V. L., Singleton, C. S., Bailey, S. M., Bernath, P. F., Codrescu, M., et al. (2007). Energetic particle precipitation effects on the Southern Hemisphere stratosphere in 1992-2005. *Journal of Geophysical Research*, *112*, D08308. https://doi.org/10.1029/2006JD007696

Randall, C. E., Harvey, V. L., Singleton, C. S., Bernath, P. F., Boone, C. D., & Kozyra, J. U. (2006). Enhanced NOx in 2006 linked to strong upper stratospheric Arctic vortex. *Geophysical Research Letters*, *33*, L18811. https://doi.org/10.1029/2006GL027160

Randall, C. E., Harvey, V. L., Siskind, D. E., France, J., Bernath, P. F., Boone, C. D., & Walker, K. A. (2009). NOx descent in the Arctic middle atmosphere in early 2009. *Geophysical Research Letters*, *36*, L18811. https://doi.org/10.1029/2009GL039706

Randall, C. E., Rusch, D. W., Bevilacqua, R. M., Hoppel, K. W., & Lumpe, J. D. (1998). Polar Ozone and Aerosol Measurement (POAM) II stratospheric NO_2, 1993-1996. *Journal of Geophysical Research*, *103*, 28361–28371. https://doi.org/10.1029/98JD02092

Reddmann, T., Ruhnke, R., Versick, S., & Kouker, W. (2010). Modeling disturbed stratospheric chemistry during solar-induced NOx enhancements observed with MIPAS/ENVISAT. *Journal of Geophysical Research*, *115*, D00I11. https://doi.org/10.1029/2009JD012569

Remsberg, E., Lingenfelser, G., Harvey, V. L., Grose, W., Russell, J., III, Mlynczak, M., et al. (2003). On the verification of the quality of SABER temperature, geopotential height, and wind fields by comparison with Met Office assimilated analyses. *Journal of Geophysical Research*, *108*. https://doi.org/10.1029/2003JD003720

Remsberg, E. E., Marshall, B. T., García-Comas, M., Krüeger, D., Lingenfelser, G. S., Martin-Torres, J., et al. (2008). Assessment of the quality of the version 1.07 temperature-versus-pressure profiles of the middle atmosphere from TIMED/SABER. *Journal of Geophysical Research*, *113*, D17101. https://doi.org/10.1029/2008JD010013

Richter, J. H., Sassi, F., & Garcia, R. R. (2010). Toward a physically based gravity wave source parameterization in a general circulation model. *Journal of the Atmospheric Sciences*, *67*, 136–156. https://doi.org/10.1175/2009JAS3112.1

Rinsland, C. P., Boone, C., Nassar, R., Walker, K., Bernath, P., McConnell, J. C., & Chiou, L. (2005). Atmospheric Chemistry Experiment (ACE) Arctic stratospheric measurements of NOx during February and March 2004: Impact of intense solar flares. *Geophysical Research Letters*, *32*, L16S05. https://doi.org/10.1029/2005GL022425

Roble, R. G., & Ridley, E. C. (1987). An auroral model for the NCAR thermospheric general circulation model (TGCM). *Annales Geophysicae*, *5A*(6), 369–382.

Rosenfield, J. E., Newman, P. A., & Schoeberl, M. R. (1994). Computations of diabatic descent in the stratospheric polar vortex. *Journal of Geophysical Research*, *99*(D8), 16677–16689. https://doi.org/10.1029/94JD01156

Russell, J. M., III, Bailey, S. M., Gordley, L. L., Rusch, D. W., Horányi, M., Hervig, M. E., et al. (2009). The Aeronomy of Ice in the Mesosphere (AIM) mission: Overview and early science results. *Journal of Atmospheric and Solar-Terrestrial Physics*, *71*, 289–299. https://doi.org/10.1016/j.jastp.2008.08.011

Russell, J. M., III, Mlynczak, M. G., Gordley, L. L., Tansock, J., & Esplin, R. (1999). Overview of the SABER experiment and preliminary calibration results. *Proceedings of SPIE-The International Society for Optical Engineering*, *3756*, 277–288. https://doi.org/10.1117/12.366382

Ryan, N. J., Kinnison, D. E., Garcia, R. R., Hoffmann, C. G., Palm, M., Raffalski, U., & Notholt, J. (2018). Assessing the ability to derive rates of polar middle-atmospheric descent using trace gas measurements from remote sensors. *Atmospheric Chemistry and Physics*, *18*, 1457–1474. https://doi.org/10.5194/acp-18-1457-2018

Salmi, S.-M., Verronen, P. T., Thölix, L., Kyrölä, E., Backman, L., Karpechko, A. Y., & Seppälä, A. (2011). Mesosphere-to-stratosphere descent of odd nitrogen in February-March 2009 after sudden stratospheric warming. *Atmospheric Chemistry and Physics*, *11*, 4645–4655. https://doi.org/10.5194/acp-11-4645-2011

Sassi, F., Liu, H. L., & Emmert, J. T. (2016). Traveling planetary-scale waves in the lower thermosphere: Effects on neutral density and composition during solar minimum conditions. *Journal of Geophysical Research: Space Physics*, *121*, 1780–1801. https://doi.org/10.1002/2015JA022082

Sassi, F., Liu, H.-L., Ma, J., & Garcia, R. R. (2013). The lower thermosphere during the northern hemisphere winter of 2009: A modeling study using high-altitude data assimilation products in WACCM-X. *Journal of Geophysical Research - D: Atmospheres*, *118*, 8954–8968. https://doi.org/10.1002/jgrd.50632

Scherhag, R. (1952). Die explosionsartigen Stratosphärenerwärmungen des Spätwinters 1951/52. *Berichte des deutschen Wetterdienstes in der US-Zone*, *6*(38), 51–63.

Schneidereit, A., Peters, D. H. W., Grams, C. M., Quinting, J. F., Keller, J. H., Wolf, G., et al. (2017). Enhanced tropospheric wave forcing of two anticyclones in the prephase of the January 2009 major stratospheric sudden warming event. *Monthly Weather Review*, *145*(5), 1797–1815. https://doi.org/10.1175/MWR-D-16-0242.1

Schoeberl, M. R., Lait, L. R., Newman, P. A., & Rosenfield, J. E. (1992). The structure of the polar vortex. *Journal of Geophysical Research*, *97*, 7859–7882. https://doi.org/10.1029/91JD02168

Shadden, S. C., Lekien, F., & Marsden, J. E. (2005). Definition and properties of Lagrangian coherent structures from finite-time Lyapunov exponents in two-dimensional aperiodic flows. *Physica D: Nonlinear Phenomena*, *212*(3–4), 271–304. https://doi.org/10.1016/j.physd.2005.10.007

Sheese, P. E., Strong, K., Gattinger, R. L., Llewellyn, E. J., Urban, J., Boone, C. D., & Smith, A. K. (2013). Odin observations of Antarctic nighttime NO densities in the mesosphere-lower thermosphere and observations of a lower NO layer. *Journal of Geophysical Research - D: Atmospheres*, *118*, 7414–7425. https://doi.org/10.1002/jgrd.505610.1002/jgrd.50563

Sheese, P. E., Walker, K. A., Boone, C. D., McLinden, C. A., Bernath, P. F., Bourassa, A. E., et al. (2016). Validation of ACE-FTS version 3.5 NOy species profiles using correlative satellite measurements. *Atmospheric Measurement Techniques*, *9*, 5781–5810. https://doi.org/10.5194/amt-9-5781-2016

Shepherd, M. G., Cho, Y.-M., Shepherd, G. G., Ward, W., & Drummond, J. R. (2010). Mesospheric temperature and atomic oxygen response during the January 2009 major stratospheric warming. *Journal of Geophysical Research*, *115*, A07318. https://doi.org/10.1029/2009JA015172

Sinnhuber, M., Berger, U., Funke, B., Nieder, H., Reddmann, T., Stiller, G., et al. (2018). NOy production, ozone loss and changes in net radiative heating due to energetic particle precipitation in 2002-2010. *Atmospheric Chemistry and Physics*, *18*, 1115–1147. https://doi.org/10.5194/acp-18-1115-2018

Siskind, D. E., Bacmeister, J. T., Summers, M. E., & Russell, J. M., III (1997). Two-dimensional model calculations of nitric oxide transport in the middle atmosphere and comparison with Halogen Occultation Experiment data. *Journal of Geophysical Research*, *102*, 3527–3545. https://doi.org/10.1029/96JD02970

Siskind, D. E., Eckermann, S. D., McCormack, J. P., Coy, L., Hoppel, K. W., & Baker, N. L. (2010). Case studies of the mesospheric response to recent minor, major, and extended stratospheric warmings. *Journal of Geophysical Research*, *115*, D00N03. https://doi.org/10.1029/2010JD014114

Siskind, D. E., Harvey, V. L., Sassi, F., McCormack, J. P., Randall, C. E., Hervig, M. E., & Bailey, S. M. (2021). 2- and 3-dimensional structure of the descent of mesospheric trace constituents after the 2013 SSW elevated stratopause event. *Atmospheric Chemistry and Physics Discuss*. https://doi.org/10.5194/acp-2021-68,2021

Siskind, D. E., Nedoluha, G. E., Randall, C. E., Fromm, M., & Russell, J. M., III (2000). An assessment of southern hemisphere stratospheric NOx enhancements due to transport from the upper atmosphere. *Geophysical Research Letters*, *27*, 329–332. https://doi.org/10.1029/1999GL010940

Siskind, D. E., Sassi, F., Randall, C. E., Harvey, V. L., Hervig, M. E., & Bailey, S. M. (2015). Is a high-altitude meteorological analysis necessary to simulate thermosphere-stratosphere coupling? *Geophysical Research Letters*, *42*, 8225–8230. https://doi.org/10.1002/2015GL065838

Smith, A. K. (2012). Global dynamics of the MLT. *Surveys in Geophysics*, *33*, 1177–1230. https://doi.org/10.1007/s10712-012-9196-9

Smith, A. K., Garcia, R. R., Marsh, D. R., & Richter, J. H. (2011). WACCM simulations of the mean circulation and trace species transport in the winter mesosphere. *Journal of Geophysical Research*, *116*, D20115. https://doi.org/10.1029/2011JD016083

Smith, A. K., Marsh, D. R., Mlynczak, M. G., & Mast, J. C. (2010). Temporal variations of atomic oxygen in the upper mesosphere from SABER. *Journal of Geophysical Research*, *115*, D18309. https://doi.org/10.1029/2009JD013434

Smith, M. L., & McDonald, A. J. (2014). A quantitative measure of polar vortex strength using the function M. *Journal of Geophysical Research - D: Atmospheres*, *119*, 5966–5985. https://doi.org/10.1002/2013JD020572

10.1029/2020JD034523

Smith-Johnsen, C., Marsh, D. R., Orsolini, Y., Nesse Tyssøy, H., Hendrickx, K., Sandanger, M. I., et al. (2018). Nitric oxide response to the April 2010 electron precipitation event: Using WACCM and WACCM-D with and without medium-energy electrons. *Journal of Geophysical Research: Space Physics*, *123*, 5232–5245. https://doi.org/10.1029/2018JA025418

Straub, C., Tschanz, B., Hocke, K., Kämpfer, N., & Smith, A. K. (2012). Transport of mesospheric H_2O during and after the stratospheric sudden warming of January 2010: Observation and simulation. *Atmospheric Chemistry and Physics*, *12*, 5413–5427. https://doi.org/10.5194/acp-12-5413-2012

Wang, N., Datta-Barua, S., Chartier, A. T., Ramirez, U., & Mitchell, C. N. (2018). Horseshoes in the high-latitude ionosphere. *Journal of Geophysical Research: Space Physics*, *123*(7), 5831–5849. https://doi.org/10.1029/2017JA025077

Wang, N., Ramirez, U., Flores, F., & Datta-Barua, S. (2017). Lagrangian coherent structures in the thermosphere: Predictive transport barriers. *Geophysical Research Letters*, *44*, 4549–4557. https://doi.org/10.1002/2017GL072568

Winick, J. R., Wintersteiner, P. P., Picard, R. H., Esplin, D., Mlynczak, M. G., Russell, J. M., III, & Gordley, L. L. (2009). OH layer characteristics during unusual boreal winters of 2004 and 2006. *Journal of Geophysical Research*, *114*, A02303. https://doi.org/10.1029/2008JA013688

Yuan, T., Thurairajah, B., She, C.-Y., Chandran, A., Collins, R. L., & Krueger, D. A. (2012). Wind and temperature response of midlatitude mesopause region to the 2009 Sudden Stratospheric Warming. *Journal of Geophysical Research*, *117*, D09114. https://doi.org/10.1029/2011JD017142